2014

Optimization Of Wind Fence Enclosures For Infrasonic Wind Noise Reduction

Johnpaul Russell Abbott
University of Mississippi

OPTIMIZATION OF WIND FENCE ENCLOSURES FOR INFRASONIC WIND NOISE REDUCTION

A Dissertation
presented in partial fulfillment of requirements
for the degree of Doctor of Philosophy
in the Department of Physics and Astronomy
The University of Mississippi

by

JohnPaul Russell Abbott

May 2014

ABSTRACT

A large porous wind barrier enclosure has been built and tested to optimize wind noise reduction at infrasonic frequencies between 0.01-10 Hz in order to develop a technology that is simple, cost effective, and improves upon the limitations of pipe and porous hose arrays. The effects of varying the fence's porosity, modifying its top condition and bottom gap, doubling the height and diameter, and adding a secondary wind barrier were investigated. A simple mathematical model which estimates the wind noise measured at the center of the enclosure was derived based on the measured turbulence and velocity profiles measure outside the enclosure, inside the enclosure, and incident to its surface. The wind fence enclosure achieves wind noise reduction by minimizing the turbulence and velocity gradients at its center, and by decorrelating and area averaging the pressure fluctuations at its surface. The optimum wind fence has a surface porosity of 40-55%, a porous roof, no bottom gap, is very tall, wide, and is supplemented by a secondary wind barrier. The optimum wind fence can achieve a wind noise reduction of 20-27 dB over the 2-4 Hz frequency band, at least a 5 dB noise reduction for frequencies from 0.1 to 20 Hz, and a constant 4-6 dB of noise reduction for frequencies with turbulence wavelengths larger than the fence. At high wind speeds, 3-6 m/s, the optimized wind fence enclosure reduces wind noise sufficiently to detect microbaroms.

DEDICATION

This work is dedicated to my parents, Craig (the first Doctor Abbott) and Ellen, and the rest of my family, who have been a constant source of joy, encouragement, examples, and inspiration. Dad, Mom, Lovina, Tom, James, Jill, Erik, Elisabeth, Jacob, Mary, Wesley, McKay, and Jadiree.

ACKNOWLEDGEMENTS

I would like to thank my adviser, Dr. Raspet, for providing valuable suggestions, instruction, support, and focus for this research and dissertation. Further, for not giving up on me when it was probably most deserved. I would also like to thank Jeremy Webster for his help and instruction in programming, equipment, assembling the wind fences, and other problems and challenges. Special thanks to Chris Betts whose timely assistance in acquiring data and resetting the fences and equipment was invaluable. I would also like to thank my committee, Dr. Thomas Marshall, Dr. Joel Mobley, and Dr. James Chambers for their suggestions and insights to improving this dissertation. Special thanks to Justin Wagner, Jericho Cain, Jim O'Dell, Leanna O'Dell, Morgan Tholl, Elder Josh Clayson, Elder Kyle Cooper, Kenneth Scott, Blake Cantrel, Ryan Johnson, Greg Lyons, and the many others who have also helped in setting up the equipment, measurement preparation, advice, and other forms of timely support. Finally, thanks go to the Department of Physics and Astronomy and the National Center for Physical Acoustics for providing the materials, opportunities, and financial support to make this research possible.

This project was supported by both the United States Army Space and Missile Defense Command and the University of Mississippi Department of Physics and Astronomy. I am most grateful for their help.

TABLE OF CONTENTS

LIST OF TABLES

LIST OF FIGURES

CHAPTER I

INTRODUCTION

Infrasonic wind noise in an outdoor microphone is caused by non-acoustic pressure fluctuations generated by velocity fluctuations in a turbulent flow exerting a force on an object, such as the microphone or other turbulence structures in the flow. There are three types of these force interactions that generate pressure fluctuations in a turbulent flow. These interactions are called the turbulence-microphone interaction or the stagnation pressure, the turbulence-turbulence interaction, and the turbulence-shear interaction.

The first of these, stagnation pressure, is experienced by any bluff body in a fluid flow, [1-2] and is generated when the flow decelerates and becomes stationary or stagnant on the surface of the bluff body.[3] Stagnation pressure is the second term in Bernoulli's equation, $p + \frac{1}{2}\rho U^2 + \rho g h = C$, and is defined as $\frac{1}{2}\rho U^2$, where p is the pressure, ρ is the air density, U is the velocity of the air flow or wind velocity, g is the acceleration due to gravity, h is the height of the air column, and C is a constant. It can also be derived from the Poisson equation relating pressure fluctuations to a turbulent flow:

$$\nabla^2 p = -\rho \frac{\partial u_i}{\partial x_j} \frac{\partial u_j}{\partial x_i}, \quad i, j = 1, 2, \text{ and } 3, \tag{1}$$

where p is the pressure, ρ is the air density, u_i and u_j are the x, y, and z components of the fluctuating flow velocity, and $\frac{\partial}{\partial x_i}$, and $\frac{\partial}{\partial x_j}$ are the partial spatial derivatives of the flow in the x, y, and z directions; see Appendix A for the derivation. The interaction generates large pressure fluctuations when the turbulent flow is incident on the microphone. The measured pressure contribution from the stagnation pressure is the sum of the pressure fluctuations averaged over the surface area of the microphone. Of the three interactions, stagnation pressure is the strongest when the microphone is placed directly in the flow. However, stagnation pressure does not dominate if the microphone is encased in a windscreen since stagnation pressure is reduced due to the increased surface area. Noise due to stagnation pressure is also reduced by increasing the distance between the microphone and the turbulence interaction at the windscreen surface since the effect of the generated surface pressures decays with distance from the source as 1/r.

The second interaction, turbulence-turbulence, is the non-linear contribution of the pressure fluctuations in a turbulent flow. It is intrinsic to the turbulent flow, and will always occur with or without a bluff body placed in the flow. It is the second term in the Poisson equation relating pressure fluctuations to the turbulent flow,

$$\nabla^2 p = -\rho \frac{\partial^2}{\partial x_i \partial x_j}\left(u_i u_j - \overline{u_i u_j}\right), \quad i, j = 1, 2, \text{ and } 3, \tag{2}$$

where $\overline{u_i u_j}$ is the time average of fluctuating velocity, and p, ρ, u_i, u_j, $\frac{\partial}{\partial x_i}$, and $\frac{\partial}{\partial x_j}$ were defined previously; see Appendix B for the derivation. Pressure fluctuations are generated by turbules colliding and interacting with other turbules in the flow. Even though these pressure fluctuations are not generated by the flow's direct interaction with the microphone, they still act as a noise

source causing non-acoustic changes in the pressure field. Where the noise contribution due to stagnation pressure is the strongest if the microphone is unscreened, the noise contribution from the turbulence-turbulence interaction dominates when the microphone is screened and mounted above the ground surface. This contribution becomes dominant as the size of the windscreen increases and as the microphone's distance from the ground increases.

The third interaction is the turbulence-shear interaction. Pressure fluctuations for this interaction are intrinsic to the flow, and like the stagnation pressure, they may also arise by the direct interaction with a bluff body in the flow. The turbulence-shear interaction is the linear term in the Poisson equation relating pressure fluctuations to the velocity fluctuations in a turbulent flow:

$$\nabla^2 p = -2\rho \frac{\partial \overline{U}_j}{\partial x_i} \frac{\partial u_i}{\partial x_j}, \; i, j = 1, 2, \text{ and } 3, \tag{3}$$

where $\bar{U}_j$ and u_i are the x, y, and z components of the mean and fluctuating flow velocities, and p, ρ, $\frac{\partial}{\partial x_i}$, and $\frac{\partial}{\partial x_j}$ were defined previously; see Appendix B for the derivation. Fluid flow can be divided up into parallel layers of differing flow speeds. At the boundary between these layers there is a deceleration and change in the flow speed, called the flow velocity gradient. A fluid, such as air, is resistant to this change, which causes flow separation and shearing to occur, generating pressure fluctuations, vortices, and eddies. The shearing effect is not limited to boundaries between fluid flows, but also occurs at the surface of a stationary object set in a flow, such as a microphone, a windscreen, or at a stationary solid boundary, such as the ground. The strength of the shearing effect is dependent on the flow velocity gradient, where larger differences in flow speed will result in more shearing. Wind noise due to the turbulence-shear

interaction is the most dominant at low frequencies and for screened microphones placed near or at the ground. Further, for larger windscreens placed in the flow, the stagnation pressure at its surface alone does not account for all the wind noise. For these situations one must also consider the wind shears and flow deceleration within the vicinity of the windscreen.

Pressure fluctuations due to the turbulent flow—wind noise—are physically different from acoustic waves but their effect on a microphone is the same as an acoustic wave.[4] Microphones function by measuring a change in fluid pressure. As seen in the linear acoustic equations and wave equation, Eqs. (4-7),

$$\frac{\partial p}{\partial t} + \rho \nabla \cdot \vec{u} = 0\,, \tag{4}$$

$$\rho \frac{\partial \vec{u}}{\partial t} + \nabla p = 0\,, \tag{5}$$

$$p - c^2 \rho = 0, \quad c^2 - \left(\frac{\partial p}{\partial \rho} \right)_0 = 0\,, \tag{6}$$

$$\nabla^2 p - \frac{1}{c^2} \frac{\partial^2 p}{\partial t^2} = 0\,, \tag{7}$$

an acoustic signal is the change in pressure that is caused by the adiabatic compression and expansion of air. This pressure change travels as a wave through the air at a speed that is dependent on the air's density and ease of compression—the speed of sound. As seen by Poisson's equation, Eq. (1), a change in pressure can also be caused by the flowing motion of air, commonly experienced as wind, especially if the flow is turbulent. Unlike acoustic pressure fluctuations, pressure fluctuations from wind flow propagate at the same rate as the wind's flow speed, not the speed of sound, and do not depend on the fluid's compressibility. Despite these

differences, a microphone will react in the same way to changes in the pressure whether the changes are due to acoustic sources or wind flow. Since noise due to wind flow is indistinguishable from noise due to acoustic waves, wind noise is considered a type of "pseudo-noise".[5-6]

Noise levels due to turbulent wind flow are extremely high in the infrasonic frequency range, and effectively mask out the detection of acoustic infrasonic signals that are caused by seismic events, volcanic eruptions, explosions, and other infrasonic sources. This is problematic for organizations and systems that monitor such events; i.e. the International Monitoring System (IMS) network which monitors nuclear explosions and testing. The most effective way to reduce wind noise is to separate the microphone from the turbulent flow, which either reduces or eliminates the noise contributions due to the microphone's direct interaction with the flow—the stagnation pressure and turbulence-shear interaction. Separation can be achieved by mounting the microphone under a porous surface, which is flush to the ground, or encasing the microphone in a windscreen. Flush mounting the microphone is highly effective at removing the stagnation pressure, but does not entirely eliminate wind noise since the turbulence-shear interaction is very high at the ground and the turbulence-turbulence interaction is not affected.

An alternative method is to house or combine the microphone with a rosette spatial filter or similar type device that reduces wind noise by spatially averaging out the incoherent wind noise and coherently adding the large scale infrasound signals. Physically, rosette spatial filters consist of a series of long hoses or pipes with distributed inlet ports. The pipes are arranged as a radial array with one end of each pipe connected to a "secondary" summing manifold at a single nexus point, while the other end extends out from the manifold, forming a cluster or rosette. Several rosettes are then combined by using a solid pipe to connect the secondary summing

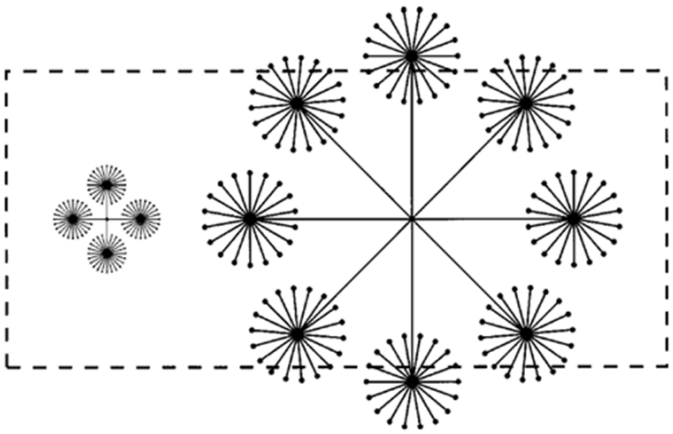

FIG. 1. Scaled sketch of an 18 m and a 70 m diameter rosette spatial filter, relative to a football field. (Sketch taken from Hedlin, Alcoverro, and D'Spain[9])

manifold directly to the microphone, or to a primary summing manifold encasing the microphone; see Fig. 1.[7-9] The microphone measures the sum of the pressure fluctuations sampled at each of these inlets. The spatial averaging occurs by exploiting the different correlation lengths and propagation speeds for acoustic signals and wind noise. At infrasonic frequencies the acoustic correlation length is larger than the correlation length for wind noise. If the inlet ports are spaced at lengths greater than the wind noise correlation length and less than the acoustic correlation length then the sampled wind noise becomes incoherent, while the acoustic signal remains coherent.[7-11] Therefore, when the sampled pressure fluctuations are summed together, the sum of the incoherent and out of phase wind noise will be lower than the coherent and in-phase acoustic signals. Noise reduction becomes more effective with an increased number of ports, N, and pipe length since the energy sum of the coherent signals grows as N^2 while the energy sum for the incoherent wind noise signals increases by N.[7-11]

Rosette spatial filters are effective at reducing wind noise but they also have significant limitations. First, since the noise reduction mechanism is highly dependent on the incoherence of wind noise and the coherence of the acoustic signal across the inlet ports, the frequency

bandwidth for efficient noise reductions is limited.[7-9] The bandwidth's upper limit is determined by the separation distance between the inlet ports relative to the acoustic wave length, while the lower limit is determined by the scale size of the turbulence relative to the size of the spatial filter. The acoustic waveform will be degraded at frequencies which correspond to acoustic wavelengths smaller than the spacing between the inlet ports. Second, to effectively reduce infrasonic wind noise the filter's spatial footprint needs to be very large—on the order of a hundred meters in diameter—which limits the types and sizes of areas where the filters can be deployed; see Appendix C. Third, spatial filters are directionally limited since they are highly dependent on proper phasing.[7-9] Fourth, spatial filters become ineffective at high wind speeds.[7-9] Fifth, pipe arrays are subject to the generation of self-noise and resonance noise that can occur in narrow pipes.[7-9]

Another approach for reducing wind noise is to place a microphone at the center of a large porous windscreen enclosure. A windscreen is a structure of any geometry that blocks or reduces the amount of wind flow near the microphone. A porous windscreen reduces wind noise by forcing the local pressure fluctuations due to the stagnation pressure and turbulence-shear interaction away from the microphone and out to the surface of the screen. Since there is little flow inside of a porous windscreen, the noise sensed by a microphone at the center of a windscreen is equal to the sum of the pressure fluctuations averaged over the entire surface area of the windscreen.[1-2, 7, and 12-14] Wind noise correlation lengths are short and decrease at the surface of a porous boundary. Therefore, as a windscreen increases in size, the size of the averaging area, the incoherence between surface pressure fluctuations, and the distance between the microphone and the surface pressure fluctuations all increase, reducing the wind noise sensed by the microphone.[13-15] Wind noise is also decreased since windscreens reduce the size of the

turbulence as the wind passes through the windscreen's surface. Since frequency is proportional to the size of the turbulence, the smaller turbulence will result in less wind noise at low frequencies.[7]

A windscreen does not entirely eliminate wind noise; in order for it to be most effective a windscreen must remain porous. A microphone encased in a windscreen is either partially or completely unaffected by noise contributions from the stagnation pressure and the shearing interactions that occur local to the microphone, depending on the frequency, and on the windscreen's porosity and size. A non-porous windscreen completely shields the microphone from the turbulent flow, isolating it from the wind noise by concentrating all the pressure fluctuations at the screen's surface. This eliminates the stagnation pressure due to the direct interactions of the turbulence with the microphone. Intuitively this seems to be the ideal design since the stagnation pressure is the dominant source of wind noise, and the increased area averaging at the screen's surface significantly reduces this interaction. However, this design is ineffective, since the velocity gradients and turbulence-shear interaction are higher on the surface of a non-porous barrier, which generates larger pressure fluctuations at the surface. These pressure fluctuations are then propagated to the microphone through the windscreen's surface.

In contrast, a porous windscreen reduces the shearing and stagnation effects by modifying the average velocity gradient at the screen's surface and at the microphone. A porous surface results in a more gradual deceleration and change in the incident and adjacent flow velocity, thus reducing the velocity gradient and shearing effects. Therefore, a porous wind barrier reduces the turbulence-shear interaction at its surface. However, there is additional wind noise at the microphone since the increased porosity allows for stagnation pressure and shearing at the microphone. Ideally, a windscreen produces the most wind noise reduction for porosities

that minimize the sum of the wind noise due to the direct interaction at the microphone and the turbulence-shear interaction at the windscreen's surface.

Windscreen enclosures have many of the same advantages as rosette spatial filters, such as effective infrasonic wind noise reduction; but are less affected by their limitations. First, they are more cost effective. Second, windscreens enclosures do not degrade or modify the acoustic waveform for higher frequencies since there is no upper limit for the filtering bandwidth. Third, they are more compact and can be deployed in spatially constricted areas. Fourth, a porous windscreen can still reduce wind noise for frequencies which correspond to turbulent wavelengths that are larger than the windscreen.[7] Fourth, since the acoustic signals and wind noise do not arrive at the microphone via narrow pipes but rather through the open air, porous windscreens are free from resonance noise that occur in narrow pipes.[7] Fifth, enclosures offer better security and protection from the weather and from potential damage to pipes and microphones from livestock. Sixth, depending on their design, windscreen enclosures can be rapidly deployed. Seventh, windscreen noise reduction does not rely on proper phasing between acoustic signals and wind noise sampled at multiple inlet ports, since both acoustic signals and wind noise are sampled by the microphone at a single point.[7] Finally—as more of a benefit than an advantage since this is also true for all symmetric spatial filters— if the distance between the microphone and the windscreen's surface is uniform in all directions, the noise reductions are independent of the wind's direction since a windscreen does not rely on proper phasing.

The main goal of this research is to build a large windscreen from commercially available materials and determine the characteristics that will optimize the noise reduction in the infrasonic frequency band. We also seek to understand the physical mechanisms for wind noise reduction

and to develop a simple calculation to estimate the wind noise reduction of a wind barrier, to be used for future designs and noise reduction applications.

As a point of clarification, a "wind barrier" or "wind fence" or "wind fence enclosure" will refer to a large enclosure that functions as a windscreen, with dimensions that are several meters in size and is made of fencing type materials. The terms "wind barrier", "wind fence", "wind fence enclosure" and related variations of these terms will be used interchangeably throughout this dissertation. The term "windscreen" will generally refer to a compact spherical turbulence reducing device, such as a porous foam ball or the devices described by Morgan,[1] Bleazy,[19] and others.[13, 20-27]

The remaining chapters will discuss past research on this subject and how the research for this dissertation was conducted. Chapter II will first present a review of the research and development of theories regarding the mechanisms for wind noise reduction in windscreens and wind noise generation. Second, it will present the research about the physical and theoretical design of windscreens and wind barriers, including their aerodynamics, geometries, recent and current wind barrier designs, and their respective effects on the surrounding turbulent field. Chapter III discusses the conceptual theory for designing and optimizing a wind barrier based on the theories and designs presented in Chapter II. Further, it discusses the criteria for designing an experimental wind barrier based on the conceptual theory. Chapter III also gives a description of the initial wind barrier chosen for this research. Chapter IV presents the six measurement series that investigated different methods and the physical characteristics of the wind fence that optimize noise reduction. This chapter also presents the results of an investigation to verify the source of an observed narrow frequency band enhancement in the wind noise spectra measured inside the wind fence. Chapter V presents the derivation of the empirical model which can be

used to provide an estimate of a wind fence enclosure's noise reduction capability. Chapter V also presents a comparison of the predicted and measured wind noise spectra in order to validate the empirical model. Finally, Chapter VI will present the summary and conclusions of this dissertation.

CHAPTER II

LITERATURE SURVEY

1. Theoretical Background

To properly model, design, and optimize a barrier's noise reduction capability it is necessary to first understand the sources of infrasonic wind noise in microphones and the physical mechanisms of how wind barriers and windscreens produce wind noise reductions. Section 1 of the literature review describes previous research on these topics.

A. Theory of wind noise reduction for a windscreen

Poisson's equation for incompressible flow implies that the pressure fluctuations at the center of a compact spherical windscreen are the sum of the pressure fluctuations area averaged over the surface of the windscreen. The distribution of the pressure fluctuations at low frequencies from the front to the back of the windscreen is partially uncorrelated. Therefore the principle mechanism for wind noise reduction by a windscreen is the combination of the reduced pressure fluctuations in the lee portion of the windscreen with the rapid decorrelation of the incident turbulence over the surface of the windscreen—leading to efficient area averaging. There is also some reduction due to the porous surface, since a porous surface leads to smaller

normal and transverse gradients of the steady flow. The reduced pressure fluctuations can be calculated by taking the correlation of the pressure fluctuation distribution over the surface of the windscreen, $\Re(pp^*)$, and then integrating it over the surface area.[15]

Another useful concept is scaling laws for wind noise reduction by a windscreen. Scaling laws state that windscreens of similar shape but differing size will have nearly identical noise reductions when the spectra of the reductions are plotted versus the reduced wavenumber, kD, where D is a characteristic dimension of the windscreen. Therefore the wavenumbers or frequencies at which noise reduction occurs for a windscreen is dependent on its size and by increasing either the windscreen's height or diameter, or both, reductions should shift to a lower wavenumber—improving the reductions at low frequencies.

This first section of the literature review will examine the history, application, and evolution of the theory for wind noise reductions in a compact windscreen to its current form and how scaling laws apply to the noise reduction of a windscreen. The review will start with Phelps' derivation of the pressure fluctuation distribution over a sphere[28] in a perfect non-turbulent steady fluid flow and end with Webster, Raspet, and Yu's discovery of the rapid decorrelation between the pressure fluctuations at the surface of the windscreen.[15] While some of the theories that will be presented are now considered incorrect, they do serve as steps in developing the theory and are worth considering.

Phelps[28] was the first to propose the hypothesis that wind noise at the center of a spherical windscreen was due to the difference in the magnitude and phase of pressure fluctuations between points on the surface of a windscreen, instead of due to flow inside the windscreen. He proposed that if the magnitude and phase of the wind pressure fluctuations were

known over the entire surface of the microphone then a windscreen could be designed to take advantage of the differences between these points and minimize noise at the microphone's surface. Phelps then derived an equation describing the distribution of pressure fluctuations over a body in an airflow. Assuming a perfect, incompressible fluid in a steady irrotational or non-turbulent flow, and Laplacian boundary conditions for a sphere (zero velocity inside the sphere), Phelps determined the following equation:

$$p(\theta,t) = \rho\frac{V^2}{8}\left[9\cos^2\theta - 5\right] + \frac{1}{2}\rho a\cos\theta\frac{\partial V}{\partial t} + P, \qquad (8)$$

where ρ is the density of air, V is the velocity, a is the radius of the sphere, and θ is the angle between the point of observation and the line passing through the center of the sphere parallel to the mean velocity. The value P is the pressure at $\theta = \pi/2$ and at a radial distance significantly greater than the radius of the sphere, or $r >> a$. The equation predicts a difference in magnitude and phase for pressure across the surface of the sphere—positive at the front and negative at the back. To prove his hypothesis, Phelps measured the response for a microphone covered with an ellipsoidal shaped windscreen and a beveled-disk shaped windscreen called a Bernoulli windscreen, for various flow speeds in a mechanically generated flow. Variations in phase and magnitude over the surface were observed for both windscreens. The pressure at the front of both the windscreens was the same, but the magnitude of the pressure behind the Bernoulli windscreen was larger than the ellipsoidal windscreen, suggesting a low pressure region behind the ellipsoidal windscreen due to flow separation.

Strasberg[29] contributed to the theory of wind noise reduction caused by a windscreen while examining potential non-acoustic noise sources for hydrophones. Strasberg considered the shielding provided by a windscreen for a microphone to be similar to the shielding provided by

the compliant casing around a hydrophone's sensitive element. The treatment and examination of non-acoustic noise sources due to turbulent water flow around a hydrophone is therefore the same as the treatment for turbulent airflow around a windscreen-encased microphone. Strasberg states that the majority of the noise in the sensitive element is due to pressure fluctuations detected at the surface of the hydrophone's casing. The magnitude of the response due to these pressure fluctuations is dependent on the average of the surface pressure. If the phase of the pressure fluctuations varies across the hydrophone's surface then the pressures at different locations on the surface will partially cancel out and reduce the response of the hydrophone's sensitive element. Strasberg also proposed that if the scale size or wavelength of the spatial variations for a turbulent flow is much larger than the largest dimension of the hydrophone's sensitive region (the compliant casing), then the turbulent flow can be assumed to act the same as a spatially uniform steady flow. Thus a turbulent flow in the low frequency can be treated as a steady flow for a compact hydrophone or windscreen. Finally, Strasberg observed that the response of a hydrophone's sensitive element due to turbulence induced surface pressure fluctuations will be lowered as the size of the hydrophone's compliant casing increases. He states that this is due to 1) a larger averaging area, 2) an increased cancellation in pressures due to larger phase variations, and 3) that the magnitude and effect of the pressure fluctuations at a sensing element will decrease as the distance to the surface of the casing increases.[24, 30]

Later, Strasberg[30] showed that measurements of pressure fluctuations in a non-turbulent flow followed scaling laws by applying dimensional analysis to previously published data.[20-23] He derived a universal empirical formula with this method which relates the sound pressure level in one-third octave bands to a dimensionless frequency given by fD/V, where f is the frequency, D is the windscreen diameter, and V is the average wind speed;

$$20\log\left(\tilde{p}_{1/3}/\rho V^2\right) = -81 - 23\log\left(fD/V\right). \quad (9)$$

Strasberg noted some limitations to the formula. Since the formula was derived only from non-turbulent data measured in a laboratory setting, data from outdoor turbulent measurements cannot fit Eq. (9). Strasberg also suggested that factors such as porosity, windscreen size or the distance from the microphone to the surface of the windscreen, and other details of construction that he assumed to be negligible may also affect wind noise reduction.

Morgan[1] investigated the physical mechanisms that cause low-frequency wind noise in outdoor microphones, and studied the effectiveness of different types of compact windscreens to help reduce this noise. He compared the measured pressure fluctuations of an unscreened microphone set both perpendicular and parallel to the direction of the flow to a screened microphone. The screened microphone was encased in three types of polyurethane foam windscreens of comparable cross-sectional area and porosity: a spherical screen with uniform porosity, a layered spherical screen with the same size and porosity as the first but with an added inner sphere of denser foam, and a flat disk shaped windscreen. He also investigated the effect of a windscreen's size and porosity by comparing the measured pressure at both the center and surface of windscreens with similar shape and construction but having different porosities and sizes. The measurements showed that changing porosity has little to no effect on noise reduction for small compact windscreens, within a limited range of foam porosities.

Morgan further developed the theory that wind noise at the center of a windscreen is due to the distribution of the pressure fluctuations at its surface by using Phelps' surface pressure distribution equation, Eq. (8), to predict the pressure at the center of a spherical windscreen in a turbulent flow. Like Strasberg, Morgan argued that Phelps' equation can be applied to a

turbulent flow for low frequencies since the vorticity for large eddies is very small. The pressure fluctuations at the center of a windscreen was determined by assuming that the second term in Eq. (8), $\frac{1}{2} pa \cos\theta \frac{\partial V}{\partial t}$, is negligible at low frequencies[19] and then rewriting the remaining parts of the equation in terms of first and second order Legendre polynomials. Solving for the pressure gave a predicted value of about one-half the stagnation pressure, which is about 6 dB of reduction. Morgan noted that this prediction was about 9 dB lower than the actual measured values.

Morgan also showed that the pressure at the center of a windscreen is due to the average pressure fluctuations at its surface, as suggested by Strasberg. He measured and plotted the surface pressure distribution with respect to the azimuth angle, θ, for both the 9 cm and 18 cm diameter windscreens and then numerically integrated these measurements with respect to the surface area. Morgan compared the value of the numerically integrated measured distribution curves to the pressure measured by both the unscreened microphones and the microphones encased in 9 cm and 18 cm diameter windscreens. He found that not only did the numerical integration show about 15 dB of reduction; the reductions also matched the pressure measured by the screened microphones. Further, he showed that the pressure distribution curves for the two windscreens had the same magnitude and shape. This suggested that the surface pressure distribution with respect to the angle θ is independent of windscreen size, for small windscreens with limited range of porosities. Both of these measured distribution curves matched Phelps' distribution curve, therefore area averaging Phelps' equation, Eq. (8), should yield similar noise reduction results.

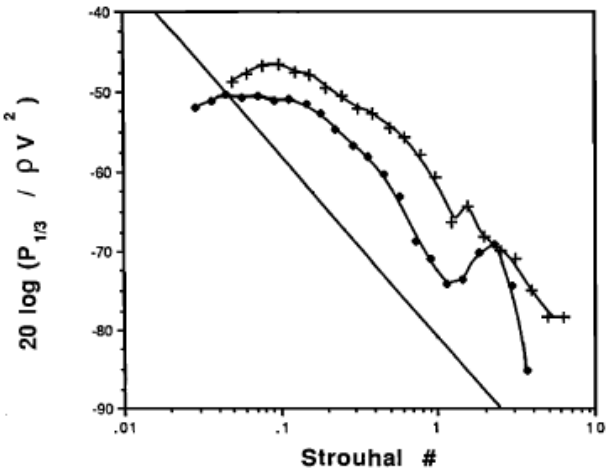

FIG. 2. Comparison between the Strasberg universal scaling law, Eq. (9), and two 5 min outdoor data averages as measured by Morgan[1-2] for dimensionless sound pressure in decibels, $20\log P_{1/3}/\rho V^2$, versus Strouhal number, fD/V. The Strasberg equation is the solid line, $+V$ = 5.8 m/s, and $\blacklozenge V$ = 9.9 m/s. (Plot taken from Morgan[2])

Finally, Morgan[2] showed that Strasberg's universal scaling law, Eq. (9), poorly predicts the wind noise for measurements of high-turbulence flows, typical in outdoor settings; see Fig. 2. He concluded that scaling laws relating to wind screen diameter are different for outdoor turbulence than for low-turbulence flows, and that further study is necessary. However, as part of his dissertation, Morgan[1] examined how the scale size of the windscreen relative to the turbulence affects noise reduction by plotting the measured noise reductions with respect to the ratio of the size of the windscreen to the size of the turbulent eddy, D/λ. The plot shows that attenuation at the center of the windscreen increases with frequency and is directly proportional to the diameter of the screen. Therefore, wind noise reductions at low frequencies will increase as the diameter of the windscreen is increased.

Zheng and Tan[12] conducted a theoretical experiment to investigate how different types of uniform flows with low-frequency turbulence affect the pressure distribution on the surface and at the center of a rigid impermeable spherically shaped windscreen. They proposed that the

surface pressure distribution and the pressure at the center of a windscreen are determined by the type of flow impinging on the windscreen. Zheng and Tan followed the theories proposed by Phelps, Strasberg, and Morgan, and assumed that at low-frequencies a turbulent flow behaves the same as a steady-state flow. They also defined a low-frequency flow to be any flow with turbulence wavelengths larger than the windscreen. Following these assumptions, Zheng and Tan developed a theoretical distribution function, $p(a,\theta)$, for three types of flow: an unsteady inviscid flow, a low-Reynolds-number Stokes flow, and an intermediate and high-Reynolds-number flow, and then integrated this distribution function over the surface area of the windscreen to determine the pressure at its center. The wind noise reduction was determined by dividing the computed center pressure by the stagnation pressure in a uniform flow. The authors concluded that wind noise reduction for a windscreen is correlated with the Reynolds-number; the wind noise reduction increases as the Reynolds-number decreases, and that the Reynolds-number is determined by the average wind speed and windscreen radius.

Hedlin and Raspet,[7] who will be discussed again in greater detail later (see page 33), as part of an investigation to compare the noise reduction of a wind fence to two rosette spatial filters, applied scaling laws to the results of a wind fence with moderate success. They also applied the theory that wind noise at the center of a windscreen is the area average of the pressure fluctuations at its surface to the results. Hedlin and Raspet used these laws and the theory to help explain why the wind fence had achieved moderate noise reduction for turbulence scales larger than its size while the rosette spatial filters had not achieved any noise reduction. Their investigation and success is mentioned here, not because it helped to modify or advance the noise reduction theory, but because it suggests that both scaling laws and the noise reduction theory can also be applied to wind barriers and wind fences of different shapes and size.

Raspet, Webster, and Dillion[27] investigated wind noise reduction for spherical windscreens in turbulent flows above the ground, at frequencies within the inertial subrange. The inertial subrange is a portion of the spectrum where wavelengths are less than the source's height above the ground, but larger than the Kolmogorov microscale. The turbulence in this region is isotropic and energy neither enters the system nor is dissipated. The spectrum is divided into two other portions: the source region or energy-containing subrange, and the dissipation subrange. The source region is for wavelengths which are a significant fraction of the inversion height, while the dissipation region are for wavelengths smaller than the Kolmogorov microscale.[31] Their investigation provided theoretical predictions giving upper and lower bounds to wind noise measurements and reductions. Raspet et al. applied the earlier windscreen reduction theories to argue that a large windscreen will reduce the stagnation pressure contribution to a low enough level that the turbulence-turbulence contribution dominates. They determined that the upper limit for wind noise measurements is the stagnation pressure as measured by an unscreened microphone and the lower limit is the turbulence-turbulence interaction as measured by a compact windscreen. The authors found that the limit set by the turbulence-turbulence interaction is the maximum amount of noise reduction that can be achieved by a compact windscreen. As a windscreen increases in size, the surface generated pressure fluctuations are reduced until only the intrinsic pressure fluctuations can be measured. These calculations were later extended into the source region by Raspet, Yu, and Webster, who also determined a calculation for the turbulence-mean shear interaction.[13] Raspet, Yu, and Webster further showed that the lower limit for wind noise measurements is not only set by the turbulence-turbulence interaction, but by the sum of the turbulence-turbulence and turbulence-shear interactions.

Raspet, Webster, and Yu[15] investigated low frequency wind noise reduction for a compact spherical windscreen. They determined that the assumption for turbulent flow at low frequencies was incorrect. The assumption states that for low frequencies, or frequencies where the size of the turbulence is larger than the diameter of the windscreen, a turbulent flow will behave the same as a uniform steady flow. Therefore positive pressure fluctuations are distributed at the front of the windscreen and negative pressure fluctuations are distributed at the back. Noise reductions are therefore caused when the opposite phased pressure fluctuations are canceled out from the area averaging of the surface pressures. Raspet et al.[15] pointed out that if this low frequency assumption was true, then the correlations between the incident pressure fluctuations at the front of the windscreen and the pressure fluctuations measured at different angles along the surface should be approximately +1 for angles at the front of the windscreen and -1 for angles at the back of the windscreen. To test the hypothesis Raspet et al. measured and correlated the pressure distribution around a spherical windscreen. Instead of varying between +1 and -1, as expected, they found the correlations decayed very rapidly with respect to the azimuthal angle—suggesting that something other than the cancelation of the steady state pressure distribution causes noise reductions.

To verify their findings, Raspet et al.[15] measured the velocity correlations around the spherical windscreen and in open air. They found that the velocity correlations had the same correlation length as the correlations for the pressure fluctuations. They also showed that the correlation length in open air between upwind and downwind sensors was comparable to one over the wavenumber, 1/k, while the correlation length for flow in the vicinity of the windscreen was much smaller. Their findings suggest that the presence of the spherical windscreen significantly reduces the correlation length of the turbulence in the vicinity of the windscreen at a

given frequency. Also, to verify that a porous surface induces decorrelation of pressure and velocity fluctuations Raspet et al.[15] examined the measurements performed by Dillion[25] for a flush mounted microphone under a thin sheet of foam and the spherical windscreen measurements made by Webster, Raspet, and Yu.[26] Their investigation showed that the presence of a porous surface causes rapid decorrelations in both the pressure and velocity fluctuations, independent of the windscreen's shape. Based on all these findings, Raspet et al.[15] state that the primary mechanism for noise reduction in spherical windscreens is not the cancellation between pressure fluctuations in the front of the screen and the opposite phase fluctuations on the leeward side of the screen, but rather the combination of reduced pressure fluctuations in the lee portion of the sphere with the decorrelation of the incident turbulence over the surface of the windscreen.

B. Sources of infrasonic wind noise generation in microphones

This section will consider wind noise generation and the models that have been developed to describe it. Morgan[1] and Morgan and Raspet[2] state and show that the principle source of wind noise in unscreened microphones is the stagnation pressure—the interaction of the incident turbulent flow with a microphone or other bluff body placed in the turbulent flow. Raspet, Webster, and Dillion[27] and then Raspet, Yu, and Webster[13] showed, however, that noise is generated not only by the interaction between the turbulence and microphone, but is the sum of several turbulent interactions. The other contributions to the wind noise are the turbulence-turbulence interaction and the turbulence-shear interaction.

Dillion[25] tested a hypothesis posed by Elliot[32-33] and Fuchs[34] that noise due to the stagnation pressure would be eliminated by flush mounting a microphone to the ground, leaving only the intrinsic pressure fluctuation—reducing the overall wind noise level. Dillion compared a microphone flush mounted onto a flat plate sitting on the ground with a microphone encased in a small, 9.0 cm diameter wind screen, set 1.0 meter in the air. Dillion postulated that if Elliot and Fuchs' hypothesis was correct then the magnitude of the wind noise spectra measured by the flush mounted microphone should be much smaller that the wind noise spectra measured in the screened microphone. However, the data showed that the magnitude of the wind noise level for the flush-mounted microphone was higher than the screened microphone contrary to the theory posed by Elliot and Fuchs. Although Dillion speculated that the increased noise at the boundary was due to the turbulence-mean shear interaction, he could not confirm this idea since a theoretical prediction for the turbulence-mean shear interaction in a bounded flow had not been developed. He concluded that even though the stagnation pressure was eliminated by flush mounting the microphone, the turbulence-shear interaction is a significant source of wind noise for flush mounted microphones.

Yu,[14] as part of her master's thesis, and Raspet, Yu, and Webster[13] improved the mathematical expressions derived by Raspet, Dillion, and Webster[15] for calculating the stagnation pressure and the turbulence-turbulence interaction for a microphone located above the ground in a turbulent flow. This model extended these calculations to include the estimates of the pressure fluctuations in the source region as well as the inertial region. Yu also derived an expression for the turbulence-shear interaction for a microphone located above the ground in a turbulent flow for the entire spectral range. The model was derived by first assuming that turbulence is both isotropic and homogeneous and then fitting the measured turbulence spectra to

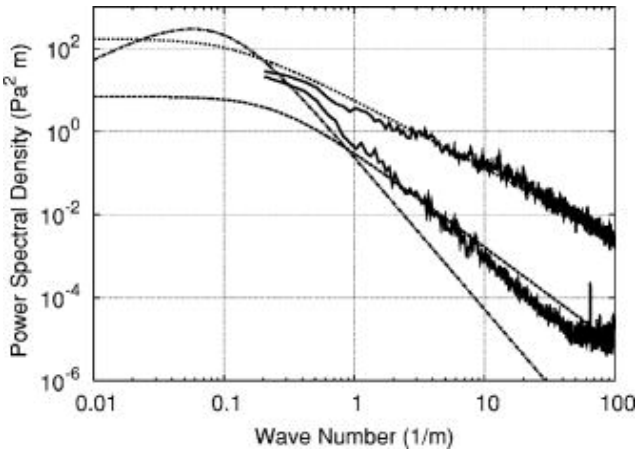

FIG. 3. Predicted wind noise spectra for the stagnation pressure (dotted line), the turbulence-turbulence interaction (dash-dotted line), and the turbulence-shear interaction (dashed line) with respect to the wavenumber, $k = 2\pi f/U$. The plot also shows the measured wind noise spectra for an unscreened microphone and a microphone encased in a 1.0 m diameter fiberglass windscreen. (Plot taken from Yu, Raspet, and Webster[13])

a form similar to the von Karman spectrum of a free jet, as suggested by George, Beuther, and Arndt.[35] These mathematical models show that in the inertial range the turbulence-shear, turbulence-turbulence, and stagnation pressure interactions decay with respect to wavenumber as powers of -11/3, -7/3, and -5/3, respectively. In the source region the turbulence-shear interaction increases with respect to wavenumber as a power of 5/3 while the turbulence-turbulence interaction and the stagnation pressure remain constant. The models also showed that at low wavenumbers the turbulence-shear interaction dominates; see Fig. 3. To validate the predictions, the authors compared the predicted and measured pressure fluctuations for a bare and screened microphone in a turbulent flow above the ground. The comparisons showed that the unscreened microphone agreed best with the predictions for the stagnation pressure, while fluctuations measured by microphones inside large spherical windscreens best matched the turbulence-turbulence interaction. The predictions for the turbulence-shear interaction did not consistently agree with the measured wind noise. The authors concluded that the principle

source of wind noise for an unscreened microphone is the stagnation pressure, that the turbulence-turbulence interaction is the dominant noise source for a large screened microphone set above the ground, and that the turbulence-shear interaction was not a principle noise source for a microphone set above the ground. However, later, as part of her dissertation work, Yu[36] showed strong agreement between the predictions for the turbulence-shear interaction and the wind noise measured by a screened microphone mounted flush to the ground, instead of above the ground.

Yu's dissertation[36] and the related paper by Yu, Raspet, Webster, and Abbott[37] derived the theory and mathematical prediction model that describes the turbulence-shear interaction for both unscreened and screened microphones mounted flush to the ground. The model is based on theories developed by Kraichnan[38-39] and George et al.[35] The predictions are derived from the wind velocity spectra and wind velocity profile measured near the ground, and show that for a microphone mounted flush to the ground in a turbulent flow, the turbulence-shear interaction decays with respect to wavenumber as a power of -5/3 in the inertial range instead of -11/3 for a microphone set above the ground in a turbulent flow. Based on Dillion's[25, 27] investigation, Yu

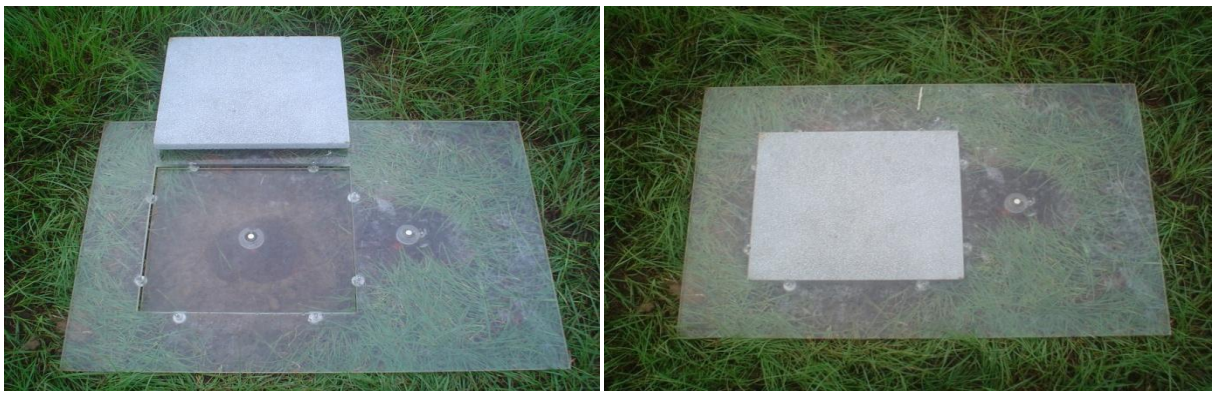

FIG. 4. Set up used by Yu[38] depicting the flush mounted microphones. The microphone on the right is left bare with its diaphragm flush with the plate. The microphone on the left covered by a sheet of foam, with the top of the foam set flush to the ground. (Images taken from Yu[36])

theorized that the turbulence-shear interaction is the dominant source of wind noise at or near the ground and not the turbulence-turbulence interaction. The theory was tested by comparing the predicted wind noise spectra to the wind noise spectra measured by a bare microphone mounted flush to the ground and a microphone covered by a sheet of foam, with the top of the foam set flush to the ground; see Fig. 4. Comparisons showed strong and consistent agreement between the predicted and measured wind noise for the screened microphone. However, the agreement between the predicted and measured wind noise for the bare flush mounted microphone was inconsistent, sometimes matching well and sometimes not at all. From these results Yu concluded that the turbulence-shear interaction is the dominant source of wind noise at the ground. Yu, Raspet, Webster, and Abbott[40] then improved the predictions for the turbulence-shear interaction for a microphone set above the ground, by including changes in the wind velocity gradient as a function of altitude.

Yu's dissertation[36] also demonstrated how different wind velocity profiles affect the generation of pressure fluctuations at a boundary. The magnitude of the pressure fluctuations and hence her predictions for the fluctuations are determined in part by the shear velocity gradient. The velocity gradient is defined as the derivative of the mean horizontal flow velocity profile with respect to the vertical spatial displacement, or $s(z) = \partial U/\partial z$. The profile is determined by different atmospheric and terrain conditions. She noted that the magnitude of the predicted wind noise level is typically higher for conditions where the gradient is larger, such as a neutral atmosphere versus a stable atmosphere. The profile's form was determined from published theories and measurements relating the different meteorological, atmospheric, and terrain conditions.[31, 41, 42] Yu used two laws to calculate the wind noise spectra based on the measured velocity profiles. The first was the logarithmic law, or $u(z) = a\ln(z/z_0)$, where a is

the logarithmic amplitude, z is the height above the ground, and z_0 is the aerodynamic roughness length. This is the velocity profile for a flat open terrain with either a neutral or an unstable atmosphere—typical of windy conditions on either a cloudy or sunny day. The second was a multi-exponential law, $u(z) = u\left(1 - \sum_{i=0}^{n-1} A_i e^{-\beta_i z} - \left(1 - \sum_{i=0}^{n-1} A_i\right) e^{-\beta_n z}\right)$. This law is a more general form and can be used to describe a wide variety of profiles and conditions. Yu showed that this law could match a logarithmic profile but that it could also be used when the wind profile was not logarithmic, which is typical of a stable atmosphere. All of her measurements were performed over flat open terrain on highly windy days; hence the majority of the measured profiles were logarithmic.

Yu's logarithmic model should accurately predict the pressure fluctuations for the velocity field upwind of the wind fence enclosure. However, since the model is limited to open terrain conditions, it will not accurately describe the pressure fluctuations as related to the velocity spectra and profile that occur inside the wind fence since the wind profile is disrupted and changed as it passes through the fence. It is therefore necessary to consider other models that can be used to evaluate the effects of the changed profile as it passes through an enclosed area.

Cionco[43] developed a mathematical model to describe airflow and its effects on the microclimate under trees and other vegetative canopies. He states that turbulence generation is affected by the velocity gradient, which is determined by the wind velocity profile. His model shows that while the wind velocity profile above a canopy follows the logarithmic law, below a canopy the velocity profile tends to behave more like an exponential law, $u(z) = u_h \exp[a(z/h - 1)]$, which can be modeled with Yu's multi-exponential model; where u_h is the velocity amplitude, *a*

is a constant, z is the height above the ground, and h is the canopy height. Other studies by Allen,[44] Amiro,[45-46] Raupach and Thom,[47] and Baldocchi and Meyers[48-49] on wind flow through forests and tree canopies give similar conclusions and models. Cionco and the other authors noted that the profile was strongly influenced by foliage density and overall porosity. They also concluded that the tree canopies act as the aerodynamic roughness length, which tends to raise the atmospheric boundary layer. Such behavior is commonly used to describe one of the turbulence reduction mechanisms for wind barrier enclosures.[50-53]

Finally, when considering sources of noise generation for a turbulent flow it is important to consider the effective size of the noise source region. As part of determining the correlation lengths of the pressure and velocity fluctuations, Abbott,[18] showed that the effect of the noise source region is spatially very large and non-local, especially at low frequencies. Raspet et al.[27] state that the size of the pressure region is approximately U/*f*, where U is the average wind speed and *f* is the frequency. The size of the pressure region will increase as the turbulent frequency decreases. Lauchle[16] also showed that the noise source region for plane boundaries is very large at low frequencies and is inversely proportional in size to the wavenumber, or k = $2\pi f$/U. Following the theory developed by Kraichnan,[37] Lauchle derived an equation [Eq. (10)] for the pressure spectra generated by turbulent flow over a flat plate as a function of source height, z; see Appendix D for the derivation.

$$P\left(\vec{k},\omega\right)=\frac{1}{\kappa}\int_{z>0}e^{-\kappa z}Q\left(z,\vec{\kappa},\omega\right)dz \tag{10}$$

$Q\left(z,\vec{\kappa},\omega\right)$ is the space and time Fourier transform of the Poisson equation and κ is the magnitude of the horizontal wavenumber, $\kappa=\left|\vec{\kappa}\right|=\sqrt{k_x^2+k_y^2}$. Equation (10) shows that the

pressure spectrum, $P(\vec{k},\omega)$, decreases exponentially with wavenumber; therefore the noise source region for large wavelengths—low wavenumbers and frequencies—is very large.

2. Design Criteria

A. Basic aerodynamics of wind barriers and their sheltering effects

Most of the early published research describing the aerodynamics of wind screening devices and their sheltering effects on the wind velocity flow field were limited to two-dimensional wind fences or shelter belts used for crop protection and other agricultural applications. Fortunately, the research provides a thorough picture of how the velocity profiles, turbulence, and turbulence power spectra on the lee side of the fences are affected by the shearing, total drag, distribution of the drag, boundary layer profiles of the approaching flow, shelter shape, height, porosity, thickness, location, fetch, roughness height, shear velocity, and the material—natural vegetation versus man-made fence—used to make the fences.

Plate[54] created a basic and simplified model describing the aerodynamics of a shelter belt, and the different flow regions surrounding the shelter belt which are characterized by changes to the turbulent flow, velocity profile, and velocity gradient. The model also describes how the aerodynamics affects these flow regions. Plate describes the model as "…physically unrealistic and somewhat oversimplified, yet it does point to the decisive role which the drag plays in the shelter problem, and it also leads to a prediction of velocity profiles…" He also provides a schematic (Fig. 5) which shows a boundary layer flow around a solid wedge-shaped object on a flat plate; and states that the regions directly in front of and behind the object (Region 2 and 6 in

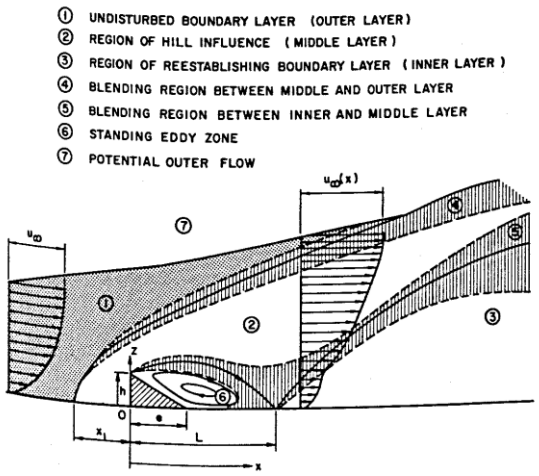

FIG. 5. Schematic of the model showing the flow regions of a boundary layer affected by a wedge shaped shelter belt on a flat plate. (Schematic taken from Plate[54])

Fig. 5)—the upstream and downstream wake—have the greatest affect on sheltering. Plate describes the region downstream of the object as a type of separation bubble in which a low velocity standing eddy zone is created. This region is bordered by the ground, the vertical barrier, and a high velocity separation streamline that extends from the top of the shelter to reconnection point on the ground a distance away (also called the Coanda effect) that is determined by the barrier's porosity, the drag acting on the shelter, and the pressure distribution directly behind the barrier. This streamline border can be described as a blending of flow that is caused by the velocity gradient acting in the region. This blending determines the recovery of the wind profile and the reduction in the sheltering efficiency.

Raine and Stevenson[55] provide a basic model and description of the aerodynamics and flow behind a one-dimensional porous barrier; see Fig. 6. They present the results of tests of model shelter belts in a simulated atmospheric boundary layer in a wind tunnel. A separated flow or shadow zone is created in the leeward side of the wind break. The size and effect of this zone is dependent upon the approach velocity, the drag force exerted on the flow field, the bleed

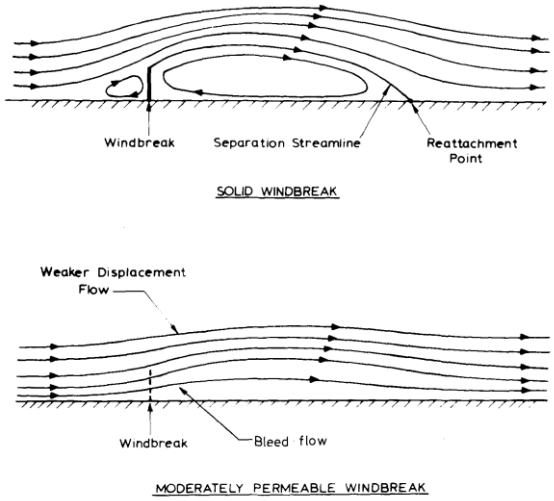

FIG. 6. Streamline sketches for airflow through a 2-D windbreak. The top sketch shows the airflow for a solid wind break or wall with no porosity and the bottom depicts a windbreak with medium porosity. (Sketches taken from Raine and Stevenson[55])

through due to the shelter's permeability, Reynolds-number, and drag coefficient. It's specifically noted that as the permeability is reduced, bleed through is also reduced, the drag force increases, and the strength the turbulent eddy in the separation zone is increased. Low permeability results in a steeper or faster return of the displacement flow to the ground at its downstream reattachment point, which is again dependent on the Reynolds-number, drag coefficient, and the flow. The authors found that the best permeability is between 20-50% depending on the relative height of the barrier. In general, it is agreed that the shelter's porosity has the strongest affect on turbulence reduction, and that a denser or a less permeable shelter belt will increase the amount of eddying and turbulence on the lee side of the barrier.

Agricultural research, like the two studies just presented, and current research with wind barrier enclosures show that various flow regions behind the barrier, characterized by different velocity gradients, are created from the interaction of the turbulent flow and the barrier's aerodynamics. Since these "interaction zones" determine the physical location of the barrier's

sheltering effects, it is important to understand and identify them. The number of zones, their size, location relative to the barrier, and characteristics of the flow gradients are dependent on the incident turbulence and the barrier's aerodynamic characteristics—such as porosity.[41, 56] Plate[54] and Dong, Luo, Qian, and Wang[56] identified seven zones that are most influenced by turbulence and wind speed reduction, while ReVelle[50] only identified five. In general these zones can be identified as 1) an upstream region where the boundary layer is relatively undisturbed or minimally influenced. 2) A small eddy region or separation zone directly behind the shelter characterized by a standing eddy, minimum turbulence, and minimum flow speeds. It is bordered by the ground, the barrier, and a separation stream line that extends from the top of the barrier to a reattachment point on the ground. 3) A transition region that sits between the separation zone and the undisturbed boundary flow that passes over the top of the barrier. It is characterized by a blending or mixing of flows and is bordered by the separation streamline. 4) An overflow region, where the flow boundary layer flow passes relatively undisturbed over the barrier. 5) A low velocity boundary layer flow region that forms downstream of the separation streamline reattachment point. This region is characterized as being a boundary layer flow, but initially with a lower velocity than the undisturbed boundary layer flow. The velocity and thickness for this region gradually increase until it matches and joins the undisturbed boundary layer flow.

B. Current wind barriers and wind barrier design

It is important to determine whether the wind-noise for infrasonic frequencies is diminished or increased by the wind fence's modification of the wind flow and the turbulence.

Agricultural models are fairly exhaustive in the treatment of how a two dimensional wind barrier modifies the turbulence but still have their limitations. The models focus on how the modified turbulence will affect the microclimate on the leeward side of a two dimensional wind barrier and not on how the modified turbulence effects wind noise generation. Further, the models are largely limited to two dimensions and do not address the effects that occur inside an enclosed structure. The agricultural models and studies that do consider the effects inside an enclosed structure, such as Argete and Wilson,[57] often used structures that are larger, more open, and have significantly greater length to height ratios than the wind barrier envisioned for this research. However, there are wind noise studies for enclosed fence structures that consider how the general porosity and shape affects the turbulence and infrasonic noise reduction. Several of these models are discussed in the following.

Raspet and Hedlin[7] investigated if an infrasonic noise reduction device with a smaller spatial footprint—such as a porous fence or barrier—can give comparable levels of noise reduction to rosette spatial filters. They evaluated the design patented by Ludwik Liska[58] in 1975, which is a 50% porous hexagonally shaped barrier with horizontal wooden slats. They also modified the design by covering the slats with a thin mesh screen for some of the measurements; see Fig. 7. The barrier was 5 m in diameter and 2 m high, and was compared against an 18 m and a 70 m rosette spatial filter. They observed that the barrier performed better than the spatial filters for the 1-5 Hz frequency band, but performed worse than the filters for frequencies below 1 Hz. They did note that the barrier's reduction was comparable to that of the two spatial filters if the results are scaled by the size of the device. This suggests that the barrier can be described by scaling laws and may, like a spherical windscreen, cause noise reduction by area averaging the pressure fluctuations over its surface area, as discussed previously on page 19.

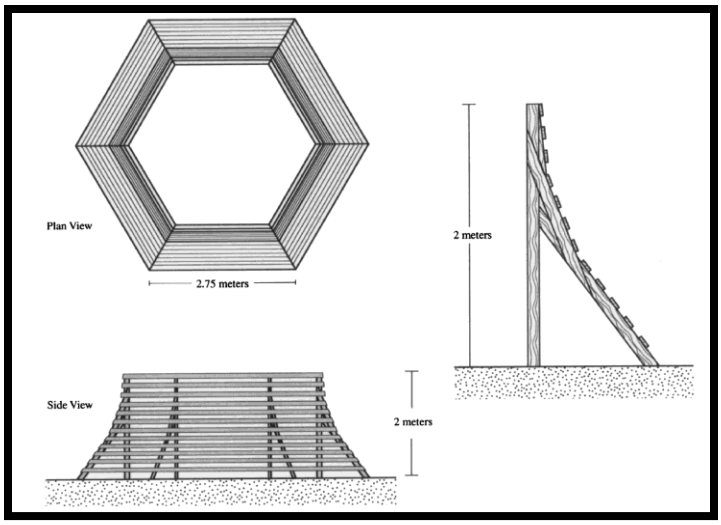

FIG. 7. Wind barrier patented by L. Liszka in 1975, and used by Raspet and Hedlin for their comparisons. The drawing is taken from the patent document. (Swedish Patent No. 7315138-3, October 30, 1975)

They also observed that like the spatial filters, the wind barrier showed large reductions only when the scale size of the turbulent wavelengths were smaller than its height. However, unlike the spatial filters, which are ineffective for turbulence wavelengths greater than the size of the rosette, the barrier achieved about 4 dB of reduction for turbulence scales up to 20 times the barrier's height. The authors concluded that a wind barrier based more on the design of the reduction principals of a spherical foam windscreen will result in a compact and effective infrasonic wind-noise filter.

ReVelle[50] presented an overview of work in wind noise reductions for the International Monitoring System (IMS) Infrasound Network's monitoring stations, including an investigation at Los Alamos National Laboratory to derive two models that describes wind noise reduction. The first model is a set of 2-D numerical airflow calculations through porous shelters using the Navier-Stokes equations. The second model describes the meteorological structure of the surface boundary layer and its defining parameters of the mean, steady state boundary layer

depth, and Monin-Obukhov similarity theory. ReVelle's models showed that noise will increase as porosity decreases because of the presence of a turbulent back eddy which forms on the leeward side of solid walls. Conversely, the models showed that noise will also increase if the turbulence sheltering influence is reduced by the wind fence being too porous. The ideal is to have a mid-level porosity which maximizes the sheltering effect while minimizing the effect of the turbulent back eddy. Mid-level porosities also lead to a reduction of the barrier's drag and drag coefficient, a reduction in the turbulent intensity levels at higher frequencies, a smaller reduction in the mean wind speed passing through the barrier, and a more gradual recovery to upstream conditions in the far wake. The models also showed other benefits for a shelter with mid-level porosity. These benefits include a systematic increase in the wake speeds, the mean speed minimum moving further downstream, and less shearing in the flow. There is also less shearing at the top of the enclosure ($z = H$), therefore resulting in a weaker downward momentum transport from the displacement flow. Finally, the shear instability effects are reduced, the induced pressure drop decreases, and the downstream reattachment point to the ground for both the flow separation streamline and the stagnation point occur closer to the barrier. ReVelle concluded that the best sheltering and wind speed reductions occur for barriers with 50% porosity and near-neutral meteorological flow conditions.

ReVelle's presentation also reviewed the wind barriers designed and constructed by L. Liszka (shown in Fig. 7), by A. Bedard of NOAA in Boulder, CO (see Fig. 8), and by D. Christie of the Australian National University in Canberra, Australia (see Figs. 9 and 10). ReVelle compared the effectiveness of Liszka's barrier against the effectiveness of a 12 porous hose 30 m diameter spatial array. There was noticeable improvement over the array, with lasting noise

FIG. 8. Turbulence-reduction device designed and used by A. Bedard and NOAA for tornado detection. A micro-barometer is located at the center of the structure. The structure is 15.25 m in diameter and 1.8 m in height, and covered in green porous fencing material. (Picture taken from Bedard et al.[52])

reductions of 5 to 8 dB for frequencies at 6 Hz and greater for all wind speeds, and a reduction of 4 to 5 dB between 0.5-2 Hz for wind speeds below 4 m/s.

ReVelle next discussed a turbulence reducing infrasonic shelter designed by A. Bedard of the NOAA in Boulder, CO. This design is a circular single walled barrier; about 15.25 m in diameter, 1.8 m high, with vertical corrugation at the top of the walls, and covered in green porous fencing material. Bedard, Bartman, Keane, Welsh, and Nishiyama[45] state that the fence reduces wind noise by raising the atmospheric boundary layer and the corrugations at the top break up the wind shear layer into small random eddies. The design helps prevent turbulence forming at lower levels behind the walls due to the flow passing over and inside a horizontal boundary normal to the edge. ReVelle's presentation does not give any information about this design's effectiveness, nor does the paper by Bedard et al. where the design is introduced.[52] However, its effectiveness is discussed in a study by Clauter[59] (see page 41).

The third design reviewed by ReVelle is a turbulence-reducing enclosure with serrated walls, designed by D. Christie of the Australian National University in Canberra, Australia. This

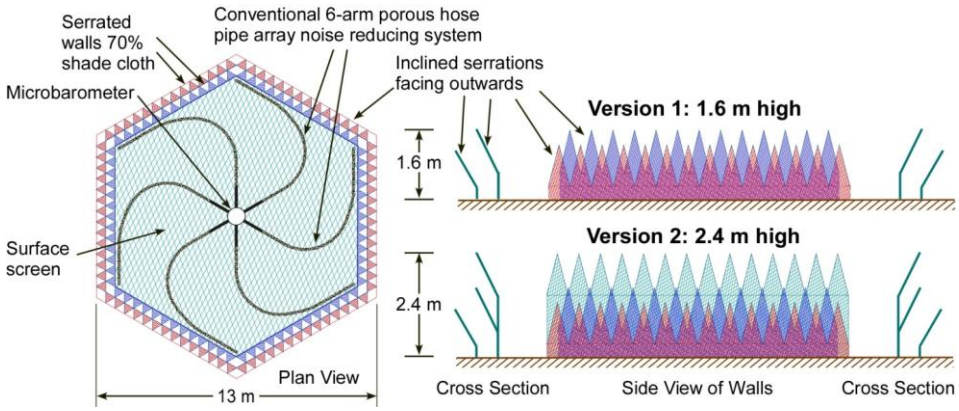

FIG. 9. Schematic design of the fourth version of D. Christie turbulence-reduction wind barrier. (Picture taken from D. ReVelle presentation[50])

FIG. 10. Side and close up views of the fourth version of D. Christie turbulence-reduction enclosure. Structure is made of porous fence material, and multi-walled, with serrated outwardly pointing walls. (Pictures taken from presentation by D. ReVelle[50])

design of a turbulence reducing enclosure differs from Bedard's in that it has multiple walls, a surface noise reducing screen stretched over the top of the enclosure, and the serrations are outwardly inclined from the center of the enclosure. The enclosure is also hexagonally shaped instead of circular, resembling the Liszka design (see Figs. 7, 9, and 10). This design was tested by comparing the measured wind noise from a 6-arm porous hose array set inside the enclosure

and a second identical array set outside the enclosure. The tests report that there is a noise reduction of two orders of magnitude at 1.0 Hz for average wind speeds of 4.5 m/s for the combined system. Christie also developed other versions of this turbulence-reduction enclosure, which are not reviewed here, but obtained reductions of up to four orders of magnitude at higher frequencies.[53]

The models just presented approach wind screening design on the theory that wind noise reduction is best achieved by lowering the turbulence without significantly creating more shearing effects. This is accomplished by modifying the enclosure's porosity, physical shape, or number of walls. A different approach to infrasonic wind screening was pursued by Shams, Zuckerwar, and Sealy[60] and by Zukerwar, Shams, Ahuja, and Funk.[61] They studied the use of small non-porous windscreens made of a material with a low acoustic impedance ratio between the material and air for infrasonic wind noise reduction. They proposed this idea on the principle that infrasonic wavelengths will penetrate any barrier of any practical thickness; therefore a nonporous wall will block any turbulence induced pressure fluctuations while allowing the transmission of infrasonic acoustic waves. The effectiveness of the design and materials—balsa wood, non-porous polyurethane foam, and Space Shuttle tile material—were tested by comparing the noise reduction for a screened and unscreened microphone place in a wind tunnel at constant wind speeds at 9.4 m/s. They also tested for infrasonic transmission loss using a sub woofer. The tests showed the foam and balsa wood to have the best noise reductions of about 20 dB at 10 Hz and 10 dB at 0.7 Hz; lower frequencies were not tested. Transmission loss tests showed the foam and balsa wood perform worse at audible frequencies (>20 Hz) with 15-25 dB loss, but then have a gain for frequencies 10-20 Hz; the tested frequency band was limited to 10-100 Hz. The tile had a uniform zero decibel transmission loss for all frequencies.

The authors concluded to have achieved their goals; however their conclusions are limited for two reasons. First, they did not perform any wind noise tests in a turbulent outdoor flow. Eliott,[33-34] Webster et al.,[62] and Morgan[1, 2] have shown that outdoor measurements under the influence of the atmospheric surface layer are very different from indoor measurements; therefore any experimental results determined in a wind tunnel cannot be applied to outdoor wind noise, or at least must be confirmed by outdoor wind noise studies. Second, low impedance materials will transmit the low frequency wind noise pressure fluctuations with low attenuation, just as they transmit the acoustic pressure fluctuations with little attenuation. In addition, the non-porous materials will create shears along the exterior, resulting in high wind noise levels as argued in the Introduction (Chapter I) and further discussed in Chapter III.

C. Aspects of Wind Barrier Design

Christie, Liszka, Bedard, and others have argued that detailed modifications to a simple fence will lead to large reductions in wind noise. It is therefore important to review research which indicates that these modifications may not be justified. The following section will examine the sensitivity of turbulence and flow to geometries, size, and other details in design and construction for windscreens.

Shields,[63] studied the correlations between wind velocity and pressure sensed in a three axis microphone array, with a simple "pill" shaped bimorph infrasonic pressure sensor that he designed. The design was shown to be insensitive to the direction of flow when he compared the spectra of multiple sensors oriented in different directions relative to the wind's direction. Shields also compared the sensor's frequency response to that of a "quad-disc" developed by

Nishiyama and Bedard.[64] The quad-disc is a static pressure probe designed to measure pressure independent of wind direction and magnitude. It consists of two pairs of thin circular disks mounted around a vertical tube or stem with a precise arrangement of holes around the central cylinder. Shields' comparisons of the bimorph sensor and a B&K ½ inch microphone sealed inside the axial tube of a quad-disc showed strong agreement between the respective measured pressure spectra. The strong agreement shows that the bimorph was comparable to the quad-disc. Shields' findings suggest that the disc structure resulting from careful design and extensive wind tunnel measurements did not provide any additional wind noise attenuation in the infrasonic frequency range over a simple vented enclosure.

Webster, Raspet, Yu, and Prather[62] investigated the effectiveness of aerodynamically designed probes when used for measurements in outdoor turbulence. Probes, such as the ones developed by Elliot,[33-34] Fuchs,[35] and Nakamura et al.,[65-66] are designed to lower measured wind noise by reducing the stagnation pressure by aerodynamically streamlining the probe for a single direction. This design optimizes these types of probes for use in wind tunnels. However, the effectiveness of these probes declines significantly when measuring outdoor turbulence. Webster et al.[62] hypothesized that this ineffectiveness is due to a strong susceptibility to the stagnation pressure generated by turbulent cross flows, which are a characteristic of the outdoor turbulent boundary layer. Webster et al. also developed predictions for the stagnation pressure spectra due to turbulent cross flow and compared the predictions to the measured pressure fluctuation spectra of four different probes. The outdoor measurement display strong agreement with the predictions. This suggests that aerodynamic streamlining of a probe or structure is not advantageous for wind noise reductions.

Clauter[59] compared the noise reduction of a 100 foot diameter porous hose array spatial filter to the 50 foot diameter wind fence barrier designed by Bedard et al.,[51-52] and a combined system consisting of the porous hoses coiled up inside the barrier. The pressure was measured using a Chaparral sensor. All three pressure spectra were plotted using a decibel scale relative to 1 μPa and measurements were performed in high and low wind speed conditions. Details regarding wind speed, measurement length, and if the measurements were done simultaneously were not included in the presentation. The porous hose array performed the best at all frequencies for both high and low wind speed conditions. In low wind speed conditions the porous hose array was about 8 dB lower than the wind fence and about 1-3 dB lower than the combined system. For high wind speeds, all three filtering systems performed worse, however the porous hose array was generally about 10-20 dB lower than the wind fence, and about 1-3 dB lower than the combined system at high frequencies and 5-8 dB lower at low frequencies. Clauter concluded that the principal determining factor for wind noise reduction is the size of the area over which the spatial averaging occurs. This suggests that the effect of any other modification is negligible. It was also suggested that since the size of the turbulence passing over and inside the top of the fence was so much greater than its height, the turbulence could reach the pressure sensor at the center of the fence unimpeded. Clauter further concluded that smaller, more compact wind fences offer no advantage to infrasonic wind noise reduction. However, there may be promise in combining the wind fence with porous hoses or some other filter.

Wilson and White[67] found turbulence, flow management, and noise reduction to be insensitive to the geometries and detailed designs for a porous windscreen. They used a fluid flow computer simulation to test windscreen design in terms of shape, size, and flow resistivity.

Assuming an incompressible fluid, Wilson and White calculated the pressure and fluid flow using the Navier-Stokes equations for open fluid flow and the Zwikker-Kosten equations for flow through the windscreen pores. The simulation consisted of sending a single vortex pulse, 1.5 s long, through a simulated windscreen. The mean flow speed for the pulse was approximately 1.0 m/s and the Reynolds number for the flow was approximately 13000. To test the effects of a windscreen's geometry the authors used three different shapes—spherical, square, and "aerodynamic" or oval—with each having the same cross sectional area (20 cm in diameter) relative to the turbulent flow. To test the size and resistivity effects, or porosity, of a windscreen in a turbulent flow, three different sizes (5, 10, and 20 cm diameters) and three different flow resistivities (10 Pa s/m^2, 100 Pa s/m^2, and 1000 Pa s/m^2) were used for the spherically shaped windscreen. The simulations showed that the length of the turbulent wake zone behind the screen increased from approximately two times the screen's diameter to three to four times the diameter as the windscreen flow resistivity decreased. The simulations also showed that pressure was consistently minimal at the windscreen's center and tended to decrease as both the windscreen flow resistivity decreased and as the diameter increased. Of the two, the size had the most dramatic effect. Finally, Wilson and White showed that the change in the overall shape of the windscreen did not modify the pressure at the center or the length of the turbulent wake zone. The authors concluded that larger windscreens are more effective, a higher flow resistivity would not improve the reduction much but may affect the acoustics, and that a more aerodynamic shape does not lead to significant additional wind noise reduction.

Xu, Zheng, and Wilson[68] also explored the effect of different windscreen geometries and flow resistivities in optimizing windscreen performance for reducing drag, resistance, and leeward turbulence in a turbulent flow. The test was done by performing a computational

experiment comparing three 2-D geometrical shapes and three flow resitivites, or porosities, for a windscreen under turbulent flow conditions with a Reynolds-number of approximately 5000. The authors acknowledge that this is much lower than atmospheric turbulence which has a Reynolds number on the order of 10^5 and greater. The limitation is due to computational restrictions. However, the authors state that the simulation is still informative since the flow is turbulent, and that it is a step towards understanding more complicated flows. Assuming an incompressible flow throughout the fluid, the pressure and open fluid flow were calculated using the Navier-Stokes equations. The pressure and flow through the porous media was determined using the Zwikker-Kosten equations. The mean flow speed was approximately 1.0 m/s. The three windscreen shapes were circular (D = 7.5 cm), elliptical (semi-major diameter = 15 cm, semi-minor diameter = 3.75 cm), and rectangular (height = 15 cm, width = 3.75 cm). Both the maximum and minimum cross sectional areas for the elliptical and rectangular screens were tested by setting the semi-major axis of both screens vertically and horizontally relative to the flow. The three windscreen resistivities were 17, 170, and 1700 Pa s/m^2. The authors concluded that an elliptically shaped wind screen with medium (170 Pa s/m^2) resistivity (porosity) and with the semi-major axis set horizontally to the flow had the best overall reduction. However, it was also noted that both the circular and horizontally set rectangular screens produced comparable reductions. This is similar to the findings of Wilson and White.[67]

Ballard and Izquierdo[69] investigated the gains in wind noise reduction when windscreens are concentrically combined to form a single multi-layer windscreen. They constructed two multi-layer windscreens. The first was made of three concentric cylinders and the second was made of two concentric hemispheres. The two exterior layers were made of #14 copper wire mesh and the innermost screen was made of acoustic cloth. The diameters of the windscreens

were 0.62 m, 0.84 m, and 1.06 m respectively. They found that the acoustic signals were not attenuated, and that the multi-layer windscreens achieved better noise reduction than a large scale Daniels pipe array. They also found that the hemispherical windscreens performed better than the cylindrical windscreens. Finally, they determined that noise reductions improved as successive layers were added to the windscreens.

A large structure in a flow may introduce different types of flow-induced vibrations, such as Vortex-Induced Vibrations (VIV). VIV can contribute to the generation of lee-side turbulence and may lead to resonance vibrations and wind noise caused by vortex and wake shedding. Studies on different methods for reducing and controlling VIV can give us insight into the control or elimination of wind noise contributions due to flow induced vibrations and wake shedding. Kumer, Sohn, and Gowda[70] presented an overview of the different types of passive control devices or methods used to reduce Vortex-Induced Vibrations acting on a structure in a flow. The authors described eight types of passive control devices that can be used to reduce the

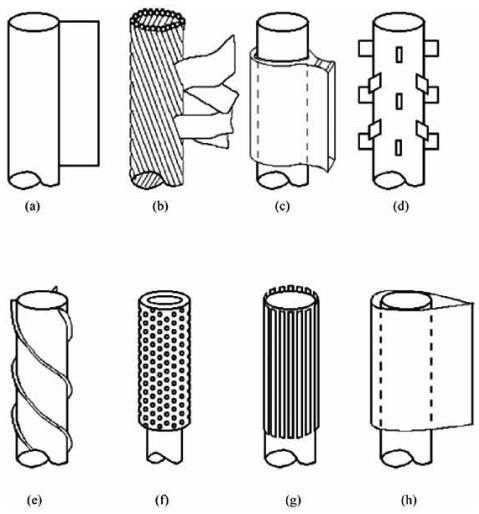

FIG. 11. Passive control devices presented by Kumar et al.: a) wake splitter, b) ribbons or hair cables, c) guide vanes, d) spoiler plates, e) helical strakes, f) perforated shroud, g) axial shroud, and h) streamlining. (Image taken from Kumer et al.[70])

effect of these vibrations, see Fig. 11. These passive control devices are 1) a wake splitter; 2) ribbons or hair cables; 3) guide vanes—which are a type of stream-lined structure set around the column but with a relatively bluff trailing edge, instead of a tapered trailing edge, and a shorter body. 4) An array of spoiler plates mounted onto the cylinder or column. 5) Helical strakes or ribs that run over the column, and have a height about 0.1 times the diameter, D, of the column and a pitch of about 15D. 6) A perforated shroud; 7) an axial slat shroud—vertical slats set about the column; and 8) a stream-lining structure geometry set around the column. Of these different techniques the axial shroud is very similar to the design of the wind fence in this dissertation. The axial shroud is a device that suppresses the formation of vortex shedding. It works by affecting the entrainment of the irritational flow, which is necessary to induce vortex shedding, in such a way that it prevents the formation of any type of oscillating flow. Modifications of these techniques may be useful should wake shedding prove to be a contributing noise source.

The literature presented so far has shown that windscreen size and porosity have the most effect on noise reduction. However, it may prove beneficial to consider if the porosity of the walls should be uniform and if the walls should extend to the ground or if the presence of a small bottom gap and non-uniform porosity will change the noise reduction.

Park and Lee[71] investigated the effects of a bottom gap and non-uniform wall porosity on wind flow, pressure, and turbulence behind a 2-D wind fence barrier. They examined the power spectral densities of the pressure, mean and rms wind flow, and turbulence for four different gap sizes, with gap to height ratios of G/H = 0.0, 0.125, 0.25, 0.375, and 0.5. They found that the pressure and turbulence spectra behind the wind barrier were significantly reduced for $G/H \leq 0.125$. They also determined that a small bottom gap at the base of the fence was better than no

gap. However, they also found that turbulent flow and pressure increased for G/H ratios larger than 0.125. Park and Lee investigated the effects of non-uniform porosity by first holding the bottom half of the fence at 40% porosity and varying the top half with 0%, 20%, 30%, 40%, and 65% porosities, and then switching the conditions, holding the top half constant and varying the bottom half. They showed that the flow behind a non-uniform wall was very unstable due to the mixing of the different flow velocities and bleed through, while the flow for a uniform fence was much more stable. Similar results were found by Kim and Lee[72] who concluded that the turbulence for the three principal flow regions formed behind the windscreen—an upper and lower shear layer developed by separation at the fence top and bottom gap, and a bleed flow passing through the fence itself—was lower for small to no bottom gaps since mixing was minimized.

The results described in this chapter will be used to design a wind fence to test our theories and assumptions. The theory, design criteria, and physical description are given in the next chapter.

CHAPTER III

CONCEPTUAL THEORY, DESIGN CRITERIA, AND PHYSICAL DESCRIPTION OF WIND FENCE ENCLOSURE

A conceptual theory for designing a wind noise reducing fence enclosure can be developed from a synthesis of the ideas presented in the Literature Review (Chapter II). The theory will allow us to determine the physical characteristics and mechanisms that lead to noise reductions for a wind barrier placed in a turbulent flow, and the steps that should be taken to optimize the barrier's design. The first part of this chapter will present and discuss this theory. The second part of the chapter will present the design criteria for a wind fence to test our assumptions and theories. Finally the chapter will present the physical description of the experimental wind fence.

1. Conceptual Theory

Wind fence enclosures are turbulence reduction devices that are typically large and cylindrical in shape. Even though there has been little theory developed specifically for wind fence enclosures, the theory for wind noise reduction by compact spherically shaped windscreens has been thoroughly investigated. The results and data from Strasberg's investigation of

cylindrically shaped hydrophones and spherically shaped windscreens, [29-30] and from Hedlin and Raspet's investigation of the Liszka wind barrier[7] suggest that wind noise reduction for a wind fence enclosure is caused by the same mechanisms as a windscreen. Therefore, the theories describing noise reduction by a windscreen may be applied to a wind barrier.

Like a windscreen, wind fence enclosures produce wind noise reduction by acting as a pressure fluctuation averaging device and should follow similar scaling laws. A wind fence enclosure produces noise reduction by eliminating the direct turbulence interactions with the microphone and transferring the noise generating interactions to the surface of the wind barrier. This increases the incoherence of the wind noise measured by the microphone by expanding the size of the microphone averaging area. It also increases the distance between the surface of the wind barrier and the microphone. Further, according to scaling laws, expanding the size of the device should shift wind noise reductions to lower frequencies—improving the reductions at low frequencies.

A wind fence enclosure also interacts with the turbulence flow by raising the atmospheric turbulent boundary layer and modifying the velocity gradient immediately adjacent to the ground. This interaction and other interactions between the wind barrier and the flow, such as the generation of vortex and wake shedding, determine the generation and suppression of turbulence and noise. To better examine how these interactions affect a barrier's capability to suppress wind noise as a pressure-averaging device the flow will be separated into three identifiable regions: I) the flow inside the barrier, II) the flow adjacent to and behind the barrier, and III) the undisturbed flow; see Fig. 12. This is simplified from the five and seven region descriptions found in Chapter II.

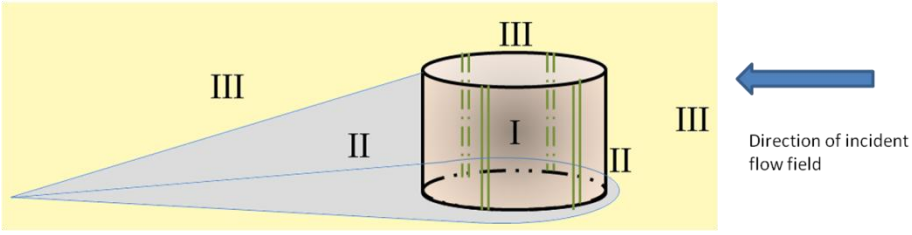

FIG. 12. Sketch depicting the location of the three source regions relative to the enclosure. Wind flow direction is from right to left. Region I is the flow located inside the barrier, Region II is the flow immediately adjacent to and behind the barrier, extending to a point downwind of the barrier where the separation flow line reconnects with the ground. Region III is the undisturbed flow. The sketch is not drawn to scale.

The first region is the flow that passes inside the wind fence enclosure; where the flow speed is very low, and the shapes of the velocity profile and velocity gradient can be estimated using the mathematical form of summed exponentials, $u = u_0\left(1-\sum_{i=0}^{n} A_i e^{-\beta_i z}\right)$. Assuming that the microphone is mounted flush to the ground and covered by a sheet of foam, the wind noise generated in the interior of the wind fence is principally caused by the turbulence-turbulence and turbulence-shear flow interactions at the microphone. It is possible that wind noise can also be generated by self-induced cavity turbulence from re-circulating air and turbulence passing over and inside the enclosure's top edge. The magnitude of these secondary noise contributions is assumed to be negligible but will be considered in the analysis of the data.

The wind noise from this region can be estimated using Jiao Yu's[36] calculation to predict wind noise from the measured turbulence and non-logarithmic velocity profile over flat open ground:

$$\left|P_I\left(0,k_1\right)\right|^2 = \frac{440C\lambda^4\rho_0^2k_1^2}{9\pi} \sum_{i=0,j=0}^{i=n,j=m} s_i s_j e^{\left(\beta_i+\beta_j\right)d} \int_0^\infty\int_0^\infty \frac{dk_2dk_3}{\left[1+\left(k\lambda\right)^2\right]^{\frac{17}{6}}} \left[\int_d^h e^{-\left(\kappa+\beta_i\right)x_2}\sin\left(k_2x_2\right)dx_2 \int_d^h e^{-\left(\kappa+\beta_j\right)x_2'}\sin\left(k_2x_2'\right)dx_2'\right] \quad (11)$$

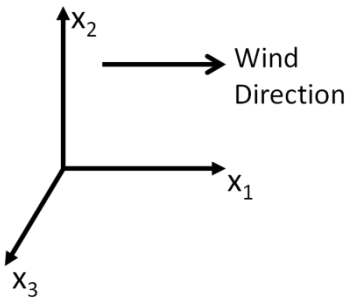

FIG. 13. Coordinate system used in Yu's logarithmic and multi-exponential models.

where h is the height of the wind enclosure, ρ_0 is the air density, and d is the thickness of the foam. The value, k, is the wavenumber vector, or $k = \sqrt{k_1^2 + k_2^2 + k_3^2}$, and κ is the magnitude of the wavenumber vector in the plane parallel to the ground, or $\kappa = \sqrt{k_1^2 + k_3^2}$. The wavenumber, k, is determined from Taylor's frozen turbulence hypothesis: $k = 2\pi f/U_c$, where f and U_c are the measured frequency and wind velocity, respectively. The values of 1, 2, and 3 indicate coordinates with respect to the direction of flow; where 1 and x_1 are longitudinal or in the direction of the flow, 2 and x_2 are in the vertical direction, and 3 and x_3 are transverse to the direction of flow (see Fig. 13). The values s_i and s_j are defined as the following:

$$s_j = U_0 \beta_j A_j \quad j = 0,1,\ldots,n-1, \tag{12}$$

and where U_0, A_j, and β_j are derived by fitting the measured wind velocity profile to the mathematical form of summed exponentials:

$$U = U_0\left(1 - \sum_{i=0}^{n-1} A_i e^{-\beta_i x_2}\right). \tag{13}$$

The C and λ terms from Eq. (11) are fitting parameters that are determined fitting the product of k_1 and the measured velocity spectrum to the product of k_1 and a velocity spectrum similar to the von Karman spectrum for a free jet:

$$k_1 F_{11}^1(k_1) = \frac{Ck_1}{\left[1+(k_1\lambda)^2\right]^{\frac{5}{6}}}. \qquad (14)$$

C is a measure of the magnitude of the spectrum in the source region and λ determines the transition from the source range to the inertial range of the spectrum.

The second region is the flow that interacts with the surface of the wind fence enclosure. This region also encompasses the flow that passes to the leeward side of the enclosure, extending downwind until a point where the separation flow that forms at the top of the enclosure reconnects with the ground and the shape of the velocity profile becomes approximately logarithmic. The wind noise generated in this region is principally due to the pressure fluctuations from the stagnation pressure and the turbulence-shear interaction at the enclosure's surface. Noise in this region may also be due to wake shedding and vortex shedding, however, this is unlikely since, as shown by Kumar et al.[70] in the Chapter II, the porous wind fence enclosure is similar to the axial shroud and perforated shroud vortex suppression devices. These devices work by affecting the entrainment of the irrotational flow, which is necessary to induce vortex shedding, in such a way that it prevents the formation of any type of oscillating flow. Analysis of the data will verify if this is true. Currently, there is no mathematical model to estimate the wind noise contribution for this region; however one will be derived in Chapter V.

The third and final region is the undisturbed flow away from the wind fence. This is the same as the flow field over open ground where the velocity profile is logarithmic, $u = (u_*/k_a)\ln(z/z_0)$. Wind noise for this region is due to only the turbulence-turbulence and turbulence-shear interactions, since these interactions are intrinsic to the flow. Like Region I, the noise contribution for this region can be estimated using Jiao Yu's calculation to predict wind noise from the measured turbulence and velocity profile over flat open ground. However, since

the velocity profile follows the logarithmic law, the noise contribution is best estimated using a logarithmic model:

$$\left|P_{III}\left(0,k_1\right)\right|^2 = P_{III}\left(0,k_1\right)P_{III}^*\left(0,k_1\right) = \frac{440a^2\rho_0^2k_1^2C\lambda^4}{9\pi}\int_0^\infty\int_0^\infty \frac{dk_2dk_3}{\left[1+\left(k\lambda\right)^2\right]^{\frac{17}{6}}}\left[\int_d^\infty \frac{e^{-\kappa x_2}\sin\left(k_2x_2\right)}{x_2-d+x_0}dx_2\int_d^\infty \frac{e^{-\kappa x_2'}\sin\left(k_2x_2'\right)}{x_2'-d+x_0}dx_2'\right] \tag{15}$$

where the C, λ, ρ_0, x_2, k_1, k, and κ terms are the same as in Eq. (11). The d term is the thickness of the foam sheet covering the pressure sensor, x_0 is the aerodynamic roughness length, and a is related to the surface stress. Both the a and x_0 terms are determined by fitting the measured wind velocity profile to the logarithmic profile law:

$$U(x) = a\ln\left(\frac{x_2-d+x_0}{x_0}\right). \tag{16}$$

The interaction between the wind fence enclosure and the flow in these three regions are directly affected by the aerodynamics of the enclosure, which is determined by the enclosure's wall porosity, height, diameter, overall shape, the presence of a bottom gap, the condition of an enclosed or open top, and the number of porous layers separating the flow from the microphone. How these characteristics and aerodynamic properties influence the stagnation pressure, the turbulence-turbulence interaction, and the turbulence-shear interaction for the three identified flow regions, as well as the generation of any wake and vortex shedding will determine the barrier's effectiveness at wind noise reduction.

As discussed in the introduction, the porosity determines the amount of noise generated by the stagnation pressure and the turbulence-shear interaction at the wind fence enclosure's surface. It also determines the generation of back eddies, vortices, and the size of the turbulent shadow zone that forms behind the enclosure. The porosity also determines the shape of the

wind velocity profile and the turbulence spectra in the interior of the barrier, which affects the turbulence-mean shear interaction in the vicinity of the microphone. Finally the porosity affects the speed of the flow inside the barrier and any re-circulating turbulence. Like the porosity, a bottom gap affects the turbulence-mean shear interaction in the vicinity of the microphone and the shape of the velocity profile inside the enclosure. A closed or open top affects the amount of turbulence that reaches the interior by passing over and inside the barrier's top edge. This also affects the extent of the flow separation due to shearing at the barrier's top edge. Both the height and diameter, as potential characteristic dimensions for scaling laws, affect the magnitude and frequency range at which noise reduction occurs. The dimensions also determine the magnitude of the turbulence passing over and inside the top edge, and the shearing and flow separation that also occur at the enclosure's top. Multiple layers modify the flow speed and velocity gradient so that the turbulence-shear interaction at the microphone is minimized without causing additional shearing at the barrier's most external surface.

In conclusion, wind noise reductions are most affected by the wind fence porosity, number of layers, size, roof, bottom gap treatments, and the generation (if any) of wake and vortex shedding. The purpose of this research is to determine the design that optimizes wind noise reductions by a wind fence enclosure. Hence, this investigation will examine how and to what extent these characteristics and interactions affect the wind noise reduction for a wind fence enclosure.

2. Design Criteria

It is assumed that the wind noise reduction in turbulent outdoor flow is not sensitive to flow management details since research has shown that audible-frequency wind noise reduction

devices are insensitive to such details in their design, such as aerodynamic shaping and additive features, when used in turbulent outdoor flows. To validate this assumption and the theory presented in the first part of this chapter a simple wind fence was designed and both acoustic and flow measurements were used to determine if the design can benefit from additional structures to manage wake shedding or vibration. The principle effect on a detailed structure would be to modify the flow behind and within the wind fence enclosure, if needed.

The design of the experimental wind fence should be simple, with uniform sides if the geometrical shape is non-circular. The specific geometry is not as important as long as the porosity and size of the panels are azimuthally uniform so that the wind noise reductions will be independent of the wind direction. The fence should have a small bottom gap ($G/H < 0.125$) to minimize the shearing gradient in the interior.[71-72] The bottom gap should be easily opened or closed without varying the overall height of the fence. A porous roof, that can easily be removed as needed, is also desirable to minimize the pressure fluctuations from turbulence that enters the wind fence by passing over the enclosure's top edge. Scaling laws indicate that the overall size and dimensions should be fairly large to increase reductions at low wavenumbers. The barrier should be sufficiently tall to make any noise due to the flow separation at the top and pressure fluctuations from turbulence passing over and inside the top edge negligible. The diameter should not be too large in relation to the height since wind flow research indicates that the zone of minimized turbulence that forms in the leeward side of the fence is finite, and is determined by the height and porosity of the wind barrier.[50-51] Hence, the barrier's diameter should not exceed the size of this zone. The barrier's porosity should vary over a wide range of porosities in order to determine if an optimum exists, and if it does, what that optimum value is. Finally, the addition of a secondary barrier should be added to verify if multiple layers will improve noise

reductions, since Ballard and Izquierdo[69] showed that wind noise decreased as successive layers of concentric windscreens were added together.

3. Physical Description of the Wind Fence Enclosure

The initial wind fence enclosure design chosen for testing was a ten-sided cylindrically shaped enclosure measuring approximately 2.9 m high and about 5.0 m in diameter, with an open top and a 0.1 m bottom gap (G/H ≈ 0.03). Each side was constructed of chain link fence panels with vinyl privacy slats inserted vertically into the fencing. The slats can be removed or added to change the enclosure's porosity. Porosity is defined as the percent ratio of open surface area to total surface area. The individual fence panels were approximately 1.5 m wide and 2.7 m high and were made of 8 gauge 2 inch chain link; see Fig. 14. To test how the fence's physical characteristics affected wind noise reduction, the wind fence was modified throughout the experiment. The details of these modifications will be described in Chapter IV.

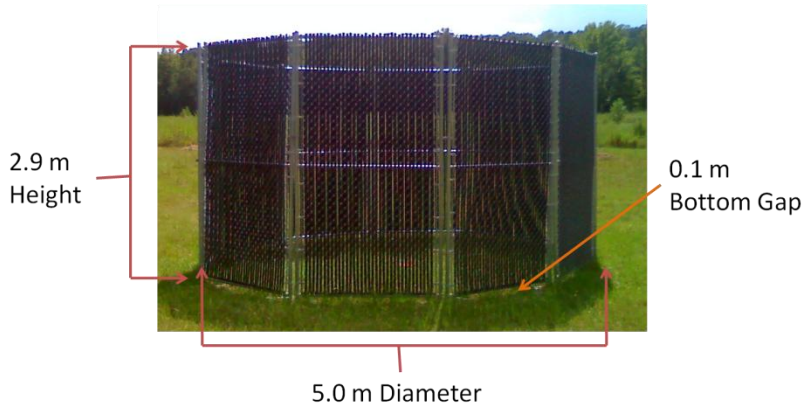

FIG. 14. Dimensions of the wind fence enclosure, 5 m width and 2.9 m height, at 30% porosity, with an open top and open bottom gap.

CHAPTER IV

MEASUREMENT SERIES AND INVESTIGATIONS

1. Introduction

This chapter describes the different measurements that were used to verify the proposed optimization characteristics and design criteria for wind noise reduction. The chapter is divided into two main sections. The first section describes the general procedures, set-up, location, instrumentation, and techniques for the measurements. The second section of the chapter provides the details describing each of the measurement series and investigations for this research, as well as the measured data and results from the investigations.

The measurements were divided into seven different series and investigations: The first investigated the effect of varying the wall porosity. The second examined the effect of modifying the bottom gap and roof treatments. The third increased the height and diameter of the wind fence, verifying if the wind fence is subject to scaling laws. The fourth measurement series investigated the effect of adding a secondary concentric wind barrier. The fifth series provides the relation between the wind noise measured by a flush mounted screened sensor and an unscreened surface mounted sensor, which is often used for wind reduction measurements. The sixth measurement series examined the wake turbulence for any enhancements and indications of vortex shedding. A separate report of this sixth measurement series is not included

in this dissertation, but is comprehensively incorporated into the reports of the first four series. The seventh investigation examined the source of an enhancement in the measured wind noise spectra that was occasionally observed during the measurement phase of this research. Even though this investigation is not considered a measurement series since it did not involve obtaining new data sets, it is considered to be a separate investigation since it has a separate focus. The investigation was conducted by comparing and analyzing the data that had already been obtained during the whole measurement phase of this research.

All measurements for this research were performed in a field near Locke Station, MS. The terrain was flat and open with mowed grass immediately around the wind fence enclosure for about 25 m to the East and West, 60 m to the North, and 80 m to the South, with harvested fields beyond these points; see Fig. 15.

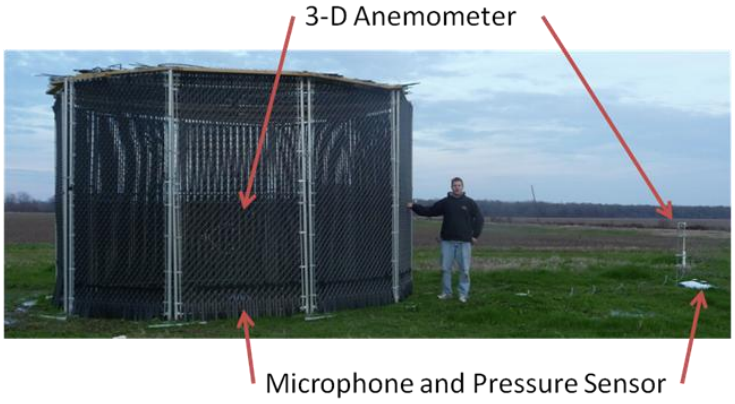

FIG. 15. General set up of the experiment showing the locations of the 3-D anemometer, microphone, and pressure sensor inside and upwind of the wind fence.

2. Procedure for Measurements

Each series measured the changes in the noise reductions, the mean velocity profile, and the turbulence energy reductions inside the wind fence as the wind barrier's physical characteristics were modified. The turbulence energy reductions on the lee side of the fence were also measured. Noise reductions were determined by subtracting the power spectra of the wind noise measured by a microphone and an infrasonic pressure sensor set at the center of the wind fence enclosure from the power spectra of the wind noise measured another identical microphone and pressure sensor set outside and upwind of the enclosure. The noise reductions were then plotted on a decibel scale, with respect to the wavenumber, k, or $WNR = 10\log\left(\frac{PSD_{Outside}}{PSD_{Inside}}\right)$. Positive wind noise reduction values indicate lower noise inside the wind fence relative to the wind noise outside of the fence, while negative values indicate an increase in the wind noise.

The microphones used in this study were Brüel and Kjær type 4193 ½" field pressure microphones, powered by a Nexus box conditioning amplifier, and set to a measurement bandwidth between 0.1 and 100 Hz. The infrasonic pressure sensors were developed by the atmospheric acoustics group at the National Center for Physical Acoustics. The sensitivity bandwidth for the infrasonic pressure sensors is between 0.02 and 175 Hz. Further details regarding the sensor's design were presented at the Fall 2011 Meeting of the American Geophysical Society.[73] Data from the microphones and pressure sensors were measured using a 16-bit National Instruments AD/DA data acquisition system and controlled by a program written

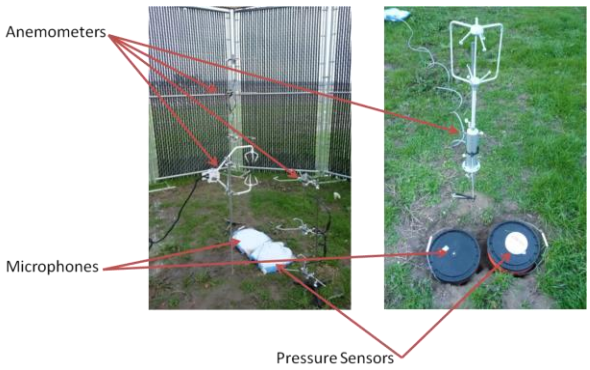

FIG. 16. General set up of the experiment showing the locations of the microphone and pressure sensors relative to the anemometers. The picture on the right shows the open field anemometer, microphone, and pressure sensor, with the foam covering removed from the microphone and pressure sensor. During measurements the covering was kept in place, as shown in the left picture. The left hand picture shows the enclosed field anemometer, the foam covered microphone and pressure sensor, and the 1-D anemometers used to measure the horizontal wind velocity profile.

in Labview©. This gave a dynamic range of approximately 96 dB. The measurement sampling rate was 200 samples/s and generally each measurement run was about 45 minutes long.

The microphones and pressure sensors were mounted under a porous sheet of foam, with the top of the foam set flush to the ground; see Figs. 15 and 16. The pressure sensors were flush mounted and covered by foam instead of the more common arrangement of placing them in the flow, unscreened and on the surface of the ground. This method was employed since the noise contribution for a screened and flush mounted sensor is due only to the turbulence-shear interaction which is better understood and more predictable than the stagnation pressure and turbulence-turbulence interactions. The fifth measurement series provides the relation between the wind noise measured by a flush mounted sensor and the surface mounted sensor.

Turbulence was measured upwind of the fence, at the center of the fence, and at three locations on the leeward side of the fence by three, 3-D ultrasonic anemometers, which were set 1.0 m above the ground; see Figs 15 and 16. Turbulence energy reductions, which demonstrate

the change in the turbulence inside and behind the wind fence relative to the turbulence upwind of the fence, were determined by subtracting the turbulence power spectra measured at the center of the fence and behind the fence from the turbulence spectra measured upwind of the fence. Like the wind noise reductions, the turbulence energy reductions were then plotted on a decibel scale, with respect to the wavenumber, k, or $TER_{Inside} = 10\log\left(\frac{PSD_{Upwind}}{PSD_{Inside}}\right)$ for the reductions inside the wind fence, and $TER_{Behind} = 10\log\left(\frac{PSD_{Upwind}}{PSD_{Behind}}\right)$ for the reductions behind the wind fence enclosure. Positive reduction values indicate lower turbulence levels for the respective locations (either inside or behind the wind fence) relative to the upwind or incident turbulence. Negative values indicate an increase in the measured turbulence with respect to the upwind turbulence incident to the enclosure. The three measurement positions behind the fence start at x = 0.3 m, and then increase to x = 2.9 m and 5.8 m. These three positions are referred to as a, b, and c, and were chosen based on their relative distance to the wind fence height, and the anticipated location of the turbulence reattachment point. The 3-D sonic anemometer set upwind of the enclosure was a Gill Instruments R3-A100 Ultrasonic Research Anemometer, and the 3-D sonic anemometers set inside and behind the enclosure were Campbell Scientific CSAT3 3-D Sonic Anemometers. The internal sampling rates for the Gill and the two Campbell anemometers were 100 Hz and 60 Hz, respectively. Data from the 3-D anemometers was measured simultaneously with the microphones. It was also obtained and controlled using the same programs and equipment.

The wind velocity profile was measured both at the center of the wind fence and outside of the wind fence using a 2.0 m vertical array of six 1-D ultrasonic anemometers, set at z = 0.1,

0.5, 0.95, 1.10, 1.55, and 1.85 m; see Fig 15. These anemometers were the individual u, v, and w branches of two Applied Technologies SAT-211/3K-probe Sonic Anemometers. The internal sampling rate for these anemometers was 10 Hz. The 2.0 m array of 1-D anemometers was controlled by a National Instruments USB to RS-232 interface and a separate program written in Labview©. The wind velocity profile inside the enclosure was measured simultaneously with the other instruments. The outside velocity profile was measured before and after each full length measurement run, for about 15 minutes, and then these two measurements were averaged together.

Before describing the different measurement series with the respective data and results, it should be noted that both the wind noise and turbulence reduction curves are plotted with respect to wavenumber instead of frequency since wavenumber is the normalization of the frequency by the wind velocity. The normalization is important since the energy in the wind noise spectra and size of the turbulence relative to the size of the wind fence is highly dependent on the wind velocity, which can significantly vary from day to day, even over the course of a single measurement day. Therefore, frequency based reductions are not comparable if the wind

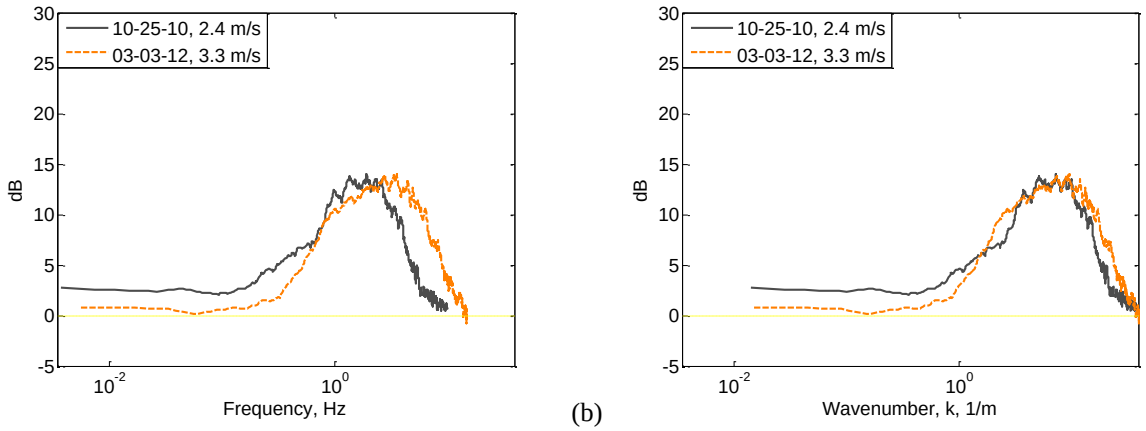

FIG. 17. Measured wind noise spectra reductions, in decibels, plotted in (a) frequency space and (b) wavenumber space, for a 55% porous fence with an open bottom gap and open top measured at two different convection velocities.

velocities for the different wind noise and turbulence measurements change or differ. Plotting the reduction comparisons with respect to the wavenumber allows the wind speed to be taken into account and isolated from the data. As an example, Fig. 17 shows how noise reduction comparisons are affected if the wind speed is not taken into account and isolated from the data. The data shown in Fig. 17 are the noise reduction curves for a 55% porous fence with an open top and open bottom gap measured on two different days, at two different convection velocities, approximately 2.4 m/s and 3.3 m/s, and are plotted with respect to (a) frequency and (b) wavenumber. The frequency plot shows a significant shift in the frequency band where noise reductions occur despite the wind velocities only differing by approximately 0.9 m/s. Therefore any comparisons to understand how physical changes to a wind fence enclosure will affect noise reductions are useless, since it would be impossible to distinguish if the effects are due to the physical changes made to the fence or are due to the differences in wind speeds. Conversely, the wavenumber plot shows changes to the reduction curves which are due only to physical changes made to the wind fence.

Data are transformed from frequency space to wavenumber space by using Taylor's frozen turbulence hypothesis, $k = 2\pi f/U$, where f is the frequency and U is the turbulence velocity, or wind speed. The frequencies on the x-axis are multiplied by $2\pi/U$, while the power spectral densities of the measured inside and outside wind noise or turbulence on the y-axis are divided by $2\pi/U$. Since the measured wind noise data both inside and outside the fence are multiplied by the same constant, the difference between the two values remains unchanged, and hence the plotted reduction curves only change along the x-axis and remain the same along the y-axis.

3. Description and Data Analysis for the Measurement Series

A. Measurement Series 1: Varying Porosity

The first measurement series investigated the effects of varying the wall porosity of the wind fence on the pressure fluctuations at the center of the enclosure, the turbulence inside and behind the enclosure, and the velocity profile and gradient inside the enclosure. Porosity is defined as the percent ratio of the open surface area to the total surface area for one side of the fence. Five different porosities were tested, starting with all the vinyl privacy slats in place and then systematically removing them until only the chain link fencing and supporting metal framework remain. The porosities were approximately 30%—all slats in place, 40%—every fourth slat removed, 55%—every second and fourth slats removed, leaving the first and third slats in place, 65%—every second, third, and fourth slats removed, leaving the first slat in place, and 80%—all slats removed.

All five porosities were measured for each of the different measurement series and fence configurations, i.e. enclosing the open top with a roof, increasing the height or width, etc. This section will focus on the effects for the original wind fence design, described in Chapter III. In general, the effect of varying the porosity was similar for the different configurations. This section is divided into two parts with the first presenting and discussing the results of varying the porosity on the measured wind noise reductions. The second part presents and discusses the effect of varying the porosity on the measured mean wind velocity profile, the turbulence energy

reductions inside and behind the wind fence, and the implications of these with respect to wind noise reduction.

i. Effect on the measured wind noise spectra

The effect of varying the fence wall porosity on the wind noise spectra measured at the center of the wind fence enclosure is shown in Fig. 18. Examination of the data shows that reductions for the 30% porous fence (solid black lines) begin at k ≈ 1.0 m^{-1}, achieving 5 dB of reduction at about k ≈ 1.5 m^{-1}, and maximum reduction of about 10 dB at k ≈ 7-8 m^{-1}. Positive reductions for the 40% and 55% porous fences (green dashed and red dash-dotted lines, respectively) begin at a smaller wavenumber than the 30% fence, at k = 0.2-0.4 m^{-1}, and also achieve 5 dB of reduction at k ≈ 1.5 m^{-1}. Both the 40% and 55% fences reach a higher maximum reduction of 10-13 dB, but the reductions occur in the same wavenumber range as the 30% fence. Reductions for the 65% porous fence (blue dotted lines) also begin at k ≈ 1.0 m^{-1}, but increase much more gradually than the fences with 30%, 40%, and 55% porosities, achieving 5 dB of

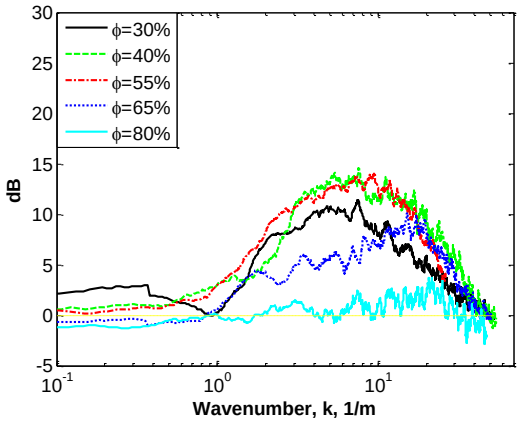

FIG. 18. Measured wind noise spectra reductions, in decibels, at different wall porosities across a fence with an open bottom gap and open top. The data was measured on 3/3/12.

reduction at $k \approx 7\ m^{-1}$, and a maximum of 8-9 dB at $k \approx 17\ m^{-1}$. The reductions for the 80% porous fence (solid light blue lines) only achieve a maximum of about 2 dB at $k \approx 20\ m^{-1}$.

In general, changing the fence porosity can significantly affect the noise reduction level for a given frequency band, and to a small extent the range of that frequency band. Best noise reductions are achieved at mid-level porosities (40% and 55%), followed by the 30% and 65% porosities. Wind fences with 80% wall porosities consistently achieved the lowest noise reductions, and in some cases even generated noise for wavenumbers near the audible frequency range. Noise reductions for the mid-level porosities typically begin between $k \approx 0.4$ and $1.0\ m^{-1}$, and exceed 5 dB of reduction over a wavenumber range between $k \approx 1.5\text{-}20\ m^{-1}$. Maximum reduction values were typically between 10-15 dB over a wavenumber range between $5\text{-}10\ m^{-1}$. Reduction levels for the two porosities were often the same; however, occasionally the 40% porosity performed better than the 55% and in other situations the 55% porosity achieved higher reduction levels. In those situations, the values differed by no more than 1-2 dB. Generally the fences with 30% wall porosity achieved maximum reduction levels for the same wavenumber range as the 40% and 55% porosities, but the levels are 1-5 dB less. The wavenumber range for fences with 65% wall porosities often matched the 30%, 40%, and 55% porosities, but just as often varied. The noise reduction levels for the 65% wall porosity were also about 1-3 dB less than the 30% porosity, but occasionally the two values matched.

The general trend that optimal noise reductions are achieved for the mid-level porosities and then perform worse as the porosities approach the extremes of being completely open or closed supports the theory that lower porosities will generate more shearing, while turbulence and wind velocity inside the fence increase for higher porosities. The data shows that the increase in wind noise in going from the 55% to the 65% wall porosity is greater than the

increase in going from 40% to 30% wall porosity, suggesting that the optimum porosity value is closer to 40% than to 55%.

ii. Effect on the meteorological variables

(a) The wind velocity profile

This section examines the effect of changing the fence wall porosity on the mean wind velocity profile, the respective velocity gradient, and the noise contribution from the turbulence-shear interaction inside the wind fence. The effect can be seen in Fig. 19, which shows the outside velocity profiles (black lines) and the respective profiles measured at the center of the wind fence for the five different wall porosities. All the profiles are plotted with the measured velocity on the x-axis and the heights of the six anemometer probes on the y-axis. As noted earlier the inside velocity profiles were measured for approximately 45 minutes, simultaneously with the measured wind noise. The outside velocity profiles are the average of the outside velocity profile measured for about 15 minutes before and after each 45 minute measurement run. The profile for the 80% porous fence should be approximately the same or less than the outside velocity profile, however it displays a higher wind speed at certain heights than the respective outside profile. This is due to the wind velocity both before and after the full 45 minute measurement being slightly lower than the wind velocity during the 45 minute measurement. The 80% velocity profile was also truncated with respect to height due to a faulty anemometer, which was later repaired.

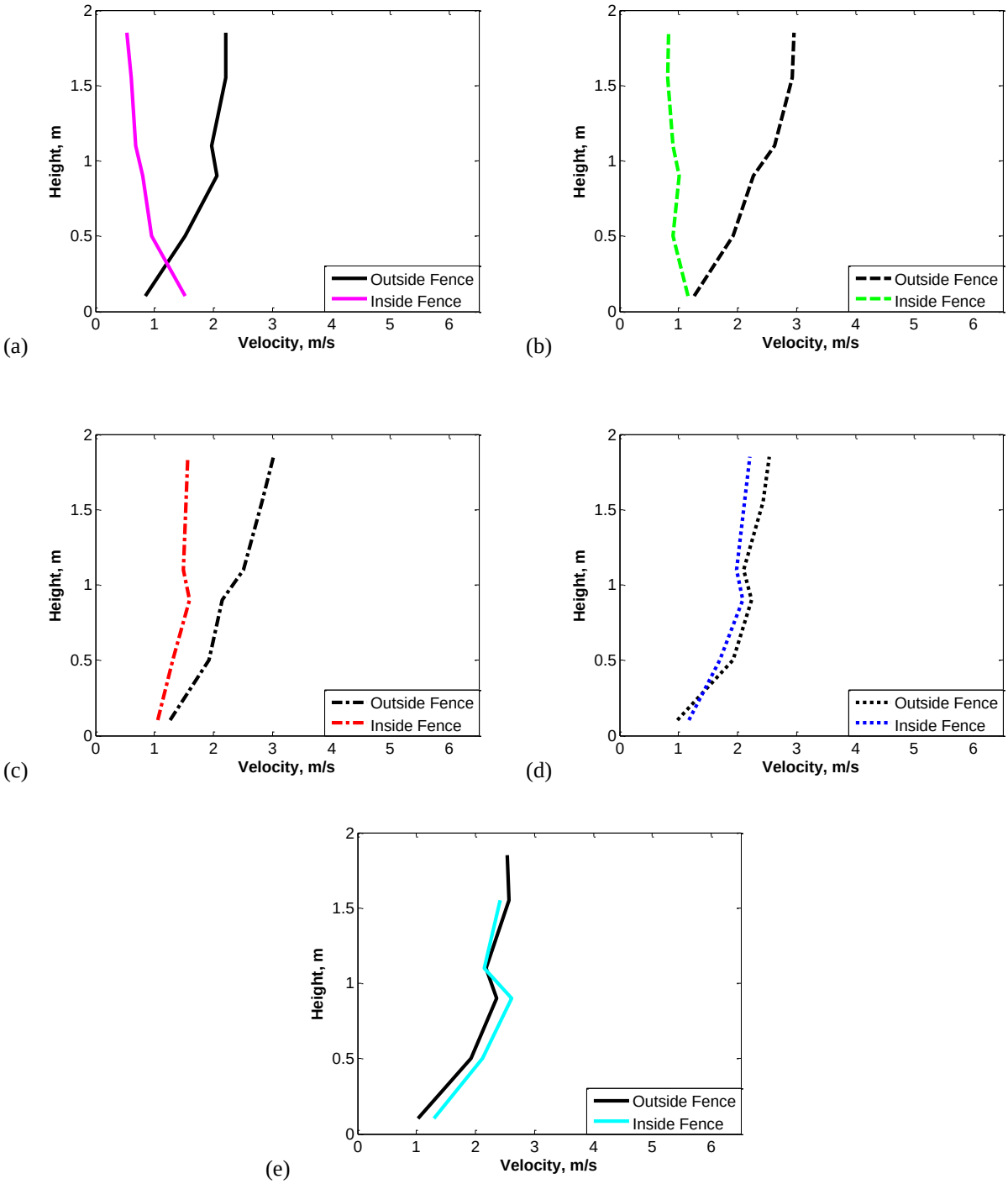

FIG. 19. Mean horizontal velocity wind profiles measured outside and inside a wind fence, set at (a) 30%, (b) 40%, (c) 55%, (d) 65%, and (e) 80% wall porosities, with an open top and open bottom gap. Data was measured on 3/3/12.

The wind speed at the base of the wind fence, z = 0.1 m, for all six velocity profiles are approximately 1.0-1.5 m/s. This is due to all the porosities sharing a common open flow space provided by the 0.1 m bottom gap. In general, as the wall porosity increases, the shape of the profile becomes more logarithmic and resembles that of the outside velocity profile. At low porosities, the maximum velocity occurs at or very near the ground and then decreases with height, with the minimum velocity occurring at or near the top of the wind fence enclosure. The shape of this profile resembles a slant or "reversed" logarithmic profile. As the wall porosity increases, the wind velocity near the top of the enclosure also increases, until it matches and then exceeds the velocity at the base of the wind fence. The extreme shapes of the "reversed slant" and logarithmic profiles that occur for the lowest and highest wall porosities (30% and 80%, respectively) result in the largest velocity gradients, while the shape of the velocity profiles measured inside the fence for the mid-level porosities are approximately straight vertical lines. Therefore the wind velocity inside the fence for middle porosities is nearly uniform with respect to height, which results in a very low velocity gradient.

(b) Measured turbulence spectra inside and behind the wind fence

This section will present and discuss how varying the wall porosity affects the horizontal and vertical components of the turbulence inside the wind fence and at three locations of increasing distance behind the wind fence. The three positions behind the fence are at x = 0.3 m, 2.9 m, and 5.8 m, or x/H = 0.1, 1.0, and 2.0; where H is the height of the wind fence and x is the distance behind the fence, relative to the back edge of the wall. The turbulence will be examined by determining the turbulence energy reductions relative to the turbulence incident to the fence.

If needed, changes to the turbulence isotropy will also be investigated. This section is divided into two parts. The first part focuses on the turbulence inside the fence and the second part focuses on the turbulence behind the fence.

(i) Effect on the turbulence inside the fence

The energy reductions for the horizontal and vertical components of the turbulence for each of the five wall porosities are shown in Fig. 20. The slopes for the horizontal turbulence reductions are negative, indicating that the high frequency turbulence is less attenuated by the wind fence than the low frequency turbulence. The slopes for the vertical turbulence reductions are mostly flat, and become positive at high frequencies. All the reduction values for both the vertical and horizontal components are positive and therefore the turbulence is generally reduced as it passes inside the wind fence. In general the largest reductions for both components of the turbulence occurs for the 40% and 55% porous fence, followed by the 30%, 60%, and 80%

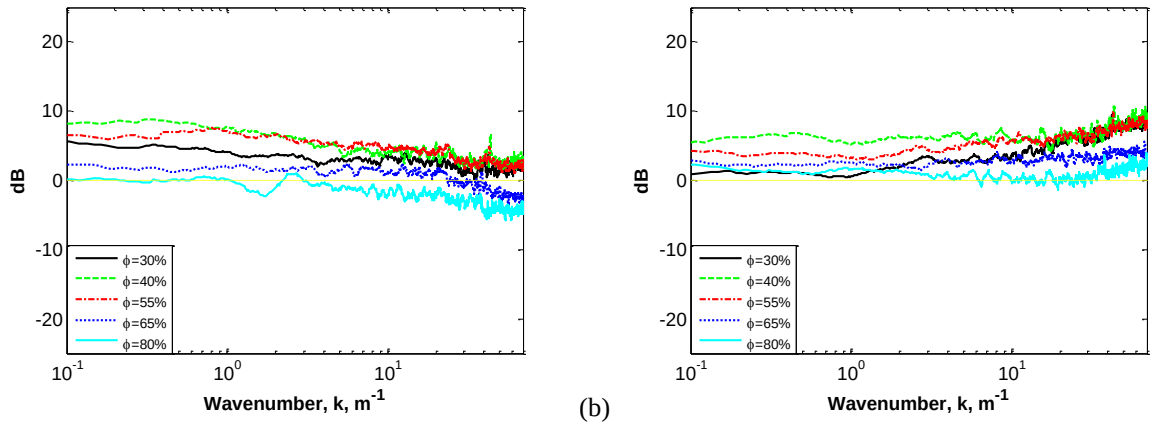

Fig. 20. Measured reductions of the (a) horizontal and (b) vertical components of the turbulence, in decibels, for different wall porosities, as the wind passes through the inside of a fence with an open top and open bottom gap. Data was measured on 3/3/12.

	Outside & Upwind, U_∞	Inside, U_{in}	U_∞ / U_{in}	$\Delta U = U_\infty - U_{in}$
30%	3.39	1.07	3.16	2.31
40%	3.27	1.26	2.6	2.01
55%	3.34	1.84	1.82	1.51
65%	3.5	2.48	1.41	1.02
80%	3.75	3.17	1.18	0.58

TABLE I. Mean wind velocities in m/s measured outside and upwind of the fence, U_∞, and inside at the center of the fence U_{in} for each porosity setting. The ratio of the outside to inside and the difference between the measured outside and inside velocities for each of the wall porosities are also shown. Data was measured on 03/03/12.

porous fences. This result is unexpected since the 30% fence is the most closed and has the highest wind speed reduction; see Tables I and II. The turbulence energy is minimized at mid-level porosities and then increases as the porosities approach the open and closed extremes. The increase in turbulence energy for the 30% porous fence may be due to a higher amount of re-circulating turbulence flow and cavity turbulence that occurs for lower porosity enclosures with open tops.

(ii) Effect on the turbulence behind the fence

Fig. 21 displays the effect of varying the wall porosity on the horizontal and vertical components of the turbulence behind the fence relative to the incident turbulence at the front of the fence. Two general trends can be identified. The first trend shows a general increase in the turbulence energy as porosity increases, with the levels matching the incident turbulence for the more open wall porosities. This is best seen in Fig. 21a, which shows the highest reduction levels for the more closed and mid-level porosities. The reduction levels then decrease in value

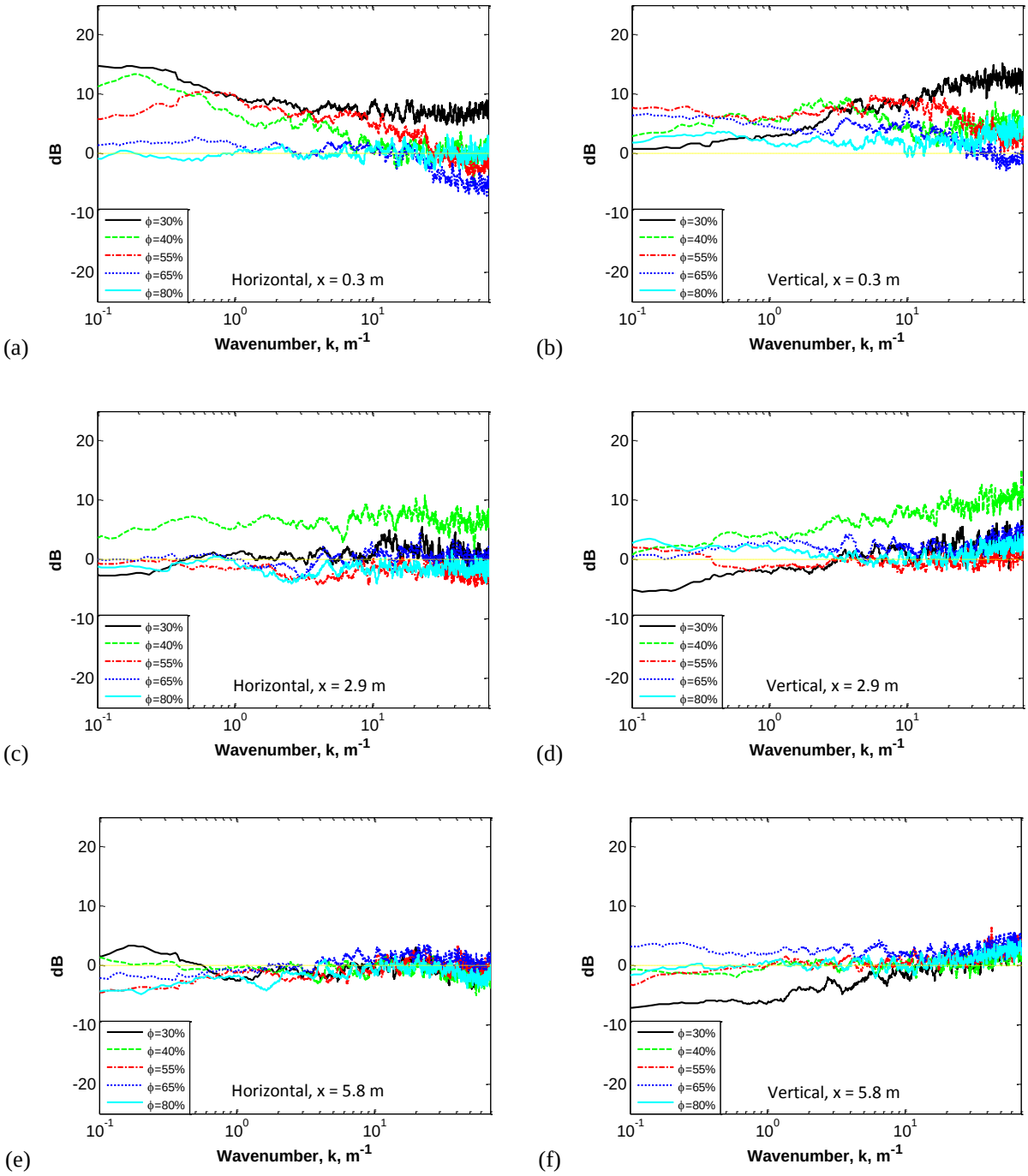

FIG. 21. Measured reductions of the horizontal and vertical components of the turbulence, in decibels, for different wall porosities, as the wind passes through and behind a fence at a distance of x/H = 0.3, x/H = 1.0, and x/H = 2.0. Data was measured on 3/3/12 for a fence with an open top and open bottom gap.

with increasing porosity until there is little difference between the turbulence on the leeward side of the fence and the turbulence upwind and incident to the wind fence.

The second trend is that turbulence energy is at a minimum immediately behind the fence, but then increases with distance from the fence, eventually approaching the energy level of the incident turbulence in front of the fence. This trend can be seen by comparing Figs. 21a-b, which shows the changes immediately behind the fence at approximately x = 0.3 m, to Figs. 21c-d and 21e-f, which show the changes at x = 2.9 m and 5.8 m behind the fence, respectively. This trend also suggests the formation of a turbulent shadow zone immediately behind the fence for low and mid-level porosities. The ±1 dB reduction level for the 30% and 55% porous fences and the 6 dB level for the 40% at x = 2.9 m indicates that the zone's length is dependent on the porosity, with the maximum length occurring for mid-level porosities. This is also shown in the minimization of the wind speed for the 40% fence at x = 0.3 and 2.9 m; see Table II. The 0 dB reduction level for both the 65% and 80% porous fences indicates that the flow does not separate or form a shadow zone for more open porosities. However, the reduced wind velocities at distances up to x = 2.9 m shows some sheltering effects.

	Outside & Upwind, U_∞	Inside, U_{in}	Behind, x/H=0.1, U_a	Behind, x/H=1.0, U_b	Behind, x/H=2.0, U_c
30%	3.39	1.07	0.55	1.32	1.57
40%	3.27	1.26	0.69	0.72	2.27
55%	3.34	1.84	1.44	2.2	2.56
65%	3.5	2.48	2.66	2.09	3.56
80%	3.75	3.17	2.19	2.06	3.98

TABLE II. Mean wind velocities in m/s measured outside and upwind of the fence, U_∞, inside at the center of the fence, U_{in}, at x = 0.29 m behind the fence, U_a, x = 2.9 m behind the fence, U_b, and at x = 5.8 m behind the fence, U_c, for each porosity setting. Data was measured on 03/03/12.

Generally, the data demonstrates that the horizontal and vertical turbulence is lower or equal to the incident turbulence for all the measurement positions. However, Fig 21d and e, display an enhancement of the vertical turbulence at low frequencies for distances of x = 2.9 m, and 5.8 m behind a 30% porous wind fence. An examination of the measured turbulence spectra, Fig. 22, shows that the shape of the vertical spectra does not change; hence the increase in turbulence is not due to any narrow band excitation which might generate significant wind noise. The enhancement is due to a general and gradual increase in the turbulence energy level, suggesting a vertical turbulence shadow zone behind the fence and the generation of turbulence

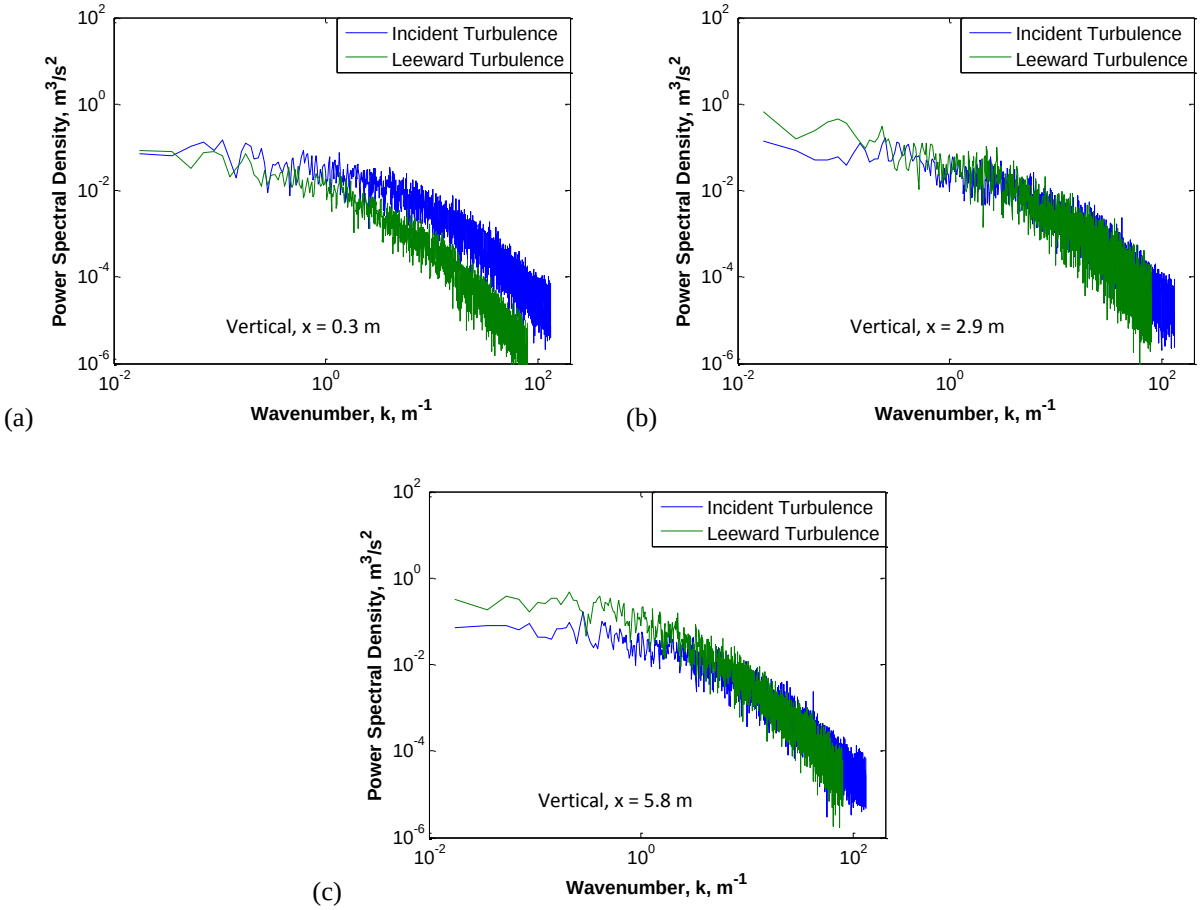

FIG. 22. Vertical turbulence spectra measured in front of and behind a 30% porous wind fence at distances of (a) x/H = 0.3, (b) x/H = 1.0 m, and (c) x/H = 2.0 m. Data was measured on 3/3/12.

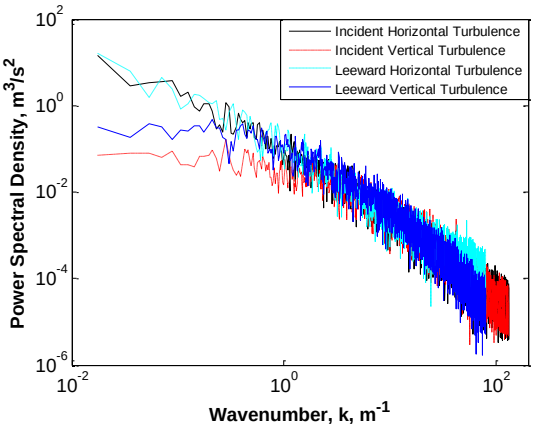

FIG 23. Horizontal and vertical components of the turbulence spectra measured in front of and behind the 30% porous fence at a distance of x = 5.8 m, or x/H = 2.0. Data was measured on 3/3/12.

outside of this zone. Vertical turbulence at these frequencies is still suppressed and lower than the horizontal turbulence, as displayed in Fig. 23. Any significant noise contribution due to low frequency vertical turbulence in the wake is therefore unlikely to occur.

iii. Discussion and Conclusions

Mid-level porosities are best for infrasonic noise reduction. The measured wind noise was consistently the lowest at these porosities. The velocity gradients for these porosities are minimal, due to a near uniform velocity profile inside the wind fence. This results in a minimization of any shearing effects inside the fence. Both the horizontal and vertical components of the turbulence are also small for mid-level porosities. The combined minimization of the shearing and turbulence results in a minimization of the noise contribution due to the turbulence-shear interaction. The turbulence behind the fence is also minimized and

contributes very little to the measured wind noise. Finally, there was no observed vortex shedding for the mid-level porosities.

Noise reductions are very low for very porous wind fences. The velocity gradient and measured turbulence inside a very porous wind fence are large. Hence, the resulting noise contribution due to the turbulence-shear interaction and the turbulence-turbulence interaction are at a maximum. Noise reductions are also poor for a low porosity wind fence. However, the reductions are better than that for very open porosities. The velocity gradient inside a less permeable fence is very large; however, the turbulence is at a minimum. The resulting noise contribution of the turbulence-shear interaction is higher than the mid-level porosities, but less than the very open porosities. The turbulence immediately behind a closed fence is also at a minimum. However, low frequency turbulence is generated in the wake of a closed fence at distances approximately equal to the wind fence height and greater. The noise contribution from this enhancement is small since the low frequency vertical turbulence enhancement is small and occurs far behind the fence. The enhancement is also not likely due to any vortex shedding since it is broad banded. Vortex shedding is highly oscillatory at a particular frequency and therefore has a narrow frequency band. In summary, the mid-level porosities are the ideal for optimizing wind noise reduction, where the best porosity is probably between 45-50%.

B. Measurement Series 2: Modifying the Bottom Gap and Open Top Treatments

The second measurement series examined the changes in the measured wind noise by the addition of a porous roof to the open top of the wind fence and the elimination of its bottom gap by extending the privacy slats to the ground. The series also investigated the effects of these treatments on the turbulence inside and behind the fence, the velocity profile and gradient inside the fence, and how they relate to changes in the wind noise. The series is divided into two investigations. The first investigation will determine if turbulence and wind noise are affected by the elimination of the bottom gap. Park and Lee[71] showed that turbulence is reduced in the leeward side of a two dimensional wind barrier when there is a small bottom gap. A similar effect should occur for a wind fence enclosure. The bottom gap was closed by inserting extension slats into the bottom gap; see Fig. 24. The number of extension slats matched the number of wall slats, and were removed in the same systematic pattern. Generally, a fence with

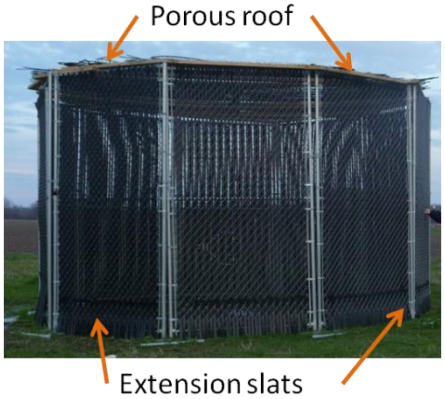

FIG. 24. The wind enclosure at 30% porosity; the top and bottom gap are closed with a porous roof and extension slats.

a bottom gap will be referred to as an "open bottom gap" fence, while a fence without a bottom gap will be referred to as a "closed bottom gap" fence.

The second investigation will determine if adding a porous roof will enhance turbulence and wind noise reductions inside the wind barrier enclosure. A reduction is expected since Christie[53, 74-76] and Hedlin and Raspet[7] showed improved signal to noise ratios when a roof covering was added to their wind fences. The porous roof, like the walls, was made of 8 gauge 2 inch chain link fence with vinyl privacy slats inserted into the fencing. The slats could be added or removed to adjust the roof's porosity. Due to the physical differences in its construction, the roof porosities were slightly different from that of the walls. In order to maintain a uniform porosity over the entire surface of the wind fence the roof slats were removed in a different pattern, matching the wall porosity as closely as possible. The porosities for the roof were approximately 35%--all slats in place; 45%--every third slat removed, leaving the first and second slats in place; 60%--every second and third slat removed, leaving only the first slat in place; and 70%--all the slats were removed, with only the chain link fence and supporting framework remaining. The 35% porous roof was used with both the 30% and 40% porous walls. The 45%, 60%, and 70% porous roofs were matched with the 55%, 65%, and 80% porous walls, respectively. Three different types of roof or top treatments were tested in this investigation. The first type was for a fence without a roof covering. It will be referred to as an "open top" fence. The second treatment was the addition of a 70% porous roof. A fence with this treatment is called a "semi-open top" fence. The third and final treatment is called a "closed top" fence. This refers to a fence with either a 35% or 45% porous roof covering, which were used with the 40% and 55% wall porosities, respectively.

The data presented in this measurement series will only be the data measured at the two mid-level porosities, 40% and 55%, since these two porosities consistently achieved the highest noise reductions. The presentation and discussion of the results and data for this measurement series will be divided into three parts. The first will focus on the changes to the wind noise reductions. The second will present the effects on the measured mean wind velocity profile, the turbulence measured inside the fence, and the turbulence measured behind the wind fence. The third part will discuss the results, implications, and how the turbulence and velocity conditions relate to the wind noise.

i. Effect on the measured wind noise spectra

(a) Bottom gap treatment

This section will first examine how the wind noise measured at the center of the wind fence is affected by the presence or lack of a small gap located at the base of the wind fence panels. The bottom gap is approximately 0.1 m and the gap to height ratio, g/H, is 0.03. This value falls within the recommended value of g/H = 0.125 determined by Park and Lee to minimize turbulence behind a porous shelter.[71] The differences in noise reductions for an open and closed bottom gap fence are shown in Figs. 25-27. Specifically, Fig. 25 displays the change in noise reductions when the bottom gap of the original open top fence is closed off for both the 40% and 55% wall porosities. Similarly, Figs. 26 and 27 show the changes in noise reductions when the bottom gap for a 40% and 55% porous wind fence with a semi-open top treatment and a closed top treatment, respectively, is eliminated with extension slats. These results show that the reductions of the bottom gap treatment are independent of the condition of the roof.

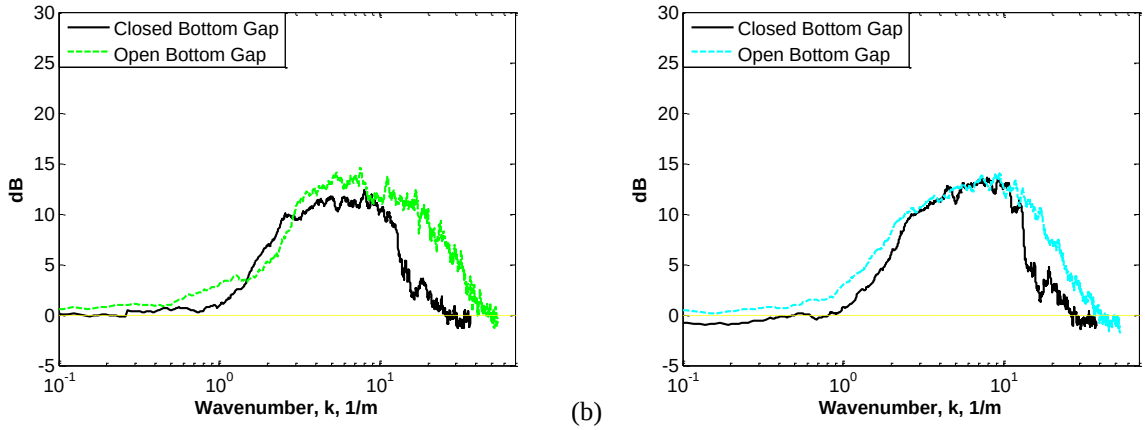

FIG. 25. Effects of the bottom gap treatment on the measured noise reduction at the center of an open top fence at (a) 40% and (b) 55% porosities. Data was measured on 2/24/12 and 3/3/12.

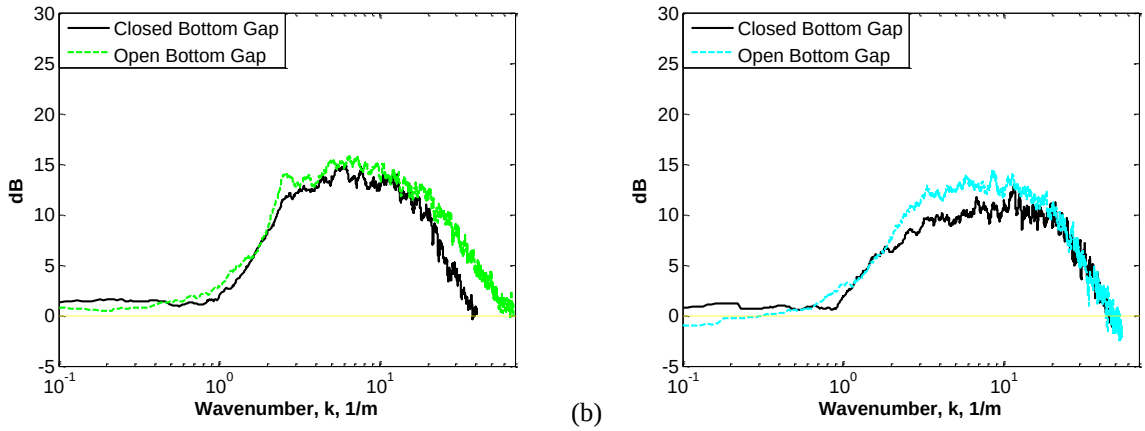

FIG. 26. Effects of the bottom gap treatment on the measured noise reduction at the center of a semi-open top fence at (a) 40% and (b) 55% porosities. Data was measured on 4/11/12 and 4/14/12.

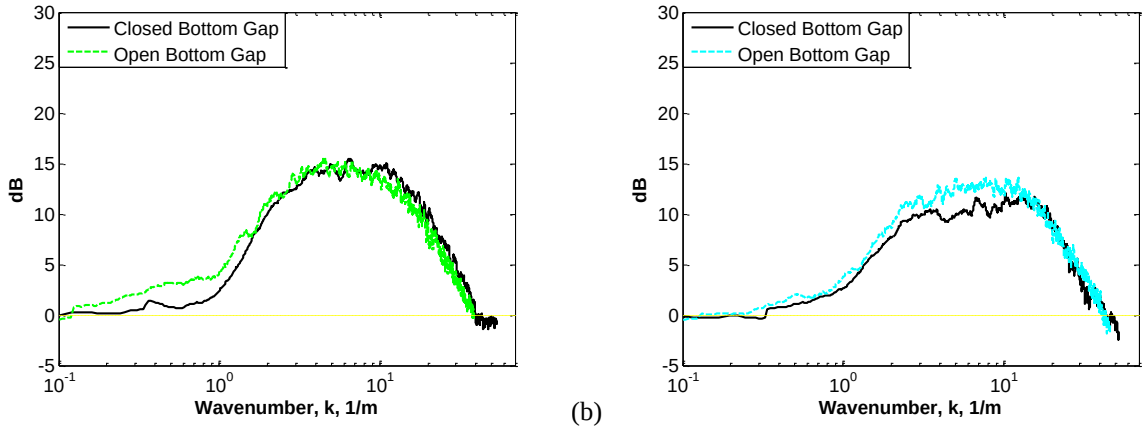

FIG. 27. Effects of the bottom gap treatment on the measured noise reduction at the center of a closed top fence at (a) 40% and (b) 55% porosities. Data was measured on 4/6/12 and 4/25/12.

Generally the reductions for a fence with an open bottom gap are either comparable to or better than the reductions for a fence with a closed bottom gap, with an improvement of 1-2 dB at most wavenumbers. The maximum reduction values for the bottom gap fences are generally about 14-15 dB, whereas the maximum reduction values for the fences with a closed bottom gap are generally between 10-13 dB, with some at 14 dB. The wavenumber range over which the maximum reductions occur is also larger for an open bottom gap fence than for a fence with a closed bottom gap. This is especially true for the open top case shown in Fig. 25. The open bottom gap fences achieve 10 dB of reduction or better between approximately k = 1.5-30 m^{-1}, while the closed bottom gap is approximately from k = 2-20 m^{-1}. The data clearly shows that having a small bottom gap is beneficial to reducing wind noise inside a porous wind fence.

(b) Top treatments

This section will discuss how the wind noise measured at the center of the wind fence is affected by the addition of a porous roof. Previous investigations[7, 53, 74-76] showed that the addition of a porous roof improves noise reductions. The results are displayed in Figs. 28 and 29 which show the differences in the noise reductions for the open top, semi-open top, and closed top treatments. The black lines in each of the plots represent the fences with an open top, the red line represents the fences with a semi-open top, and the green and blue lines represent the fences with a closed top at 40% and 55% wall porosity, respectively.

The data for the 40% porous fences, Figs. 28a and 29a, shows a consistent pattern that adding a porous roof improves noise reductions at all frequencies, regardless of the roof porosity or the bottom gap condition. The noise reductions for both the closed and semi-open top fences

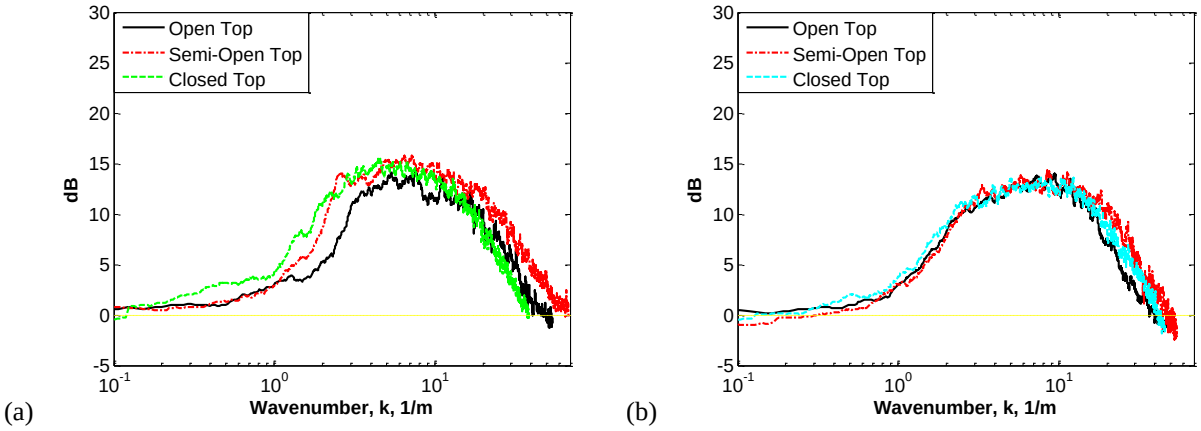

FIG. 28. Effects of modifying the top treatment on the measured noise reduction at the center of an open bottom gap fence at (a) 40% and (b) 55% porosities. Data was measured on 3/3/12, 4/14/12, and 4/25/12.

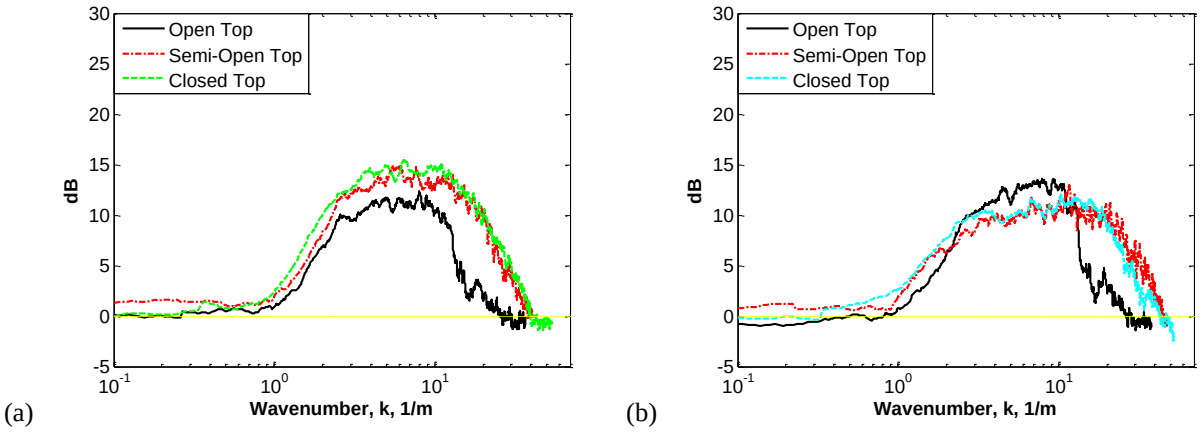

FIG. 29. Effects of modifying the top treatment on the measured noise reduction at the center of a closed bottom gap fence at (a) 40% and (b) 55% porosities. Data was measured on 2/24/12, 4/11/12, and 4/6/12.

are nearly identical, peaking at approximately 14-15 dB, which is approximately 1-3 dB higher than the open top fence. Likewise, the wavenumber range for the semi-open top and closed top fences are also nearly the same and larger than the open top fence, achieving 10 dB of reduction or better between k = 2-25 m^{-1}. However, this pattern is not seen for the 55% porous fences, Figs. 28b and 29b. Instead, the data shows that noise reductions are unaffected by the addition of a porous roof if the bottom gap is open, and become worse if the bottom gap is closed. If the

reduction pattern for the 55% porous fences was similar to or the same as the pattern for the 40% porous fence then it would suggest that having a porous roof would be beneficial for improving wind noise reductions. As it is, due to the inconsistent pattern for the 55% porous fences, we cannot reach a definitive conclusion that any particular treatment to the top of the fence is beneficial to improving wind noise reductions.

ii. Effect on the meteorological variables

(a) The wind velocity profile for the bottom gap and top treatments

Modifying the bottom gap affects the wind velocity profile, the velocity gradient, and the shearing at the center of the wind fence enclosure. This section will demonstrate how the velocity profiles change as the bottom gap is modified. The results are displayed in Figs. 30 and 31, which show the inside and outside velocity profiles for a 40% and 55% porous fence with (a) an open and (b) a closed bottom gap. The black lines in each plot represent the velocity profile outside and upwind of the fence, while the green and light blue lines represent the velocity profiles inside the 40% and 55% porous fences, respectively.

The results show that the wind velocity at the base of an open bottom gap fence is unhindered and is comparable to the wind velocity outside the fence. The wind velocity gradient and the noise generated by the turbulence-shear interaction are therefore small. Conversely, closing off the bottom gap hinders the wind flow near the ground, which makes the flow less uniform with respect to height. The shape of the velocity profile inside a 55% porous is approximately logarithmic. However, closing off the bottom gap increases the slope. Likewise eliminating the bottom gap causes the profile for the 40% fence to change from a reversed slant

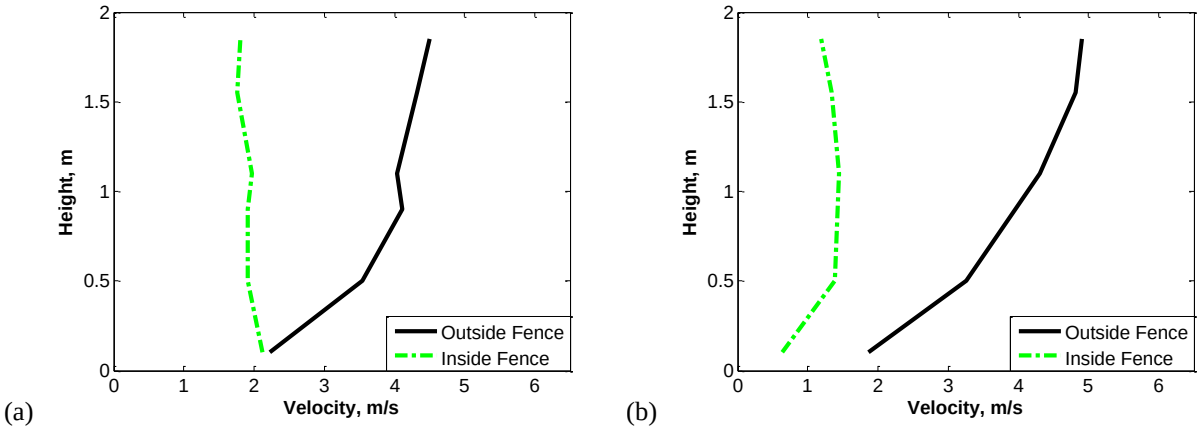

FIG. 30. Measured wind velocity profiles inside and outside of a 40% porous wind fence with (a) an open bottom gap, and (b) a closed bottom gap. Data was measured on 5/1/12 and 2/17/11.

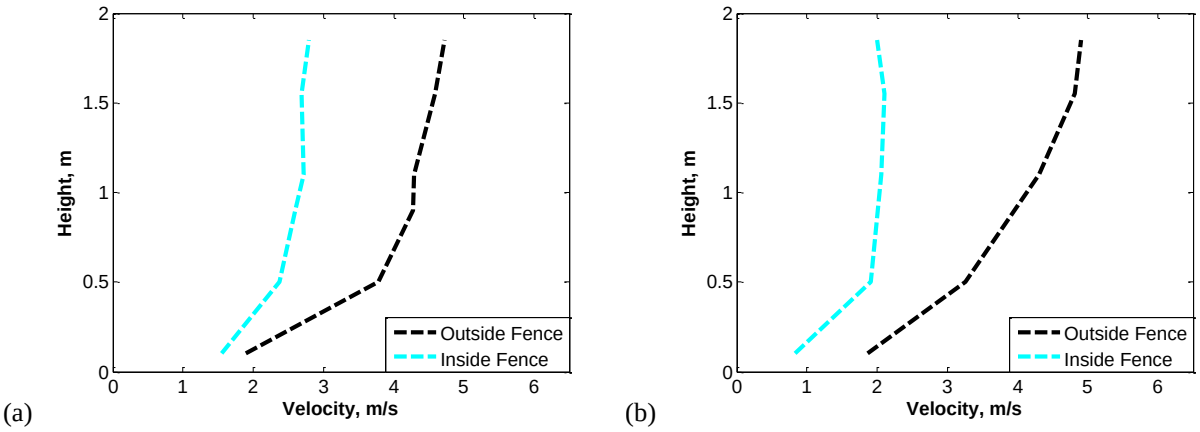

FIG. 31 Measured wind velocity profiles inside and outside of a 55% porous wind fence with (a) an open bottom gap, and (b) a closed bottom gap. Data was measured on 5/1/12 and 2/17/11.

to a bowed or arced shape, with the apex of the arc located approximately at z = 0.5 m. This occurs due to the combination of the slower velocities at the base of the fence and near the top of the fence.

Unlike the bottom gap, modification of the fence's top treatment has little to no effect on the velocity profile inside the fence. This can be seen in Fig. 32 which shows the outside and inside velocity profiles for a fence with an open top, a semi-open top, and a closed roof

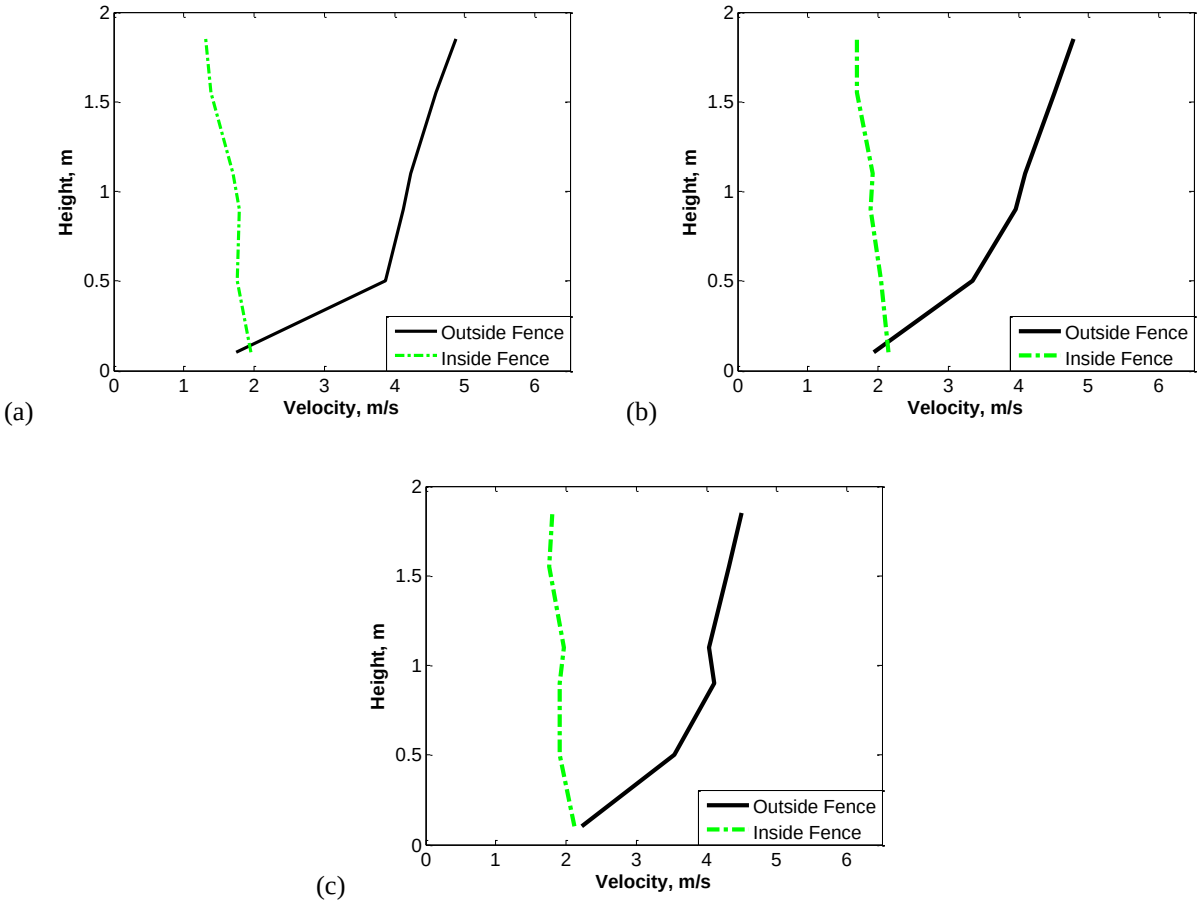

FIG. 32. Measured wind velocity profile for a 40% porous wind fence with an open bottom gap, and (a) an open top, (b) a semi-open top, and (c) a closed top. Data was measured on 3/6/12, 4/23/12, and 5/1/12.

treatment. Initial comparisons would indicate a slight difference between the open top fence and the two fences covered by the porous roof, due to differing wind velocities at the base and top of the profile. However, closer examination shows that the slopes for the three profiles are approximately the same, indicating that there are no significant changes to the velocity profile when the top treatment is modified. Therefore, the velocity gradient and turbulence-shear interactions at the center of the wind fence are unaffected by the addition or lack of a porous roof.

(b) Measured turbulence spectra inside the wind fence enclosure

This section will examine how modifying the bottom gap and roof treatments affects the horizontal and vertical components of the measured turbulence inside the wind fence. As with the porosity investigation, changes in the turbulence due to modifying the bottom gap and roof treatments help indicate the mechanisms that result in better noise reductions. The purpose of this part of the investigation is to determine how the turbulence is modified inside the wind fence enclosure. As before, the turbulence is examined by determining the turbulence energy reductions relative to the turbulence incident to the fence.

(i) Bottom gap treatments

The investigation by Park and Lee[71] showed that turbulence behind a two dimensional porous wind barrier with a small bottom gap was lower than the turbulence behind a similar wind barrier without a bottom gap. A similar effect should also occur for a wind fence enclosure; hence the turbulence reductions for an open bottom gap fence should be better than the reductions for a fence without a bottom gap. Only the results for the 40% porous fence will be presented in this section, since the reductions for both the 40% and 55% are comparable. The results can be seen in Fig. 33, which displays the reductions for (a) the horizontal and (b) the vertical components of the turbulence for a closed and open bottom gap fence. The black lines for both of the plots represent the reductions for a closed bottom gap fence and the green lines represent the reductions for an open bottom gap fence. The results show that the reductions for both the open and closed bottom gap fences are comparable at most wavenumbers. The shapes

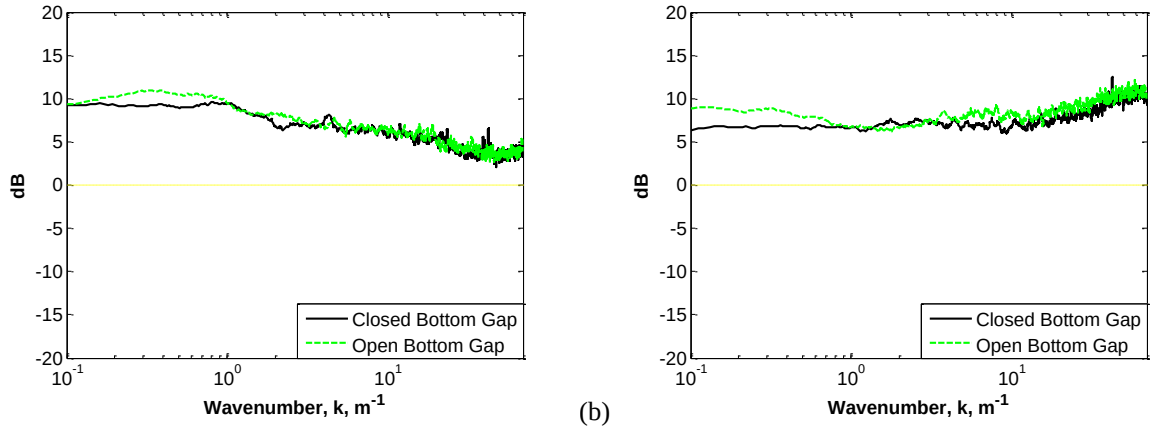

FIG. 33. The measured energy spectra reductions of (a) the horizontal and (b) the vertical components of the turbulence, in decibels, inside of a closed and open bottom gap fence. The closed bottom gap data was measured on 4/11/12 and the open bottom gap data was measured on 4/14/12.

and magnitudes of the reduction levels are approximately the same. This demonstrates that turbulence inside the fence is relatively unaffected by the presence or lack of a bottom gap.

(ii) Top treatments

The effect of the open, semi-open, and closed top treatments on the horizontal and vertical energy reductions for the 40% and 55% porous fences are displayed in Figs. 34 and 35, respectively. The 55% data is included since the investigation of the wind noise spectra was inconclusive, and an examination of the turbulence spectra may provide better insight as to whether the addition of a porous roof will improve wind noise reductions. The results indicate that the addition of a porous roof improves the reduction of the horizontal component of the turbulence for a 40% porous fence, while the reductions for 55% porous fence remain approximately the same. The vertical component of the turbulence is also mostly unaffected by

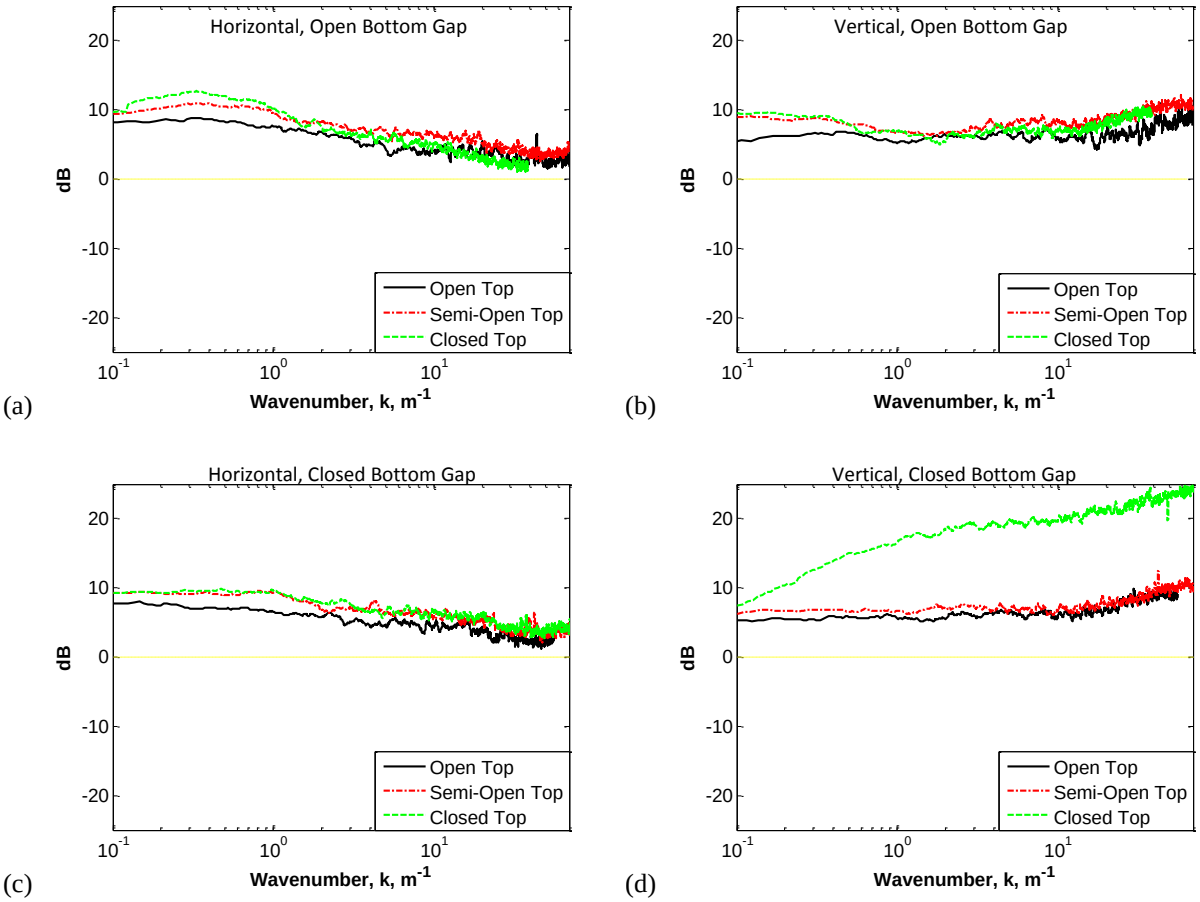

FIG. 34. Measured energy spectra reductions of the horizontal and vertical components of the turbulence, in decibels, inside of an open bottom gap fence and a closed bottom gap fence with 40% wall porosity, as the top treatment was modified. Data for the open bottom gap fence was measured on 3/3/12, 4/14//12, 4/25/12. Data for the closed bottom gap fence was measured on 2/24/12, 4/11/12, and 4/6/12.

the addition of a 70% porous roof. However, the results demonstrate that the vertical turbulence reductions improve by the addition of a less porous roof. The magnitude of this improvement varies, where some measurements showed little to no change (Figs. 34b and 35b), while others achieved significant gains (see Figs. 34d and 35d). The cause of the large variations in the reductions is unknown. However, it is unrelated to the condition of the bottom gap and the porosity. In conclusion, the turbulence is reduced when a porous roof is added. The magnitude of this improvement is variable and inconsistent.

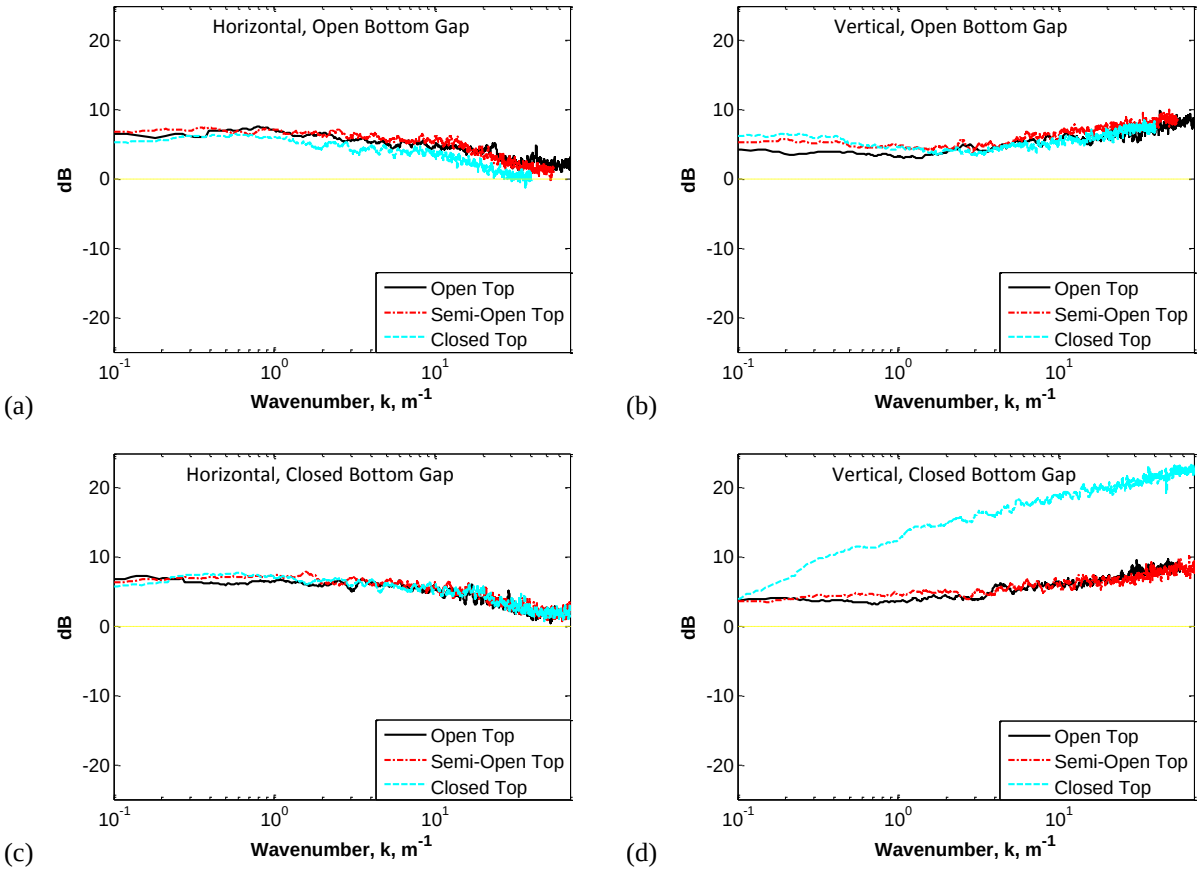

FIG. 35. Measured energy spectra reductions of the horizontal and vertical components of the turbulence, in decibels, inside of an open bottom gap fence and a closed bottom gap fence with 55% wall porosity, as the top treatment was modified. Data for the open bottom gap fence was measured on 3/3/12, 4/14//12, 4/25/12. Data for the closed bottom gap fence was measured on 2/24/12, 4/11/12, and 4/6/12.

(c) Effect on the turbulence behind the fence

This section will determine how eliminating the fence's bottom gap and open top affects the horizontal and vertical components of the measured turbulence at three positions of increasing distance behind the fence. The three positions are the same positions that were examined for the porosity investigation, x = 0.3 m, 2.9 m, and 5.8 m or x/H = 0.1, 1.0, and 2.0. Due to the large amount of data obtained for this section, and that the data for both the 40% and

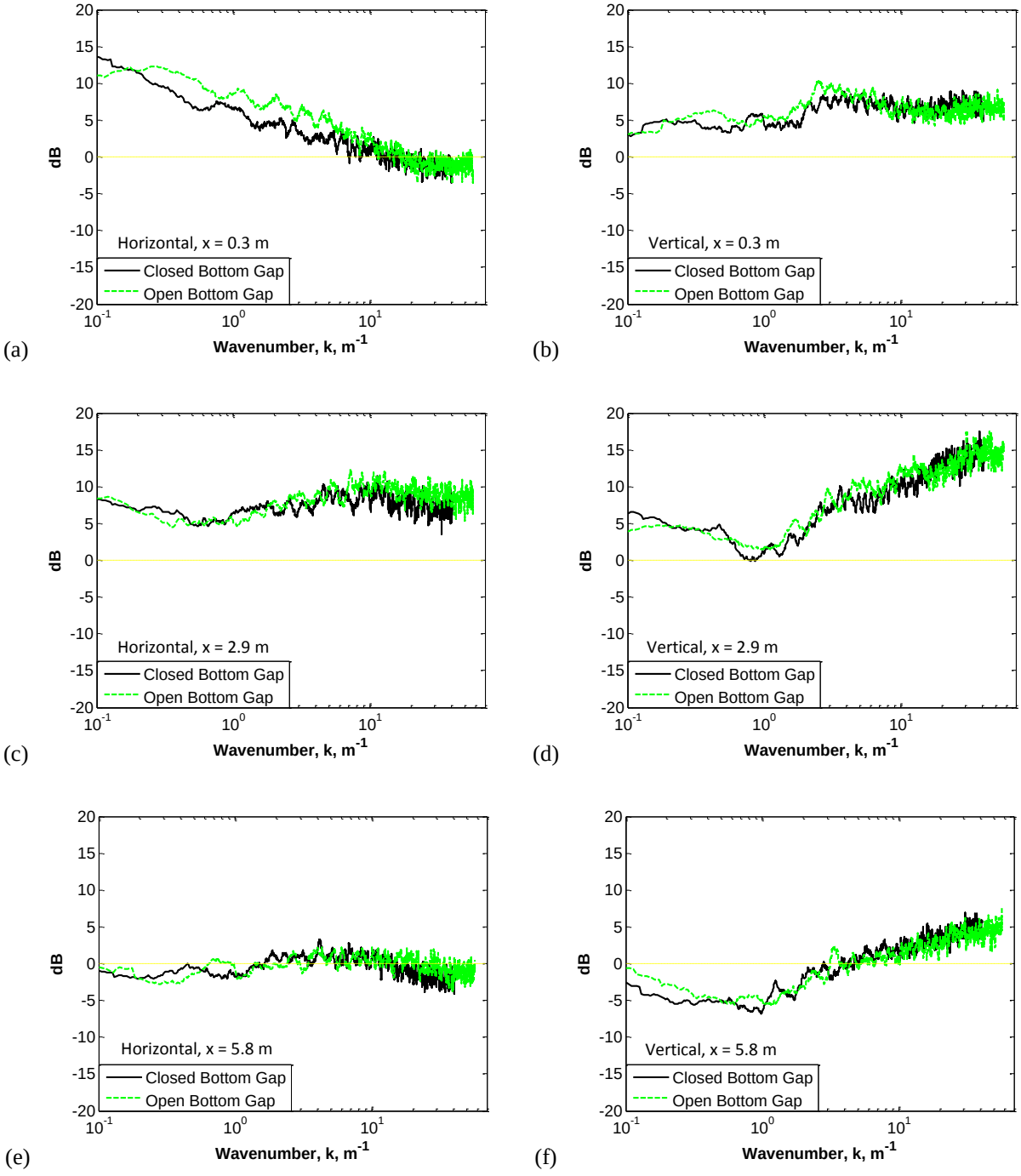

FIG. 36. Comparisons of the measured energy spectra reductions of the horizontal and vertical components of the turbulence, in decibels, behind a closed and open bottom gap fence with 40% wall porosity at a distance of x/H = 0.1, x/H = 1.0, and x/H = 2.0. The closed bottom gap data was measured on 3/7/12 and the open bottom gap data was measured on 3/6/12.

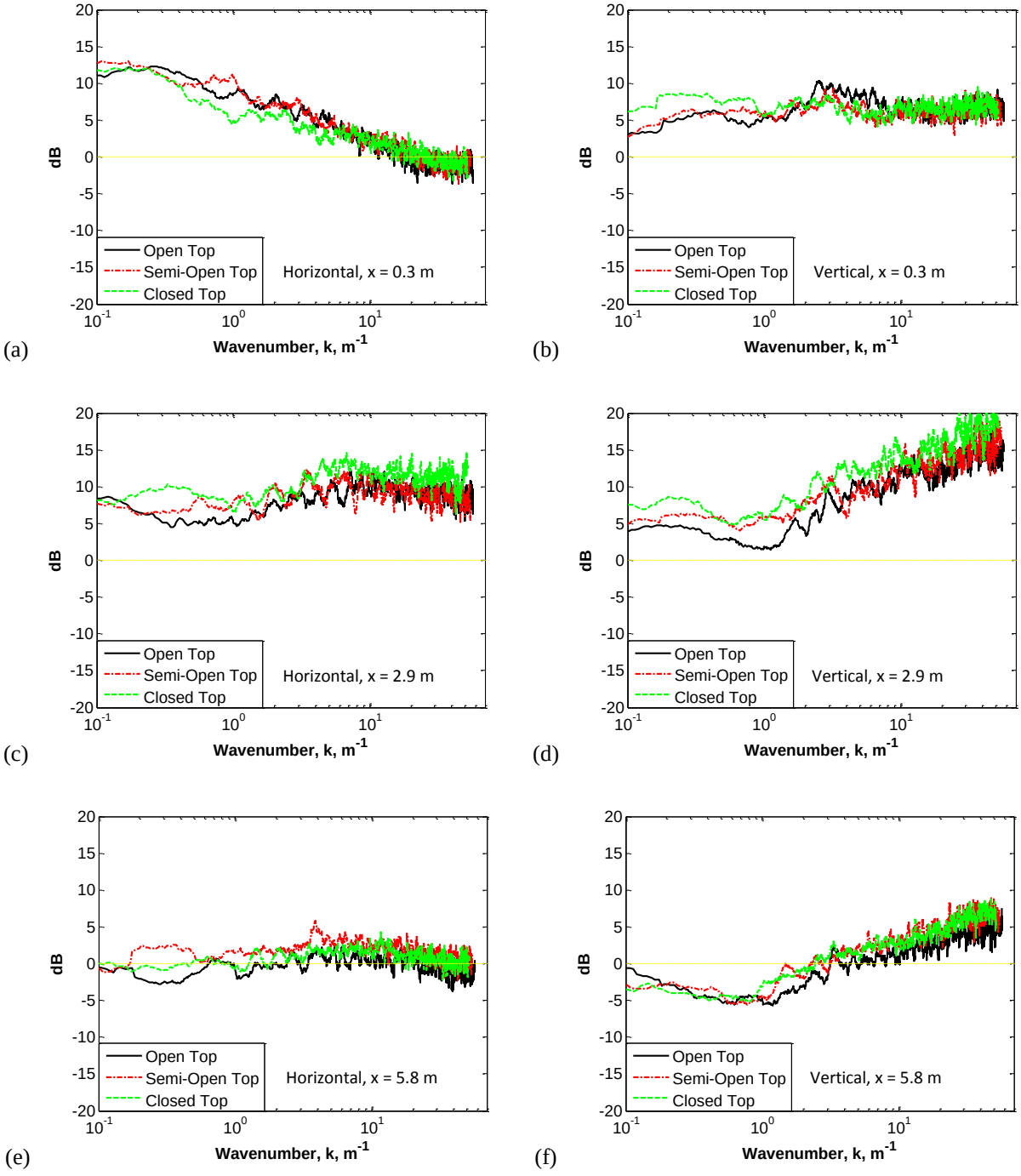

FIG. 37. Measured energy spectra reductions of the horizontal and vertical components of the turbulence, in decibels, behind an open bottom gap fence with 40% wall porosity, as the top treatment was modified, at a distance of x/H = 0.1, x/H = 1.0, and x/H = 2.0. The open top data was measured on 3/6/12, the semi-open top data on 4/23/12, and the closed top data on 5/1/12.

55% porous fences are comparable, only the results for the fences with 40% wall porosity will be presented in this section.

Results of the bottom gap treatment are shown in Fig. 36, and the results for the roof treatments are shown in Fig. 37. Both sets show the reductions for a 40% porous fence. The 55% porous fence is not shown, since the reduction patterns are comparable. The results show that the magnitude of the all the horizontal turbulence reductions decreases with distance from the fence until, at x = 5.8 m, the leeward side turbulence is the same as the incident turbulence at the front of the fence. Likewise the magnitude of the vertical turbulence reductions decreases with distance. However, instead of matching the incident vertical turbulence, low frequency turbulence is generated. As seen in Fig. 38, the magnitude of the generated vertical turbulence is lower than the horizontal turbulence. It is therefore not significant. In general, the results show that there is little to no difference in the turbulence at any point behind the fence regardless of the bottom gap treatment or roof treatment. Therefore neither the bottom gap nor the roof has any significant affect on the turbulence behind the fence.

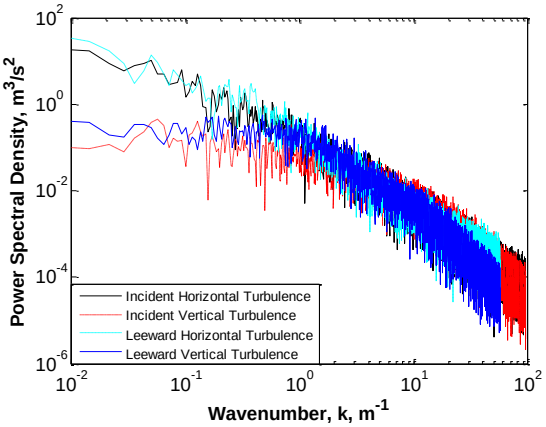

FIG 38. Horizontal and vertical components of the turbulence spectra measured in front of and behind an open top and open bottom gap fence at a distance of x = 5.8 m, or x/H = 2.0. Data was measured on 3/6/12.

iii. Discussion and Conclusions

The second measurement series investigated the effect of adding a porous roof to the fence's open top and eliminating its bottom gap to the wind noise, turbulence, and velocity profile measured at its center, and the turbulence measured behind the enclosure. The investigation showed that a small bottom gap is beneficial to improving wind noise reductions, where the measured wind noise was slightly lower for an open bottom gap fence. The flow at the base of the fence was unhindered, resulting in a more uniform flow velocity with respect to height. This resulted in a minimization of the velocity gradient and shearing effects. Surprisingly, the turbulence inside the enclosure was unaffected by modifications to the bottom gap. This was contrary to the results found by Park and Lee.[71] Even though the turbulence was unaffected, the minimization of the velocity gradient and shearing by the bottom gap results in a lower contribution of the turbulence-shear interaction inside the enclosure. The wake turbulence did not change due to any modifications to the bottom gap. Therefore any noise contributions from the wake turbulence were unaffected.

The second part of the measurement series investigated if adding a porous roof to the wind fence is beneficial to wind noise reduction. Previous investigations[7, 53, 76-78] showed that the addition of a porous roof improves noise reductions. However, the results for this investigation showed that the effects of adding a porous roof on the measured wind noise were small and inconsistent. The reductions only showed consistent improvement for a 40% porous fence. This indicates that adding a porous roof may be beneficial, but only for wind fences with lower wall porosities. The small and inconsistent effect on the wind noise may be due to the relative height of the fence. Due to its height the separation distance between the top and base of the fence is

sufficient so that any modifications to the wind noise due to the addition of a porous roof are negligible at the sensor.

The addition of a porous roof did not affect the velocity profile or the wake turbulence, and minimally affected the horizontal component of the turbulence inside the fence. The vertical turbulence reductions improved; however the magnitudes of these improvements were varied and inconsistent. Therefore any noise reduction that does occur due to the addition of a porous roof is caused by the limiting of the vertical component of the turbulence, as it passes over the top of the fence. However, this effect is small.

In summary, it is favorable to have a small gap at the base of the fence; however the improvement is small. Turbulence inside the fence is reduced by adding a porous roof which suggests that adding the roof is beneficial to wind noise reductions. However, the benefit of adding a porous roof is not conclusive, since the improvements to the wind noise were small and inconsistent.

C. Measurement Series 3: Size and Scaling Laws

The third measurement series investigated how changing the wind fence enclosure's relative size affects the wind noise reduction, turbulence, and the wind velocity profile at its center, as well as the wake turbulence behind the fence. The first objective of the investigation was to see if low frequency noise reductions will improve as the size of the fence increases, and if the improvement is in proportion to the increase in size. The second objective of the investigation was to verify if a large, cylindrically shaped, porous wind fence is subject to scaling laws; and if so, to identify its characteristic dimensions. If the wind fence enclosure in this investigation is subject to scaling laws then the measured noise reductions should shift to lower wavenumbers in proportion to the respective enlarged height and width (see page 12, Strasberg[29-30], and Hedlin and Raspet[7]). The investigations consisted of constructing and testing a wind fence enclosure with a height that was two times that of the original wind barrier (5.8 m), and then constructing and testing another wind fence enclosure with a diameter twice that of the original wind barrier (10.0 m); see Fig. 39. Ideally, a wind fence enclosure with both the height and width doubled relative to the original wind barrier should have been constructed and tested. However, due to constraints, such an investigation was not practical. Such an investigation does have merit and should be considered for future research. Further, due to size limitations, the top of the fences were left open for this measurement series. The bottom gaps were modified during the series. However, the results for these modifications will not be presented since they either did not significantly differ or provide any new or additional insights.

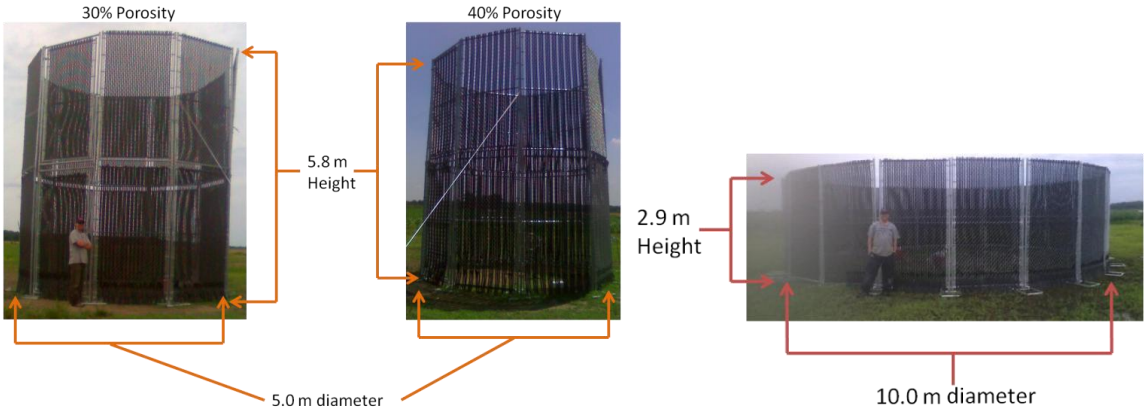

FIG. 39. Dimensions of the double height (right) and double width (left) wind fence enclosures. The two double height fences have 30% and 40% wall porosity, and the double width fence has 30% wall porosity.

It is important to consider if there is a limiting value for the wind fence diameter, and if doubling its width exceeds this limiting value. Flow theory suggests that the pressure sensor should be placed within the turbulent shadow zone that forms behind the front wall of the wind fence. If the radius of the enclosure were to exceed this distance then the sheltering conditions of the fence may become ineffective. Fortunately, the expanded radius for the 10 m wind fence does fall within the turbulent shadow zone, as determined by the leeside turbulence measurements performed for the porosity investigation; see page 63.

The results presented and discussed in this section will be the data measured at the 40% wall porosity since this porosity, along with the 55% wall porosity, consistently achieved the highest noise reductions. The data for the 55% wall porosity will not be presented, since generally it is comparable to the 40% porosity. However, it will also be presented if there are significant differences between the data for the two porosities, such as differing trends and behaviors, or if further information and insight can be gained from the additional information. As a matter of simplifying nomenclature and ease of identification, the three different sized fences in this investigation will be referred to as “standard” or “single” for the original 2.9 m

high and 5.0 m diameter wind fence, “double height” for the 5.8 m high and 5.0 m diameter wind fence, and “double width” for the 2.9 m high and 10.0 m diameter wind fence.

The first section will present and discuss the effect on the wind noise reductions as measured at the center of the wind fence relative to the wind noise measured outside and upwind of the fence. The second section will discuss the effect on the wind velocity profile measured inside the fence. This section will also discuss the effect on the turbulence energy reductions both inside and behind the fence relative to the turbulence upwind and incident to the fence. The third section will summarize and discuss the overall effects, trends, and behaviors identified in the previous two sections. The sections presenting the wind noise and meteorological measurements will be further subdivided into two different parts focusing on the effects for the two investigated dimensions; first, doubling the height, and second, doubling the width.

i. Effect on the measured wind noise spectra

(a) Double Height

The dimension investigated in the first part of the study was the windscreen’s height, h. This first section describes the change in noise reductions measured inside the wind fence when the height is doubled from approximately 2.9 m to 5.8 m. The effect can be seen in Fig. 40, which shows the wind noise reductions for a double height fence relative to a single height fence with (a) 40% and (b) 55% wall porosities. As can be seen, the results are not completely consistent, but there are some general trends. At 55% wall porosity, increasing the wind fence’s height does not improve the maximum noise reduction level; it stays at approximately 14 dB. It

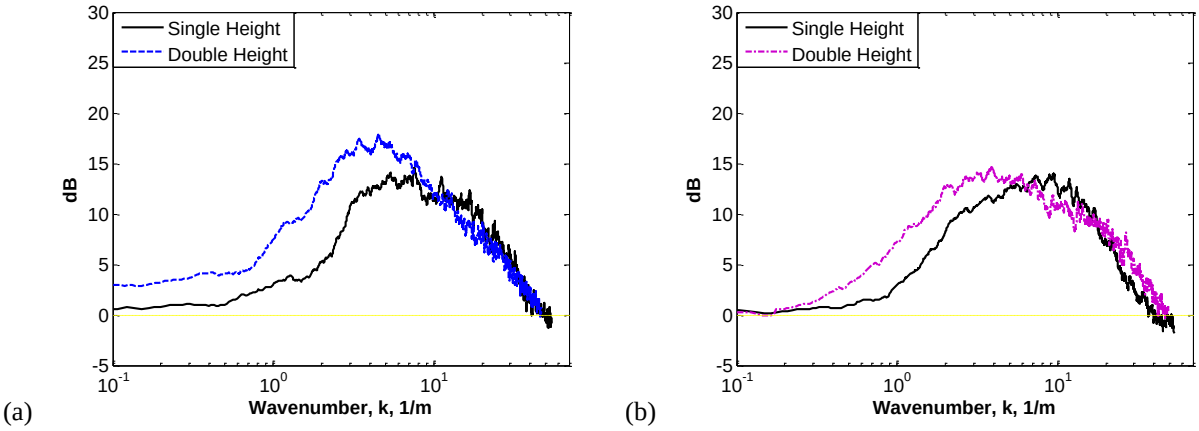

FIG. 40. Measured noise reductions, in decibels, comparing a double height fence to a single height fence, at (a) 40% and (b) 55% wall porosities, with an open bottom gap. Data was measured on 5/28/13 and 3/3/12.

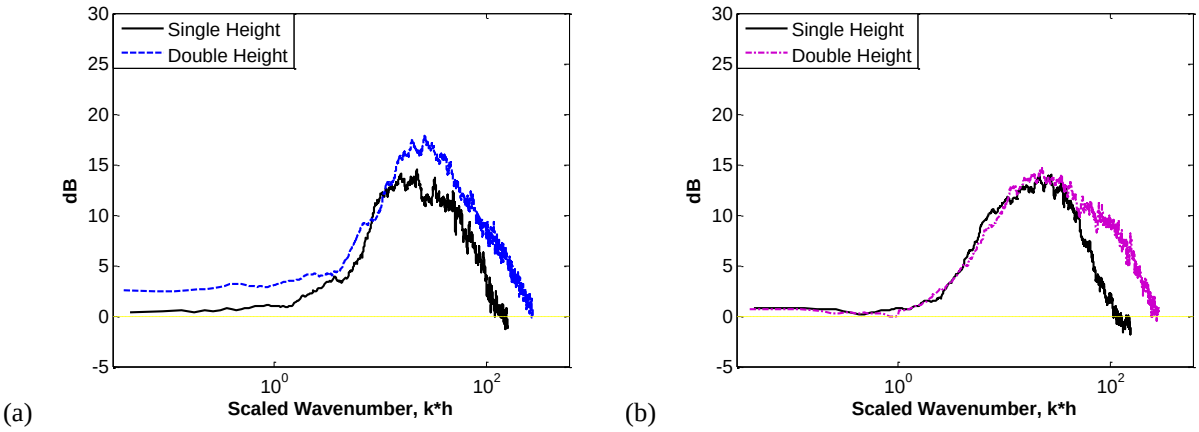

FIG. 41. Measured noise reductions, in decibels, versus wavenumber scaled with height, comparing a double width fence to a single width fence, at (a) 40% and (b) 55% wall porosities, with an open bottom gap. Data was measured on 5/28/13 and 3/3/12.

does, however, cause the reductions to shift to a lower wavenumber band by approximately a factor of two; with the peaks of the reduction curves at k = 3.5 m^{-1} and k = 7.5 m^{-1} for the double and single height fences, respectively. The shift improves reductions for wavenumbers between k = 0.4 m^{-1} and 2.0 m^{-1} by approximately 3-6 dB. The results for 40% wall porosity differ slightly from the 55% wall porosity. At 40%, increasing the wind fence's height improves both the maximum noise reduction level and shifts the reductions to a lower wavenumber band. The

maximum reduction levels improve by about 4 dB, while the shift to the lower wavenumber band is also by about a factor of two, with the peak of the reduction curve shifting from $k = 8\ m^{-1}$ to $k = 4\ m^{-1}$.

The scaled reduction curves of the double and single height fences at (a) 40% and (b) 55% wall porosity are displayed in Fig. 41. The plots are scaled by multiplying the wavenumber, k, by the height, h. The results show that the scaled plots do not align perfectly since the reduction bandwidth for the double height fence is wider than the single height fence. This misalignment and imperfect scaling suggests that the height alone is not a characteristic dimension. Therefore low wavenumber noise reductions will not improve in proportion to the height of the wind fence. However, the shift does suggest that low frequency wind noise reductions will improve as the enclosure's height is increased. The shift suggests that the improved reductions are due to the taller wind fence modifying more of the turbulence-shear interaction in the free stream, since the source location for this interaction at low frequencies is at higher levels in the atmosphere. The improved reductions are also due to an increased area averaging since the surface area increased. In general, increasing the height of the wind fence is advantageous to improving wind noise reductions.

(b) Double Width

The second dimension investigated in this measurement series is the fence's diameter, d, which will also be referred to as width. This section describes the change in noise reductions measured inside the wind fence when the diameter is doubled from approximately 5.0 m to 10.0

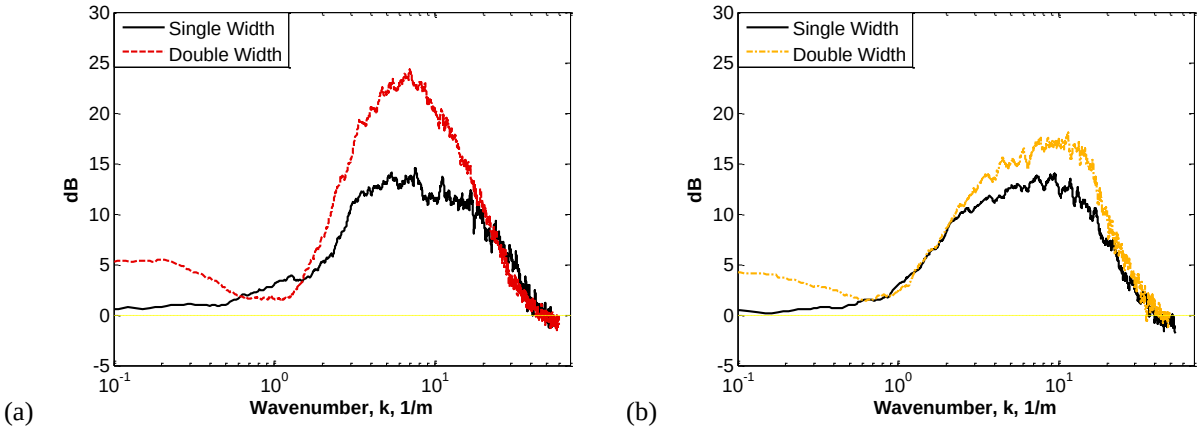

FIG. 42. Measured noise reductions, in decibels, comparing a double width fence to a single width fence, at (a) 40% and (b) 55% wall porosities, with an open bottom gap. Data was measured on 4/17/13 and 3/3/12.

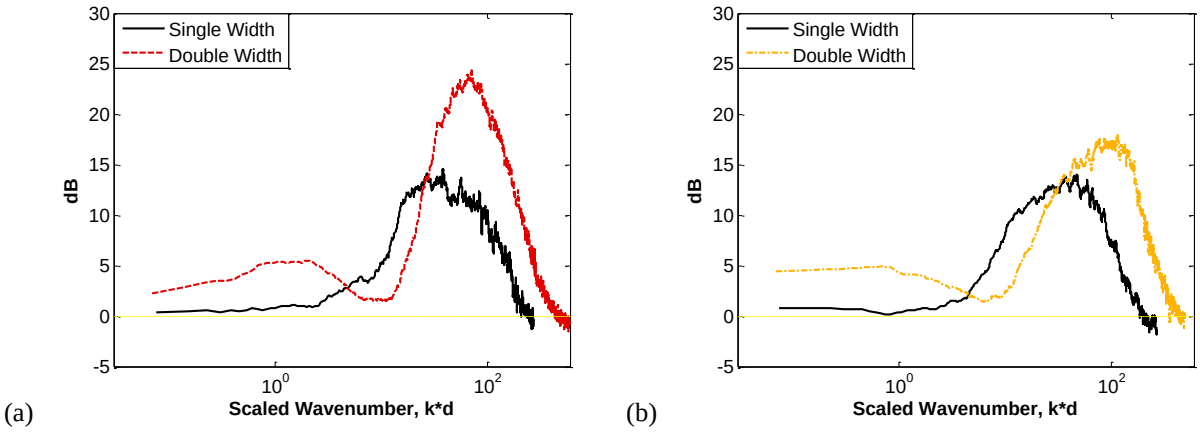

FIG. 43. Measured noise reductions, in decibels, versus wavenumber scaled with width, comparing a double width fence to a single width fence, at (a) 40% and (b) 55% wall porosities, with an open bottom gap. Data was measured on 4/17/13 and 3/3/12.

m. The effect can be seen in Fig. 42, which shows the wind noise reductions for a double width wind fence relative to a single width wind fence with (a) 40% and (b) 55% wall porosities. The reductions curves for the single width fences shown in Fig. 42 are the same as the reductions curves for the single height fences shown in Fig. 40. The results for doubling the width differ slightly for the 40% and 55% porosities, but there are some commonalities. In general, the data indicates that expanding the diameter of the wind fence enclosure significantly improves noise

reductions. The maximum noise reduction level increases by 10 dB for the 40% porous fence and by 5 dB for the 55% porous fence. However, unlike increasing the height of the fence, the noise reductions are not shifted to lower wavenumbers. The peaks of the reduction curves for both the 40% and 55% porous fences stay at k = 7-8 m^{-1}.

The scaled reduction curves of the double and single width fences at (a) 40% and (b) 55% wall porosity are shown in Fig. 43. The plots are scaled by multiplying the wavenumber, k, by the diameter, d. The results show that the scaled reduction curves do not align. This shows that the diameter alone is not a characteristic dimension of the wind fence. The improvements in the reductions are due to the increase in the separation distance between the pressure sensor and the effects of the stagnation pressure and turbulence-shear interactions at the surface of the wind fence, and by the increased averaging area of the surface. In general, the results show that increasing the diameter of the wind fence is beneficial to wind noise reduction. Overall, increasing the size of the wind fence improves noise reductions. Expanding the width leads to large reductions in the same frequency band, while increasing the height leads to better noise reductions at lower frequencies and an expanded frequency bandwidth.

ii. Effect on the meteorological variables

(a) The wind velocity profile

This section will discuss how the velocity profile measured at the center of the wind fence changes as its height and then its diameter are doubled. The purpose of this investigation is to identify modifications to the velocity gradient and shearing as the wind fence is enlarged.

These modifications along with modifications to the turbulence will be used to determine the noise contributions of the turbulence-shear interaction inside the fence, and contributions from any other noise sources.

(i) Double Height

The effect of increasing the height of the wind fence on the velocity profile is displayed in Figs. 44 and 45. The two figures show the velocity profiles measured at the center of (a) a single and (b) a double height wind fence at 40% and 55% wall porosities. As can be seen, the shapes of the velocity profiles remain approximately the same for both the single and double height wind fences. The reverse slant shape characteristic of the 40% open bottom gap fence is retained with approximately the same slope. Likewise the logarithmic shapes and slopes for the 55% porous fence are retained. The results suggest that increasing the fence's height does not affect the wind velocity profile and gradient. This is expected since any changes to the profile

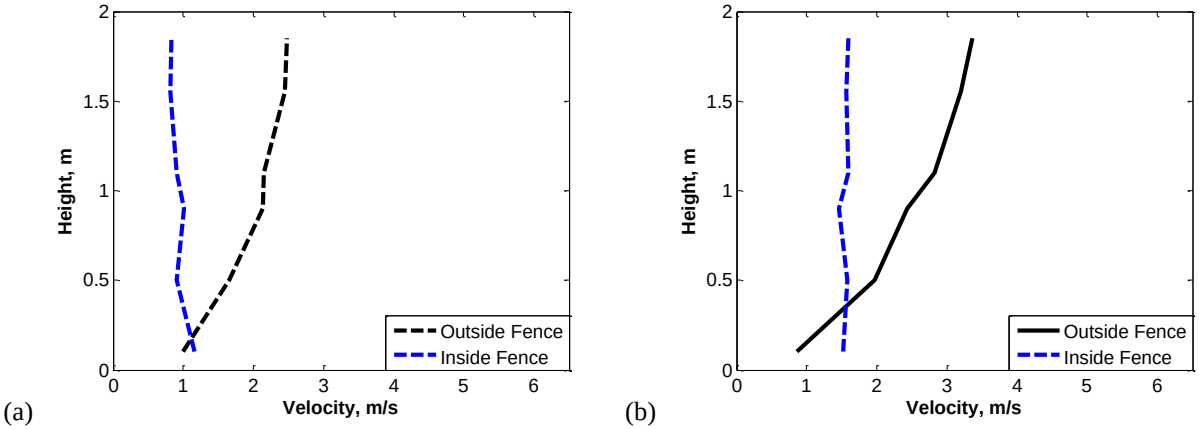

FIG. 44. Measured wind velocity profiles inside and outside of (a) a single height and (b) a double height wind fence with an open bottom gap and at 40% wall porosity. Data was measured on 3/3/12 and 5/28/13.

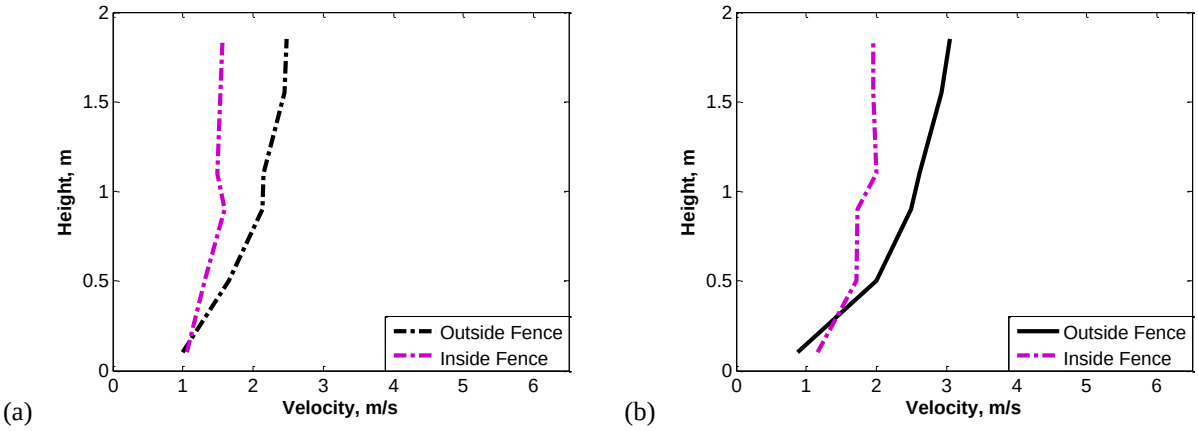

FIG. 45. Measured wind velocity profiles inside and outside of (a) a single height and (b) a double height wind fence with an open bottom gap and at 55% wall porosity. Data was measured on 3/3/12 and 5/28/13.

that may occur will likely occur near the top of the fence, which is beyond the height measured by the 2 m anemometer array. This is also where the velocity profile transitions to the logarithmic shape associated with a free flow field.

(ii) Double Width

The effects of doubling the wind fence diameter on the velocity profile are shown in Figs. 46 and 47. The two figures display the velocity profiles measured at the center of (a) a single and (b) a double width wind fence and at 40% and 55% wall porosities, respectively. The data shows that the shapes and slopes of the velocity profiles are not conserved when the diameter is doubled. Rather, doubling the width has a similar effect to closing off the bottom gap for a single width fence: the velocities at the base of the profile are significantly slowed down and the velocities near the top of the profile are unaffected. This causes the reverse slant shape for the 40% porous fence with open bottom gap to change to the bowed or arced shape where the wind

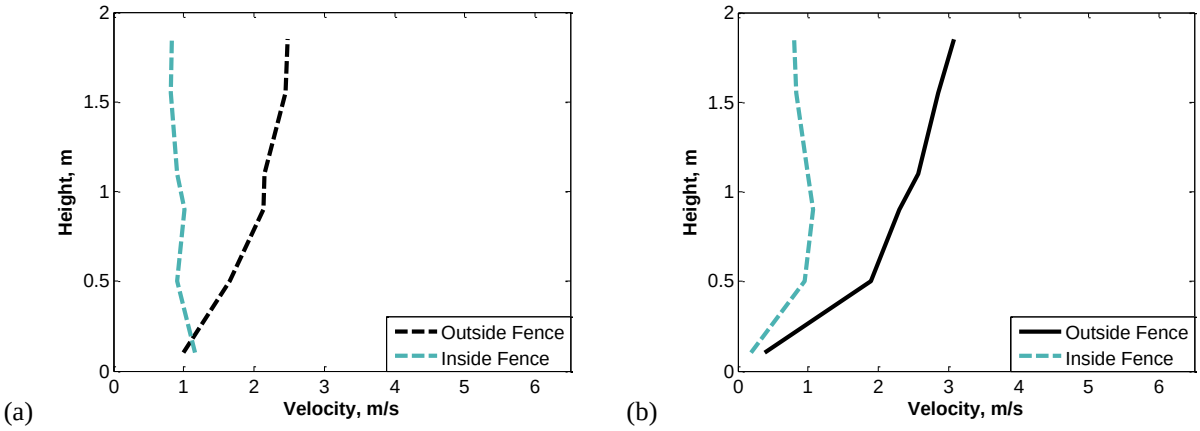

FIG. 46. Measured wind velocity profiles inside and outside of (a) a single width and (b) a double width wind fence with an open bottom gap and at 40% wall porosity. Data was measured on 3/6/12 and 4/17/13.

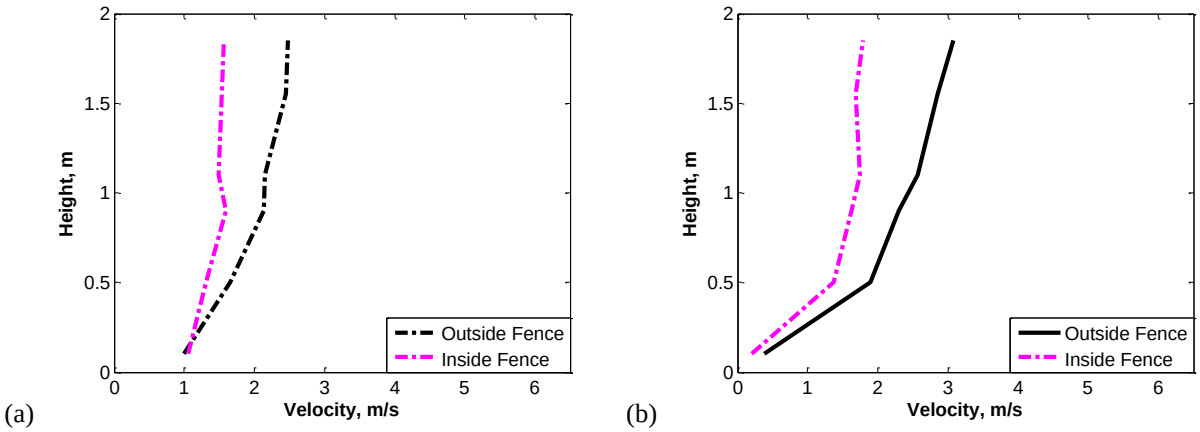

FIG. 47. Measured wind velocity profiles inside and outside of (a) a single width and (b) a double width wind fence with an open bottom gap and at 55% wall porosity. Data was measured on 3/6/12 and 4/17/13.

velocity at the top and bottom of the profile are slower than the velocity at a height of approximately 1.0 m. The effect also causes logarithmically shaped velocity profiles, like that of the 55% porous fence, to have an increased slope. Expanding the diameter of the wind fence enclosure, therefore, causes an increase in the velocity gradient and shearing. This may be due to the increased diameter allowing sufficient time and distance for the modifications to the velocity profile caused by passing through and over the barrier's surface to dissipate.

(b) The measured turbulence spectra inside the wind fence

This section discusses how reductions of the horizontal and vertical components of the turbulence energy spectra inside the fence relative to the turbulence upwind and incident to the fence change as the fence's height and then its diameter are doubled. The effects of increasing the wind fence enclosure height are displayed in Fig. 48, which shows the reduction curves of the (a) horizontal and (b) vertical components of the turbulence for a single height and double height wind fence at 40% wall porosity. The data shows significant improvement to the turbulence energy reductions for the horizontal component of the turbulence. The vertical turbulence was also reduced. However the magnitude of this reduction was small. Regardless, improved turbulence reductions were consistently observed, with varying degrees of magnitude, for increasing the wind fence height.

The results of doubling the wind fence height on the horizontal and vertical components of the turbulence are displayed in Fig. 49. The data indicates that the reductions for the double

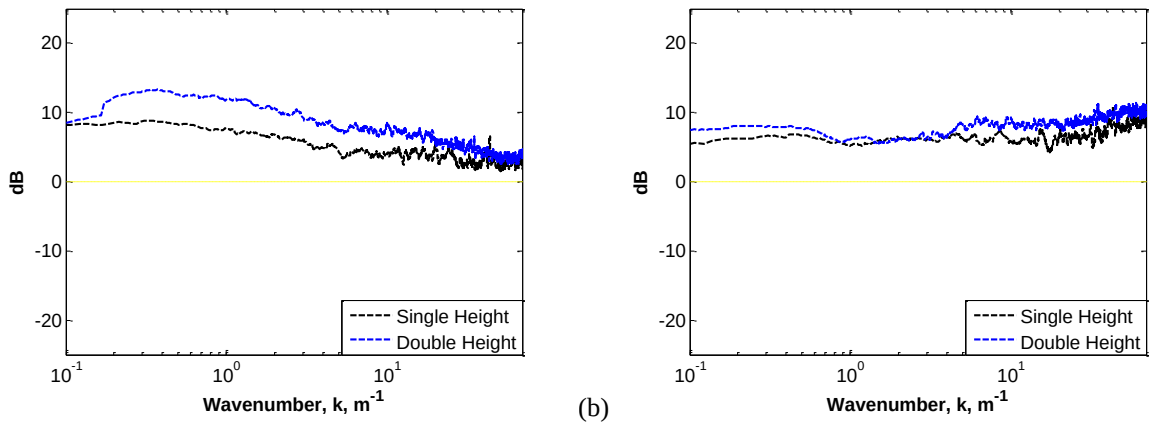

FIG. 48. Comparison of the measured energy spectra reductions of the (a) horizontal and (b) vertical components of the turbulence, in decibels, inside of a single and a double height wind fence with an open bottom gap and at 40% wall porosity. Data was measured on 3/3/12 and 5/28/13.

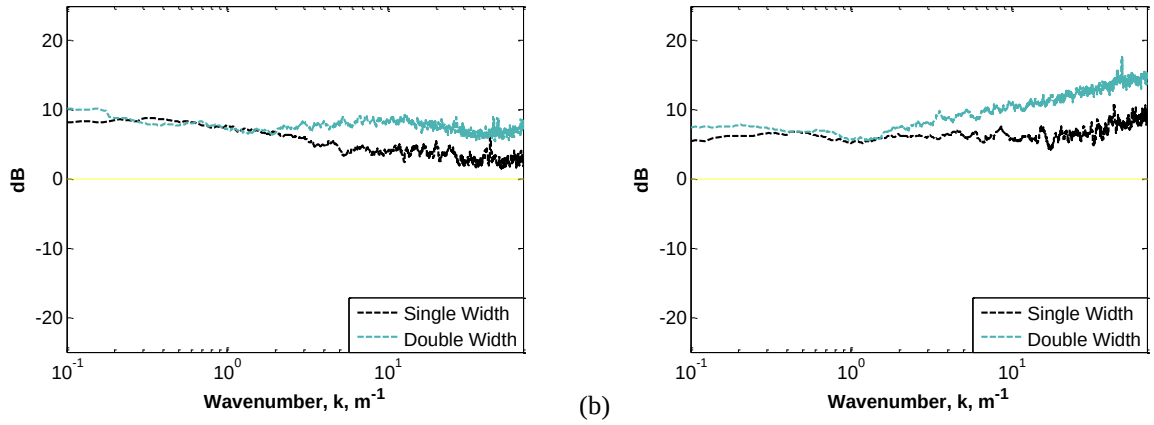

FIG. 49. Comparison of the measured energy spectra reductions of the (a) horizontal and (b) vertical components of the turbulence, in decibels, inside of a single and a double width wind fence with an open bottom gap and at 40% wall porosity. Data was measured on 3/3/12 and 4/17/13.

width fence are only better than the single width fence for wavenumbers above k = 1 m^{-1}. The reductions also improve at low wavenumbers, but the wavenumber at which this occurs differs. For the horizontal turbulence the improvement occurs below k = 0.2 m^{-1} and at k = 0.4 m^{-1}. The reduction values at mid-level frequencies are approximately the same. This behavior for the horizontal turbulence is unique, since these reductions typically maintain a more constant and uniform distance, as seen in Fig. 48. The behavior for the vertical turbulence is very similar to the effect of the double height wind fence. This suggests that the expanding either the height or the width has a similar effect on the vertical turbulence.

(c) The measured turbulence spectra behind the wind fence

This section will present and discuss modifications to the wake turbulence at x = 0.3 m, 2.9 m, and 5.8 m behind the wind fence, relative to the turbulence in front of the wind fence. The reduction curves plotted in Fig. 50 demonstrate how doubling the wind fence height affects

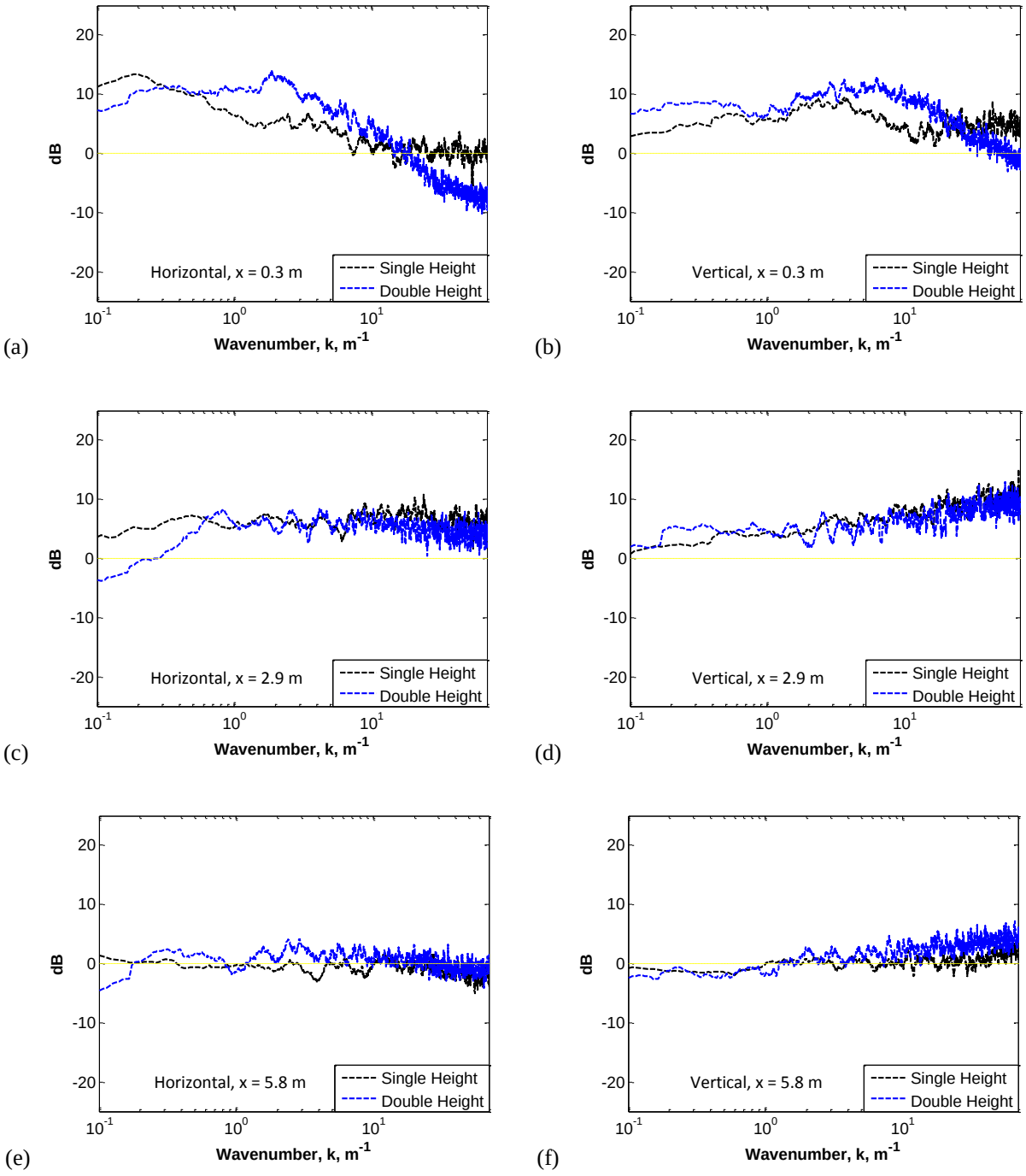

FIG. 50. Comparisons of the measured energy spectra reductions of the horizontal and vertical components of the turbulence, in decibels, behind a single and a double height fence with an open bottom gap, 40% wall porosity, and at distances of x = 0.3 m or x/H = 0.05, x = 2.9 m or x/H = 0.5, and x = 5.8 m or x/H = 1.0. Data was measured on 3/3/12 and 5/28/13.

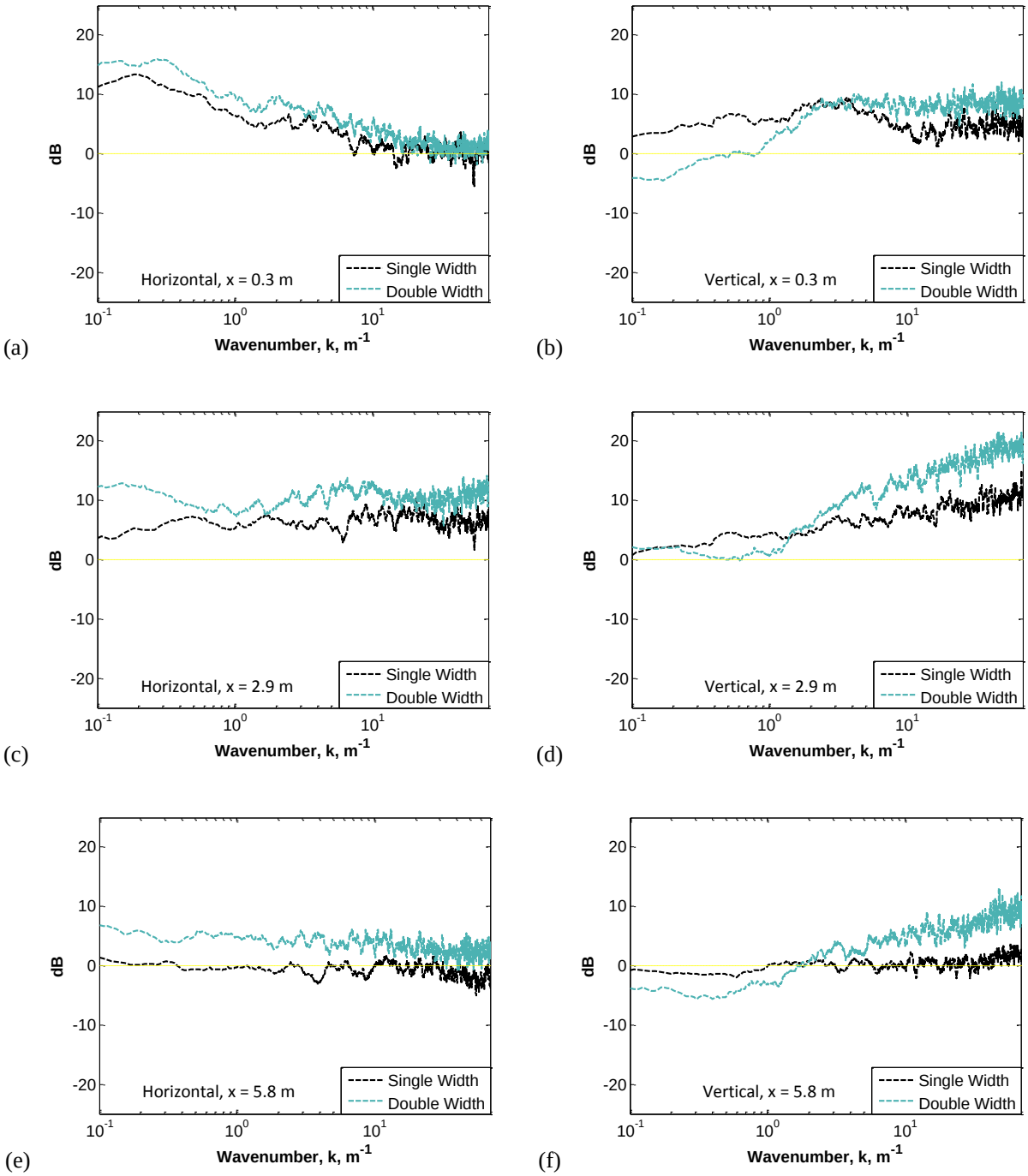

FIG. 51. Comparisons of the measured energy spectra reductions of the horizontal and vertical components of the turbulence, in decibels, behind a single and a double width fence with an open bottom gap, 40% wall porosity, and at distances of x = 0.3 m or x/W = 0.03, x = 2.9 m or x/W = 0.3, and x = 5.8 m or x/H = 0.7. Data was measured on 3/3/12 and 4/17/13.

the turbulence in the wake of the fence. The results show that the turbulence reduction curves are significantly different and generally better immediately behind (x = 0.3 m, x/H = 0.05) the double height fence as compared to the single height fence. However, the turbulence reductions for the double and single height fences are approximately the same for the other two locations, x = 2.9 m and 5.8 m. Therefore, except for distances very close to the fence (within half of its height), the turbulence is relatively insensitive to any adjustments and changes to the height of the wind fence enclosure. This is unexpected since increasing the height and width of the wind fence should cause a major disruption to the flow around and through the wind fence enclosure.

The results in Fig. 51 demonstrate how doubling the wind fence width affects the turbulence measured on the lee side of the fence. The lee side region starts immediately behind the fence and extends to a distance that is approximately two-thirds the distance of the fence width, and two times the height. As expected, the turbulence reduction curves show a consistent decrease in the turbulence at all regions behind the fence, when the diameter is expanded. Therefore, unlike increasing the height, the turbulence is affected by the diameter of the wind fence.

iii. Discussion and Conclusions

Increasing the wind fence height principally causes wind noise reductions to shift to lower frequencies. This shift does not completely scale with respect to height, which suggests that the shift is due to the wind fence's effect on the atmospheric boundary layer profile rather than scaling laws. The data shows that increasing the wind fence height has little effect on the turbulence, velocity gradient, and the resulting decrease to the turbulence-shear interaction inside

the fence. Therefore the improved reductions are due to an increased averaging area and perturbing the low frequency source region for the turbulence-shear and turbulence-turbulence interactions located at higher levels in the atmosphere.

Expanding the wind fence diameter significantly increases the wind noise reductions, but does not cause the reduction to shift in frequency. This confirms the hypothesis that the shift to lower frequencies is caused by modifications to the atmospheric boundary layer at higher elevations. The turbulence and velocity profile data show that the noise contribution due to the turbulence-shear interaction inside the wind fence should increase. However the significant decrease in the total measured wind noise implies that this increase is negligible, while the enlarged surface averaging and expanded separation distance between the microphone and the surface interactions have a significant impact on wind noise reductions.

In summary, optimizing wind noise reductions will depend on the reduction goal. If the goal is to shift the reduction to lower frequencies, then the height should be increased. If the goal is to maximize the reductions for the same frequency band then the diameter should be expanded. Simultaneously doubling both the height and the width was not possible for this study. However, based on the evidence that reductions significantly improve as either the height or width increase, it is very likely that the best overall reductions can be achieved by increasing both dimensions, rather than just one.

D. Measurement Series 4: Concentric Secondary Wind Barriers

The fourth measurement series investigated how adding secondary wind barriers to the wind fence will affect the noise reductions. The series also investigated how the velocity profiles inside the fence, the turbulence measured inside the fence, and the wake turbulence behind the fence were affected, as well as their influence on the wind noise reduction. Three different secondary barriers were tested during this investigation. The first was a small hollow hemispherical dome made of open celled polyurethane foam,[77] which was added to all the different fence configurations and treatments that have been described in this dissertation—porosity, roof, bottom gap, doubling height, and doubling width. This foam dome will generally be referred to as "the dome." It is approximately 0.6 m high, has an interior diameter of 1.06 m, an exterior diameter of 1.22 m, and the walls are approximately 0.08 m thick. The pore density is approximately 40 ppi; see Fig. 52a. The second and third barriers were the standard 5.0 m

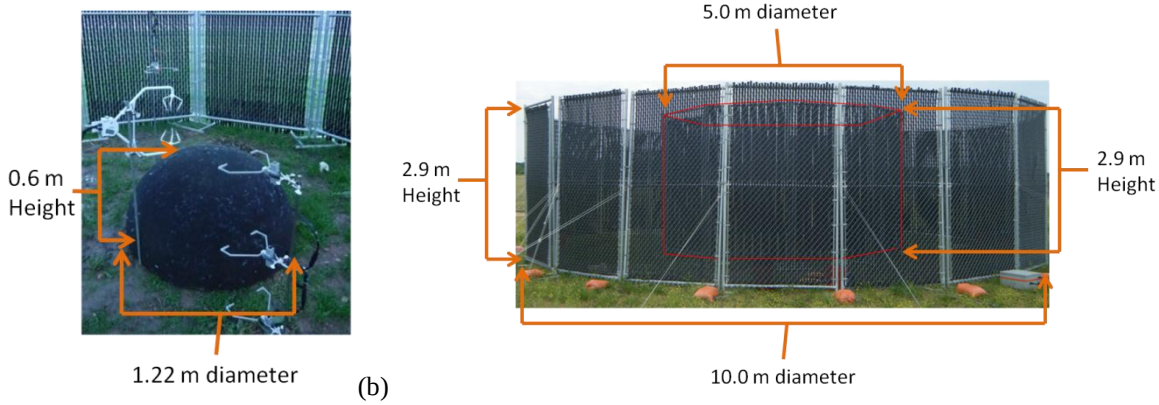

FIG. 52. Dimensions for the concentrically combined wind fences for (a) the foam dome set at center of the enclosure and (b) the 5.0 m diameter wind fence (highlighted in red) set inside the 10.0 m diameter wind fence.

diameter (single width) wind fence enclosure with 40% and 55% wall porosities. These were set inside the 10.0 m diameter (double width) wind fence enclosure; see Fig. 52b. In general a wind fence enclosure that has been combined with a secondary wind barrier will be referred to as a "double layer" or "combined" wind fence, while a wind fence that has not been combined with a secondary wind barrier will be generally referred to as a "single layer" or "non-combined" wind fence. For completeness noise reductions for a "triple layer" wind fence were also measured. This triple layer fence was comprised of the 10.0 m diameter wind fence combined with both the 5.0 m diameter wind fence, and the foam dome.

i. Effect on the measured wind noise spectra

(a) Hemispherical Foam Dome

The first part of the investigation focused on the effect on the wind noise spectra measured at the center of a normal, single height and width wind fence when the small foam dome was used as the secondary wind barrier. The effect is shown in Fig. 53 which displays the

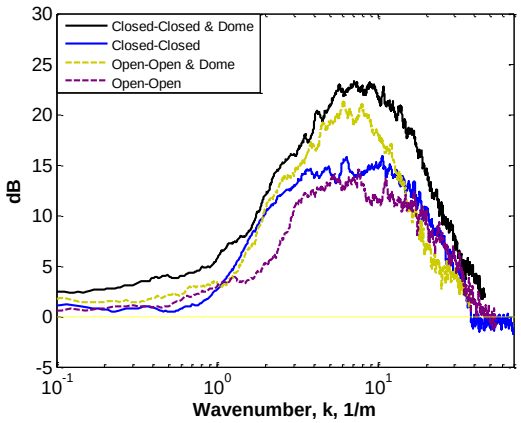

FIG. 53. Measured wind noise spectra reductions, in decibels, of the double and single layer forms of an open top-open bottom gap wind fence and a closed top-closed bottom gap wind fence, at 40% outer wall porosity. The double layer consists of the original wind fence combined with the foam dome. Data was measured on 4/25/12, 4/6/12, 3/6/12, and 3/3/12.

results of the foam dome combined with a wind fence that has an open bottom gap and open top, and to a wind fence that has a closed bottom gap and closed top. In both cases noise reductions improve by 6-8 dB. A similar improvement was observed for all wall porosities. The overall noise reductions improved when the open top was covered with a porous roof and the bottom gap was closed. The best reductions for the combined dome with the single width and height wind fence system were achieved for the wind fence enclosure with a closed top and closed bottom gap.

The second part of the investigation focused on the dome's effect as a secondary wind barrier on the wind noise measured by the double height wind fence. The effect is displayed in Fig. 54, which shows the noise reductions for the single and double height wind fences combined with the dome, and the non-combined double height wind fence. The results demonstrate that adding the dome improves reductions by about 5-10 dB, with maximum reduction values at approximately 23 dB. The wavenumber range where the maximum reductions occur also shifts from about k = 4 m^{-1} to k = 6 m^{-1}. Despite this shift, the magnitude for the low frequency end of the reduction curves stay the same or are slightly improved. Comparisons between the combined

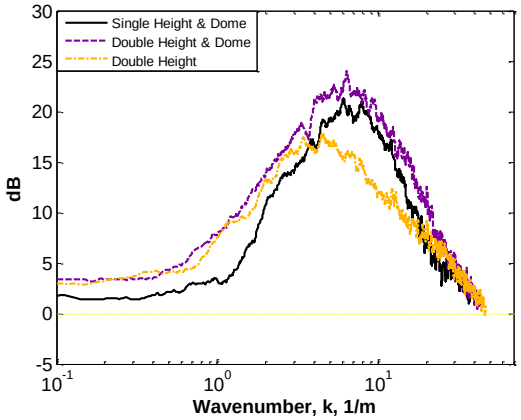

FIG. 54. Measured wind noise spectra reductions, in decibels, of the double height wind fence combined with the dome, the single height wind fence combined with the dome, and the double height fence without the dome. All fences had an open bottom gap and 40% outer wall porosity. Data was measured on 5/28/13 and 3/6/12.

single height fence and the combined double height fence also show that the dome and the double height system are comparable to or better than the reductions for the dome and single height wind fence, especially in the low wavenumber range.

The third part of the series investigated the effect of the dome on the wind noise measured by the double width wind fence. Fig. 55 displays the noise reductions for the single and double width wind fences combined with the dome, as well as the non-combined double width wind fence. The reduction curves demonstrate that adding the dome as a secondary wind barrier improves the noise reductions by about 10 dB when the exterior wall porosity is 55% and by about 1-2 dB when the exterior wall porosity is 40%. This difference is due to the more efficient reductions of the non-combined 40% fence versus the non-combined 55% fence. The measured maximum reductions for the combined 40% and 55% double width fences are typically between 25-27 dB, at k = 7-8 m^{-1}. This is a 5 dB improvement over the combined single width fence. The data also shows that the reductions for the non-combined double width wind fence are highly variable. Therefore, it is not possible to determine if adding the dome to a

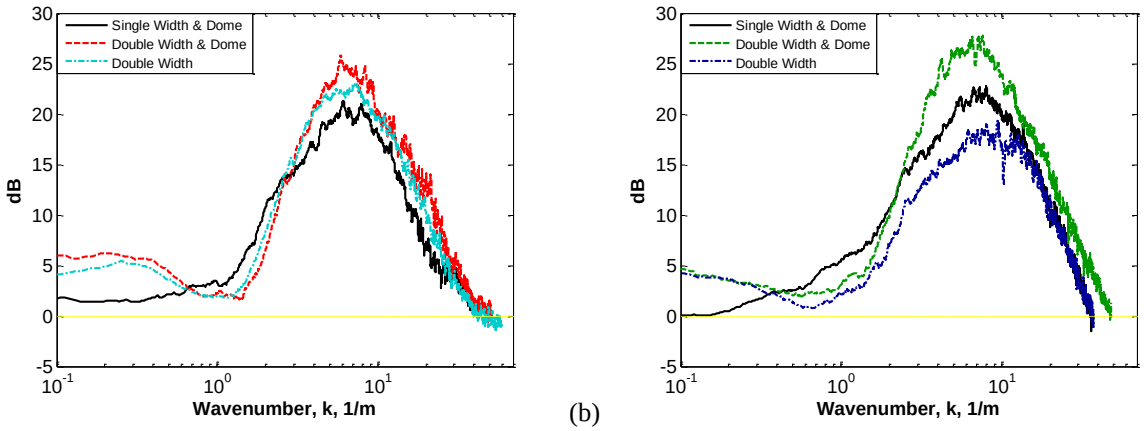

FIG. 55. Measured wind noise spectra reductions, in decibels, of the double width wind fence combined with the dome, the single width wind fence combined with the dome, and the double width wind fence without the dome. The fences in plot (a) had an open bottom gap and 40% outer wall porosity. The fences in plot (b) had a closed bottom gap and 55% outer wall porosity. Data in plot (a) was measured on 4/17/13 and 3/6/12. Data in plot (b) was measured on 4/9/13 and 3/7/12.

single width wind fence is better than simply enlarging the overall width. Adding a dome does, however, cause reductions to be approximately the same for wind fences of similar size but differing porosity. Regardless, the best results are achieved with the secondary barrier in the double width fence. Finally, in general, the addition of the dome enhances the reductions over the entire measured spectrum and in all aspects of the primary wind fence, regardless of the size, porosity, bottom gap, or roof treatment.

(b) Porous Wind Fences

This section will consider the effect of using the single width wind fence at 40% and 55% wall porosities as secondary wind barriers. The measured noise reductions due to the combination of the double width wind fence with the single width wind fences are shown in Fig. 56. The measured wind noise spectra reductions of the combined dome and double width fence are also shown in Fig. 56. The data indicates that the two single width wind barriers have a similar effect to the dome on the noise reductions—the noise reductions are enhanced at all

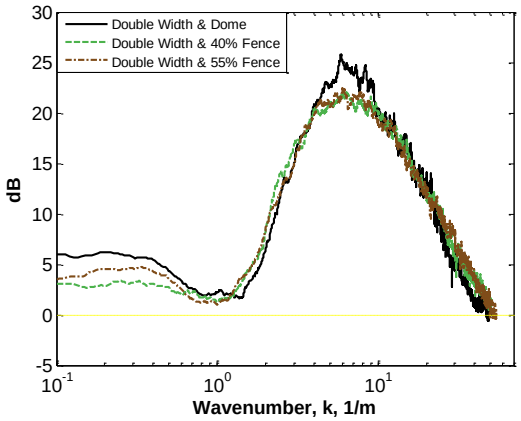

FIG. 56. Measured wind noise spectra reductions, in decibels, of the 40% porous double width wind fence combined with the three secondary wind barriers: the foam dome, the 40% porous wind barrier, and the 55% porous wind barrier. Data was measured on 4/17/13, 5/14/13, and 5/20/13.

points along the measured spectrum. There is little to no difference between the reductions for the 40% and 55% porous wind barriers combined with the double width fence. Generally, the reductions of these two combined systems match the reduction values of the combined dome and double width wind fence enclosure. However, the double layer fence with the dome achieves better reductions at the peak of the curve, by about 2-6 dB between k = 5-10 m^{-1}, and by 2-3 dB for wavenumbers lower than k = 1 m^{-1}. Therefore, of the three types of secondary barriers that were tested, the small foam dome is the best. The results are unexpected since the foam dome has a significantly smaller surface area than the single width wind fences, and should therefore be less effective at abating noise due to reduced area averaging. The reductions for the dome may be better since it has a closed top and a thicker porous wall, which makes it better for improving reductions for a low average flow speed and a turbulent interior flow.

The investigation also evaluated the effectiveness of adding a tertiary wind barrier. The triple layer wind enclosure is comprised of the double width fence, the single width fence, and the foam dome. Due to the significant improvement in reducing wind noise by the addition of a secondary wind barrier and by Ballard's and Izqierdo's study, a triple layer wind fence enclosure

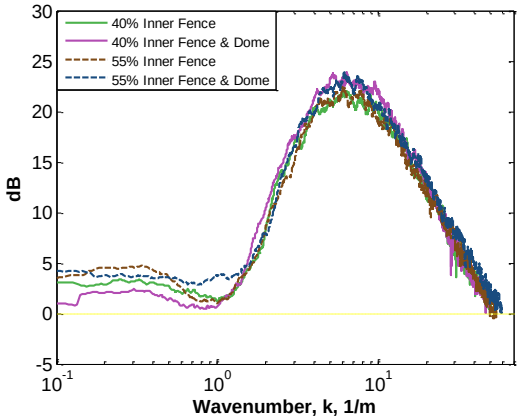

FIG. 57. Measured wind noise spectra reductions, in decibels, of the 40% porous double width wind fence combined with secondary wind barriers (the 40% and 55% porous fences) and a tertiary wind barrier (the foam dome). Data was measured on 5/14/13 and 5/20/13.

should result in larger reductions. However, as seen in Fig. 57, the improvement is marginal, with reductions improving by only 1-2 dB. The small improvement indicates that the first secondary wind barrier reduces the interior generated wind noise to negligible levels with respect to the surface averaged noise so that the addition of a third wind barrier has only a small effect.

The final part of the noise reduction investigation evaluated the individual effects of the dome, the wind fence, and how they contribute to the overall noise reductions when combined together. The results of this investigation are shown in Fig. 58, which displays the reductions for the non-combined dome, the non-combined single width wind fence at 40% porosity, and the reductions when this fence and dome are combined together. The results demonstrate that individually, the dome and the mid-level porosity wind fence achieve approximately the same level of noise reduction, about 15 dB, and that the reductions for the wind fence are better at lower wavenumbers. These improved reductions are due to a small shift to a lower frequency band, which is likely due to the wind fence's height relative to that of the dome. When the wind fence enclosure and dome are combined, the reductions tend to shift to the same wavenumber band as the wind fence, or the primary barrier, and improve by about 5-8 dB. This data suggests

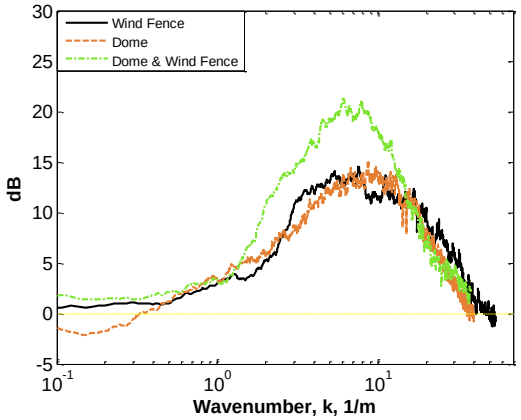

FIG. 58. Measured wind noise reductions, of the non-combined dome, the non-combined single width and height wind fence at 40% porosity, and the combination of the dome and 40% wind fence. Data was measured on 3/3/12 and 4/10/13.

that the secondary wind barrier does not affect the wind noise generated at the surface of the primary wind fence, since the noise reductions do not improve in either a multiplicative or additive manner when the dome is combined with the wind fence. If the reductions were multiplicative then the combined wind barrier system would achieve maximum noise reductions of approximately 30 dB; and if the combined reductions were additive then the maximum reductions would be no more than 6 dB. This supports the theory that the dome only affects the residual wind noise inside the primary fence and that the reductions are due to the elimination of this residual wind noise. The data also suggests that the dome may be more efficient as a secondary filter than as a primary filter. In general, combining the dome and wind fence achieves better noise reductions than what they could achieve individually. Similar conclusions can be drawn from the results for the combined single width and double width wind fence. Finally, the results show that the base reduction level and the wavenumber band where the reductions occur are determined by the primary wind fence these reductions are then enhanced by the secondary barrier.

ii. Effect on the meteorological variables

This part of the investigation will present and discuss the changes to the wind velocity profile, the turbulence inside the fence, and the turbulence behind the fence when a secondary wind barrier is added to the wind fence enclosure. Only the meteorological data for the 40% and 55% porous wind fences acting as secondary barriers will be presented since, due to the size of the foam dome and the size of the anemometers, it was not possible to measure the turbulence or velocity profiles inside of the dome.

(a) The wind velocity profile

The effect of adding a secondary wind barrier on the velocity profile is displayed in Fig. 59, which shows the velocity profiles measured inside the non-combined double width fence, the double width fence combined with the 40% porous single width wind barrier, and the double width fence combined with the 55% porous single width wind barrier. The exterior wall porosity is at 55%. The data shows that the velocity profiles for the two double layer wind fences are nearly vertical, and that the average velocity is approximately 0.55 m/s, which is much slower than the non-combined double width fence. The low average wind velocity and the nearly

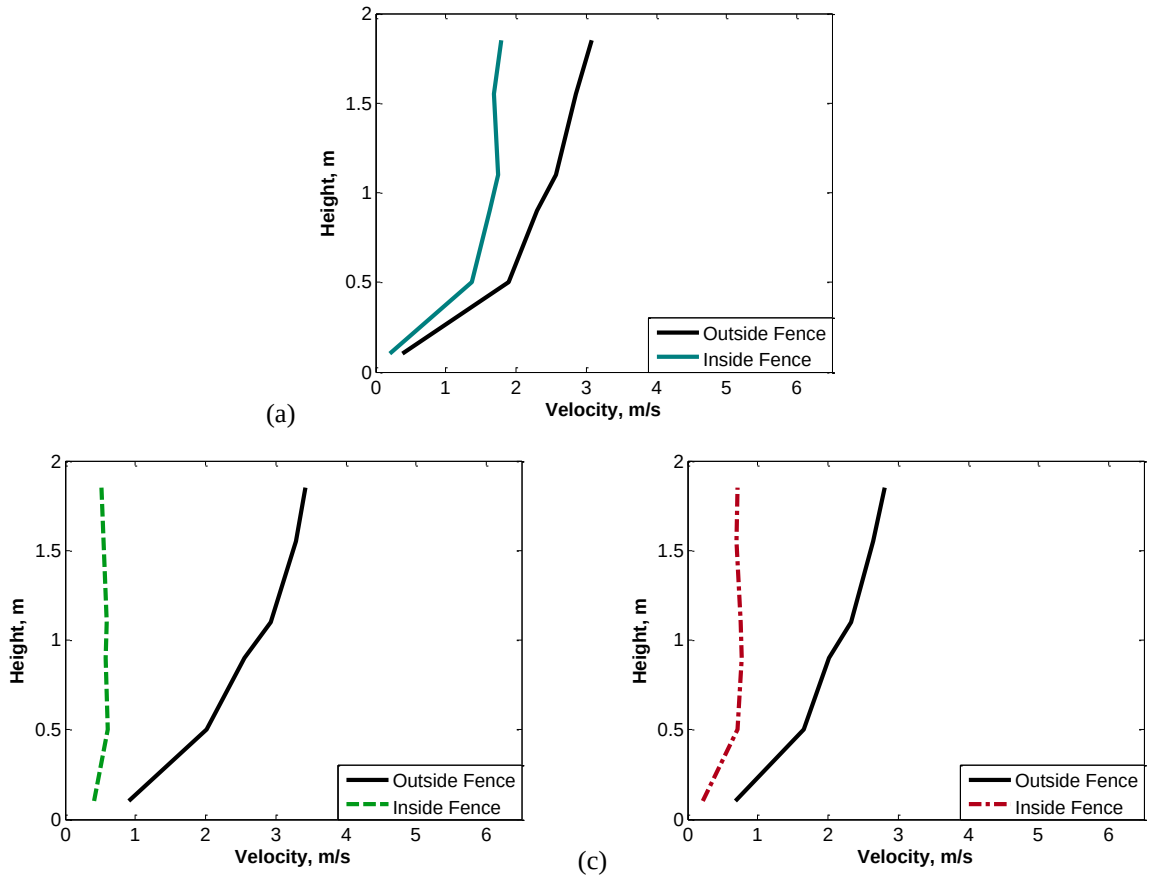

FIG. 59. Measured wind velocity profiles inside and outside of (a) a double width fence at 55% wall porosity by itself, and then concentrically combined with (b) the single width 40% porous wind barrier and (c) the single width 55% porous wind barrier. Data was measured on 4/17/13, 5/15/13, and 5/21/13.

vertical profile shapes indicate that the velocity gradient at the center of the double layer wind fence is nearly zero.

(b) The measured turbulence spectra inside the wind fence enclosure

This section will discuss the effect on the turbulence inside the wind fence enclosure relative to the turbulence incident to the fence when it is combined with a secondary wind barrier. Figure 60 displays the reductions of the horizontal and vertical components of the turbulence inside a non-combined double width fence and then combined with the 40% and 55% single width fences. The results indicate that the energy reductions for the horizontal component of the turbulence are better at all frequencies than the turbulence energy reductions for a single layer wind fence enclosure. The reductions for the vertical components of the turbulence however are improved only for wavenumbers higher than k = 0.6 m^{-1}. The reductions however, are still positive, and hence turbulence is not generated. Overall, the addition of a secondary wind barrier decreases the amount of turbulence inside the wind fence enclosure.

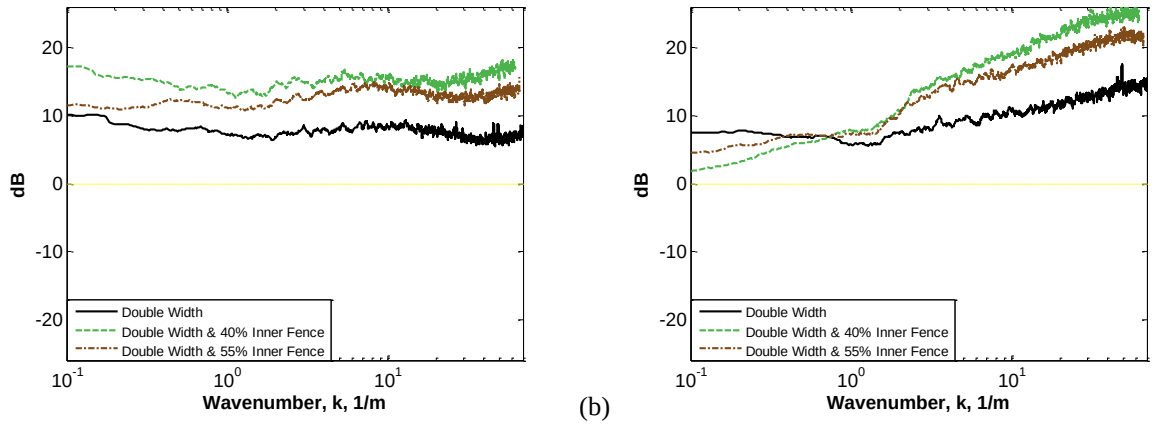

FIG 60. Measured reductions of the (a) horizontal and (b) vertical components of the turbulence energy spectra, in decibels, inside of a double width wind fence at 40 and 55% wall porosities with and without secondary wind barriers. The secondary wind barriers are the 40% and 55% single width porous wind fences. Data was measured on 4/17/13, 5/14/13, and 5/20/13.

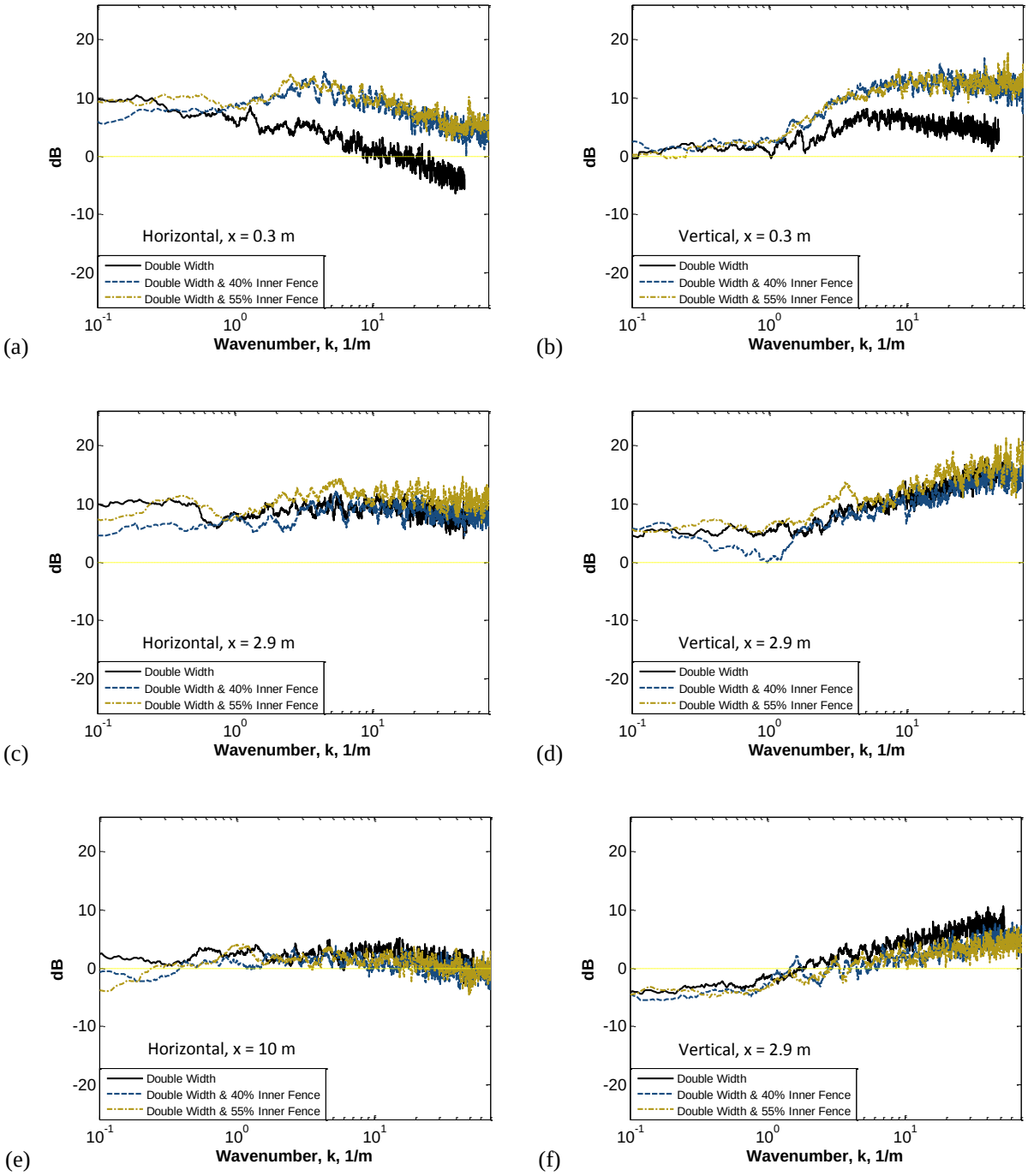

FIG. 61. Measured reductions of the horizontal and vertical components of the turbulence energy spectra, in decibels, behind a double width wind fence at 55% wall porosity both with and without secondary wind barriers, and at distances of x = 0.3 m, 2.9 m, and 10.0 m. Data was measured on 4/9/13, 5/15/13, and 5/21/13.

(a) The measured turbulence spectra behind the fence enclosure

This section will discuss the effects on the turbulence field in the lee side region of the wind fence as a secondary wind barrier is added to the enclosure. The effect is seen in Fig. 61, which shows the turbulence reductions for the non-combined double width fence and the double width wind fence combined with the 40% and 55% secondary fences. The data indicates that the turbulence immediately behind the fence is significantly reduced at high frequencies. However, the reductions are approximately the same at low frequencies, or at wavenumbers below $k = 1\ m^{-1}$. Likewise, there is little to no difference at all frequencies between the turbulence fields of the single layer and double layer wind fences beyond $x = 2.9$ m. At $x = 10.0$ m vertical turbulence is generated at low frequencies. However, as discussed in previous cases, the magnitude of this generated turbulence is less than the horizontal turbulence and is therefore not significant. Therefore, except at distances immediately behind the wind fence, the wake turbulence is relatively insensitive to the addition of a secondary wind barrier.

ii. Discussion and Conclusions

The purpose of this measurement series was to investigate if additional wind barriers would improve noise reductions. Based on the study by Ballard and Izquierdo,[69] noise reductions were expected to improve as additional wind barriers were added. Three types of wind barriers were tested: a small hemispherical foam dome, the single width and height wind fence at 40% wall porosity, and the single width and height wind fence at 55% wall porosity. Of the three barriers tested, the small hemispherical foam dome proved to be the most effective.

In general, adding an additional wind barrier improved wind noise reductions, regardless of the type of wind fence. The data showed that the base reduction level and frequency band where the reductions occur are determined by the primary wind fence. The secondary wind barrier then enhances the magnitude of these reductions over the entire measured wind noise spectrum. The data shows a decrease in the velocity gradient and turbulence inside the double layer wind fence. This results in a further minimization of the turbulence-shear interaction inside the wind fence. The improved reductions are also due to the outer fence reducing the wind speed and the scale size of the turbulence down to levels that are most easily and effectively reduced by the secondary wind barriers. The secondary barrier then further decreases the interior generated wind noise to negligible levels with respect to the noise generated by the turbulence-shear interaction and stagnation pressure at the enclosure's exterior surface.

The results indicated that reductions for the single width and height wind fence were optimized when the dome was combined with a closed top and closed bottom gap wind fence. This result was unexpected since an open bottom gap fence provided the best reductions for all the previous measurements. The improvement may be explained due to the dome's increased effectiveness when the wind velocity is low. The open bottom gap allows a higher wind velocity at the base of the fence, which produces a more uniform vertical velocity profile and less shearing. However, the dome is less effective at reducing residual wind noise at these higher velocities. Eliminating the bottom gap reduces the wind velocity at the base of the fence to a level where the dome is most effective, improving the wind noise reductions.

A triple layer wind barrier, consisting of the double width fence as the primary layer, a porous single width fence as the secondary layer, and the foam dome as the tertiary layer was tested and compared with a combined single and double width wind fence. The improvements

were small, and therefore a tertiary wind screen shows no significant benefit to the wind fence design and optimization.

The maximum reductions for this measurement series and all measurement series were observed for the combined dome and double width wind fence, while the best reductions for wavenumbers between 0.3 and 3 m^{-1} were observed for the combined dome and double height wind fence. Reductions below $k = 0.3\ m^{-1}$ were comparable for the two combined enclosures, but the reductions for the combined dome and double width fence are slightly better. Design recommendations for either type of fence will depend on the targeted frequency range for improving wind noise reductions. Regardless of the design of the exterior or primary wind fence layer, a secondary layer should be added to the enclosure in order to maximize the enclosure's wind noise reduction capability.

E. Measurement Series 5: Comparisons to Other Reduction Methods

During the course of this research all wind fences were evaluated by comparing the measured wind noise spectra from a sensor located at the center of the wind fence and covered with a 1" thick sheet of porous foam, with the top of the foam mounted flush to the ground (see Fig. 62b), relative to another identical pressure sensor located upwind of the wind fence and mounted in the same manner. This method evaluated the noise reductions with respect to the wind noise contribution of the turbulence-shear interaction at the Earth's surface. This measurement method was chosen since the turbulence-shear interaction is well understood due to Jiao Yu's research and theory.[36-37, 40] In other wind noise research, reductions have been measured in comparison to a pressure sensor placed unscreened, in the flow, and mounted on the Earth's surface (Fig. 62a). In order to compare the results of this dissertation with other noise reduction studies it is necessary to have a set of reduction measurements between an unscreened

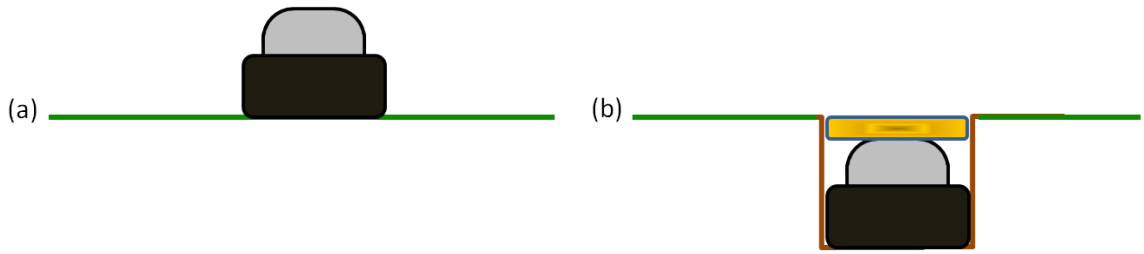

FIG. 62. Illustration depicting the NCPA pressure sensor (a) surface mounted on the ground and unscreened, (b) flush mounted to the ground and covered with a 1" thick sheet of foam. The illustration is not drawn to scale.

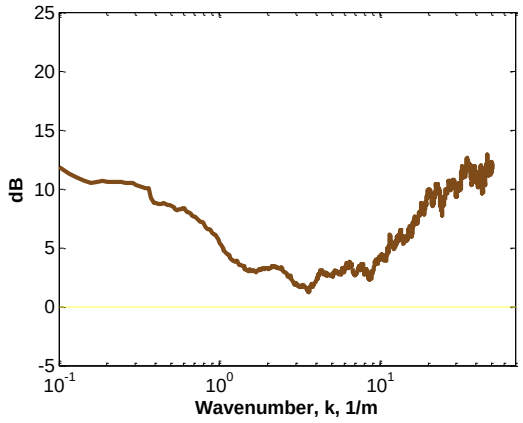

FIG. 63. Measured wind noise reductions, in decibels, of a screened flush mounted sensor relative to an unscreened surface mounted sensor. Data was measured on 4/12/13.

pressure sensor and a surface mounted pressure sensor. This measurement series provides the information necessary to relate results of this dissertation to other wind noise reduction studies.

The noise reductions for the screened-flush mounted pressure sensor relative to the bare-surface mounted pressure sensor are shown in Fig. 63. The results indicate that reductions are significantly improved simply by removing the sensor from the flow and covering it with a screen. The gain in noise reductions are 1.5 dB and better, depending on the frequency, with the best reductions occurring for wavenumbers below k = 1 m^{-1} and above k = 10 m^{-1}, with reduction gains of 3-12 dB. The improved reductions are due to the surface mounted pressure sensor measuring the wind noise generated by the stagnation pressure, while the flush mounted sensor measures the noise due to the turbulence-shear interaction. Using an unscreened surface mounted sensor as the reference leads to higher reported reductions since the magnitude of the wind noise due to the stagnation pressure is higher than the noise generated by the turbulence-shear interaction. Further, results that rely on the stagnation pressure as a reference level will be more variable, since the effect of the stagnation pressure is more dependent on the size and shape of the pressure sensor as well as terrain and measurement conditions. Therefore, noise reduction

evaluations that use stagnation pressure as a reference signal should be reduced by at least 1-10 dB for low and high frequencies, and by 1-3 dB for mid-range frequencies, when compared with the results of this dissertation.

F. Investigation of Observed Narrowband Infrasonic Noise Source

During the course of these investigations there were instances where a limited frequency band of the wind noise reductions approached zero. Examples of these instances are shown in Figs. 42, and 55-57. The purpose of this investigation is to determine the source of these narrow band abatements by comparing the measured wind noise spectra to the measured turbulence spectra and to known sources of infrasonic acoustic signals. The abatement was most often observed in the data measured with the 10 m diameter wind fence, both individually and when combined with a secondary or tertiary wind barrier, and usually occurred at approximately k = 1 m^{-1}; see Fig. 64a. Typically, wind noise reductions start at wavenumbers that coincide with turbulence scales that are approximately the same size of the wind fence enclosure. Reductions below this point are either non-existent or have a flat response with a small consistent wind noise

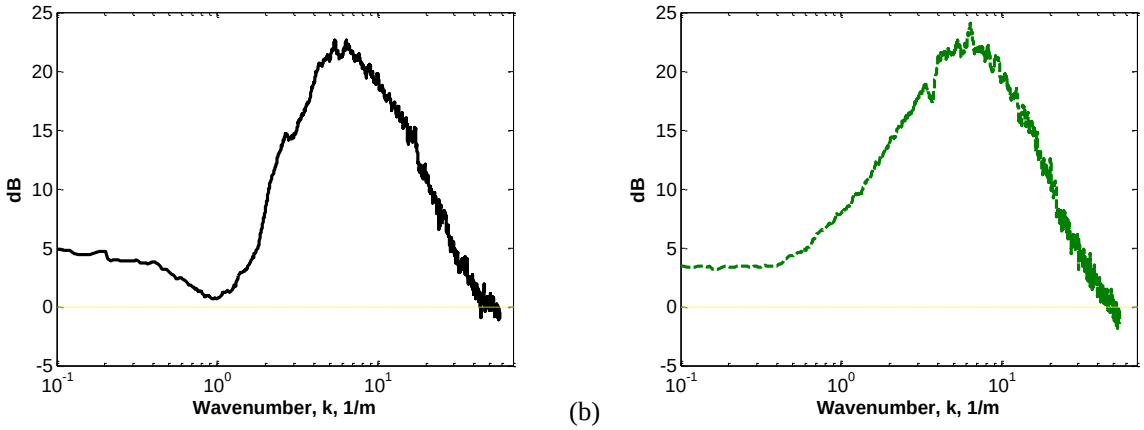

FIG. 64. Measured wind noise spectra reductions, in decibels, of (a) a combined double width wind fence showing narrow band abatement at approximately k = 1.0 m^{-1}, and (b) a combined double height wind fence without the narrow frequency band abatement. Data was measured on 4/16/13 for the double width fence and 5/28/13 for the double height fence.

reduction of 2-6 dB, as seen in Fig. 64a. In other situations, like those shown in Figs. 42, 55-57, and 63b, the reduction curves show a narrow band abatement near this transition region. Due to its narrowness of the frequency band, its location, and the augmentation of the wind noise spectra, the three possible sources of this abatement are vortex shedding, resonance, or microbaroms.

Vortex shedding occurs when the turbulent wake flow behind a bluff body begins to oscillate at a particular frequency.[3, 70] If this phenomenon was the source of the narrow band abatement there would also be narrow band spectral peaks in the wake turbulence. Resonance

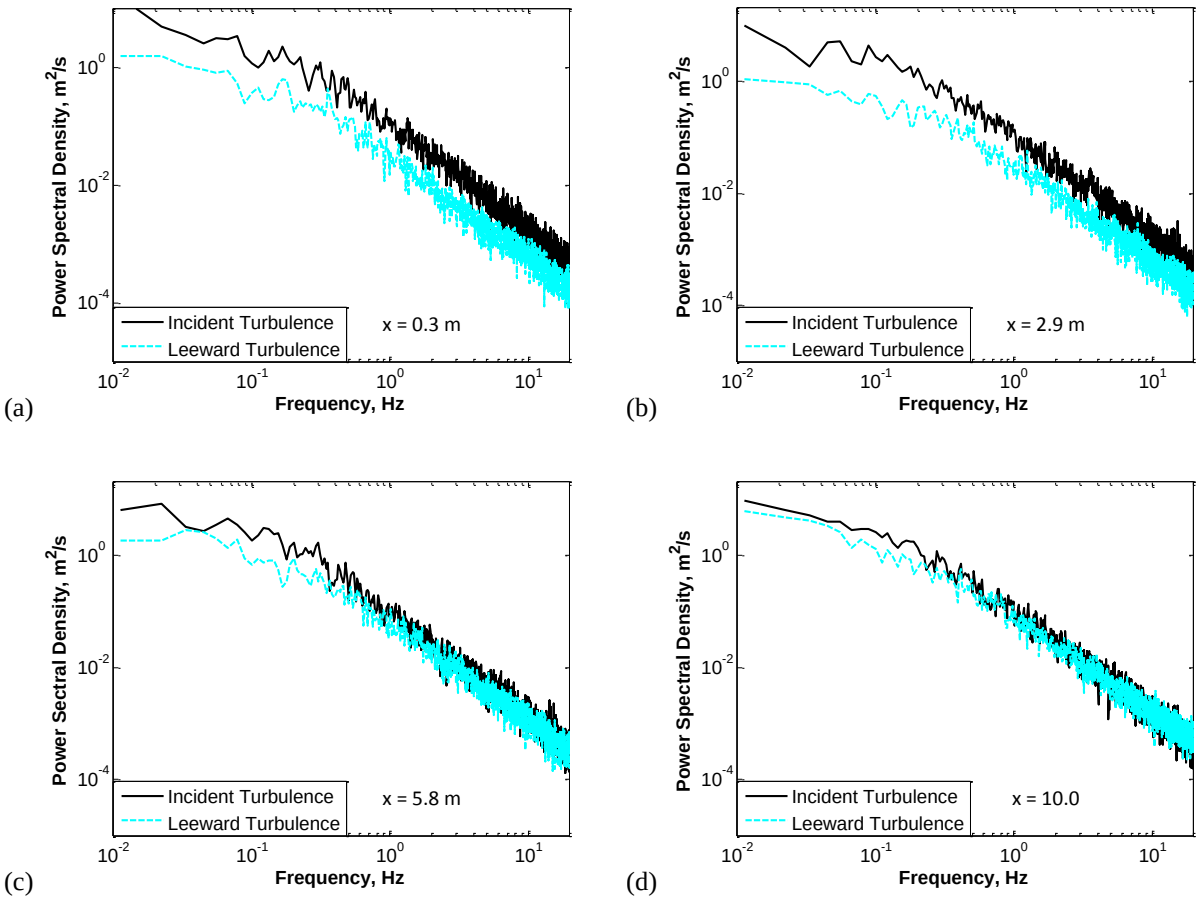

FIG. 65. Measured power spectral density of the turbulence at four locations of increasing distance behind a combined double width wind fence. The distances were approximately (a) x/H = 0.1, (b) x/H = 1.0, (c) x/H = 2.0, and (d) x/H = 3.0. Data was measured on 4/16/13.

due to wind flow occurs when a bluff body, driven by turbulence, vibrates at its own natural frequency. The noise arises when vibrations of the bluff body couple with the turbulent flow.[70] Therefore, if resonance was the source of the abatement then there also should be spectral peaks in the wake turbulence data. However, as displayed in Fig. 65, which shows the wake turbulence behind the fence up to a distance of three times the fence height, there are no discernible spectral peaks in the turbulence data. This leaves microbaroms as the most likely source of the narrowband abatement in the wind noise reduction data.

Microbaroms are narrow-band (0.1-0.5 Hz) coherent infrasonic acoustic signals. They are generated in marine storms by the non-linear interaction of the ocean surface waves with the atmosphere. These signals have an amplitude of about 80 dB, propagate over very long ranges, and can be readily detected.[78-80] However, microbaroms are only detected when interfering noise sources, such as wind noise, are below the microbarom amplitude level, see Fig. 66. This plot displays wind noise as measured with a 30 m pipe array at various wind speeds, measured in July 2007.[50] The microbaroms, even with a noise reduction device, were only detected for wind speeds lower than 10 km/h, or approximately 2.8 m/s.

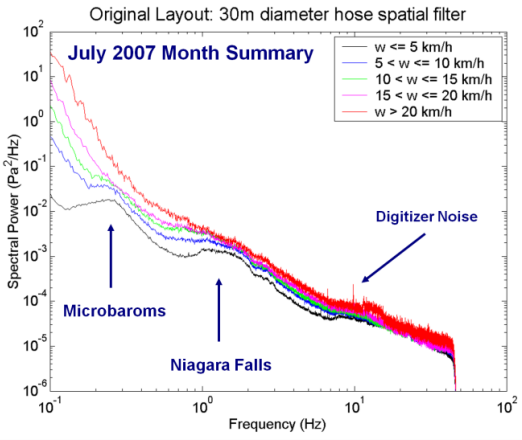

FIG. 66. Wind noise spectra as measured by a 30 m hose array under various windy conditions over the course of the month of July 2007. Figure taken from D. ReVelle.[50]

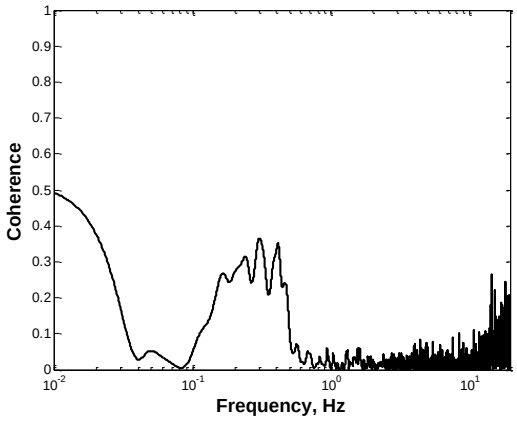

FIG. 67. Normalized coherence of the wind noise measured inside and outside of a combined dome and double width wind fence. Data was measured on 4/16/13.

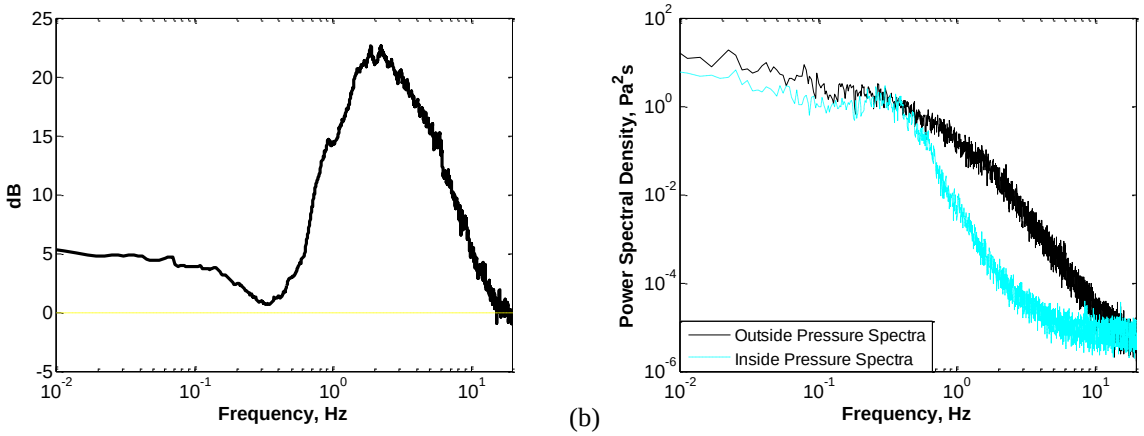

(a) (b)

FIG. 68. Measured wind noise spectra of a combined dome and double width wind fence. The reductions, in decibels are shown in part (a) and the power spectral densities of the wind noise measured inside and outside of the fence are shown in (b). Data was measured on 4/16/13.

Since microbaroms are infrasonic, their acoustic correlation length is larger than the 10 m separation distance between the sensors set inside and outside of the wind fence. We can verify that microbaroms are the source of the narrow band abatement of the wind noise by correlating the wind noise spectra measured by the two pressure sensors. As seen in Fig. 67 the correlation produces a coherence peak between 0.2 and 0.4 Hz, which is within the microbarom bandwidth.

The data in Fig. 68 shows that the abatement typically occurs at the same frequencies as the coherence peak. Therefore the narrowband abatement is due to the detection of microbaroms. We also assume that if microbaroms had not been detected, then the reductions at the transition point would be at a constant 3-6 dB. It is interesting to note that each time microbaroms were detected during the course of the research for this dissertation, the average wind velocities were typically between 3-5.6 m/s, or between 11-20 km/h, which is well above the limits for the 30 m hose array shown in Fig. 66. These results demonstrate the effectiveness of an optimized wind fence for reducing wind noise levels sufficiently to detect infrasonic acoustic signals.

CHAPTER V

EMPIRICAL MODEL

In order to gain a better understanding of the reduction mechanics of a wind fence, it is helpful to develop a simple mathematical model that can provide an estimation of a wind fence's noise reduction capability. Additionally the model can demonstrate how the three different source regions—I) inside the fence, II) the surface of the fence, and III) the undisturbed flow region outside the fence—and the flow interactions in these regions contribute to the overall noise sensed at the center of the fence. The model is derived by adapting the wind noise theories developed by Yu, [36-37, 40] Raspet et al.,[15] and Webster et al.[26] to the measured wind velocity profiles and turbulence spectra incident to and inside the fence, the correlation length of the measured wind velocity around the barrier, and the mean velocity distribution near the barrier's surface.

We have proposed that the primary mechanism for noise reduction for a large cylindrical wind barrier is the decorrelation of the incident turbulence over the surface of the barrier which results in a more efficient area averaging of the pressure fluctuations at the surface of the wind barrier. We propose that the wind noise measured at the center of the wind fence is due to a combination of 1) the turbulence-turbulence and turbulence-shear interactions inside the fence, 2) the stagnation pressure and turbulence-shear interactions at the surface of the fence, and 3) the turbulence-shear and turbulence-turbulence interactions in the unperturbed flow away from the

wind fence. Assuming that all contributions from the interactions in these three regions add incoherently, we also propose that the wind noise at the center of the wind barrier can be determined by combining the noise spectra contributions from the three identified regions of flow,

$$|P(f)|^2 = |P_I(f)|^2 + |P_{II}(f)|^2 + |P_{III}(f)|^2 . \quad (16)$$

We expect that for a well designed wind fence the contribution from the interior flow should be small, and that the wind noise will be primarily due to the interactions at the barrier's surface. The derivation of the empirical model and comparisons of the calculated estimates to the measured wind noise will verify these assumptions.

This chapter will be divided into four sections. The empirical models for Regions I and III will be described in the first two sections since they have already been derived by Jiao Yu. The model for Region II will then be derived in the third section. The fourth section will show and discuss the comparisons of the measured and calculated wind noise.

1. Empirical Model for Regions I

We wish to derive a mathematical model that will estimate the wind noise measured inside a wind fence at a given size and porosity. Measurements show that wind noise is reduced for frequencies with wavelengths that are approximately the same size as the wind fence height and smaller; see Fig 69. Physically, this can be explained by considering the size of the turbulence relative to the size of the wind fence (see the illustration in Fig. 70 which shows two turbules with wavelengths, λ = 3 and 10 m, incident to and passing through a 3 m high and 5 m

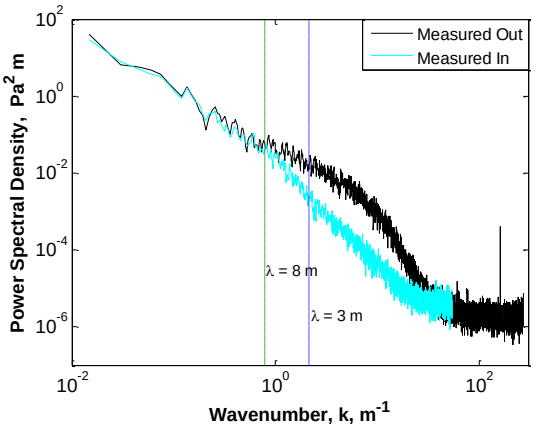

FIG. 69. Power spectral density with respect to 1/wavelength of the measured inside and outside wind noise. Data was measured on 3/3/12 for a 55% porous wind fence.

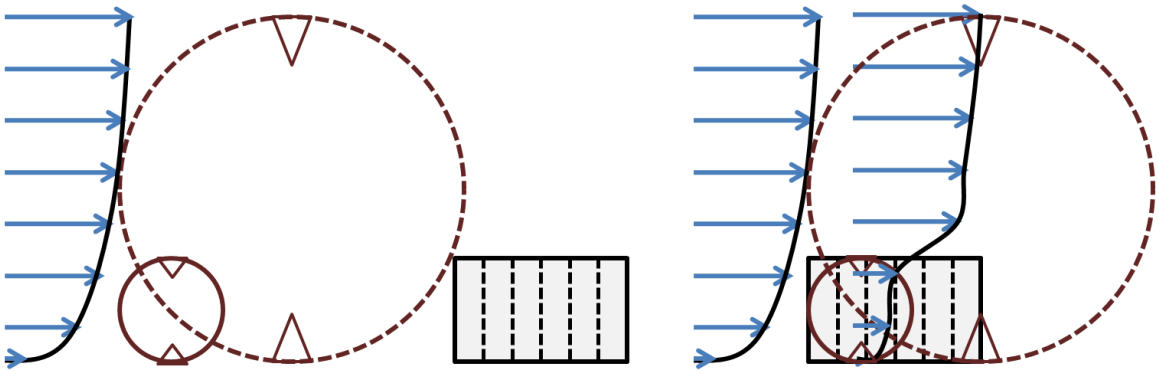

FIG. 70. Scaled two dimensional turbulence, with wavelengths of λ = 3 and 10 m, and the wind velocity profile incident to and passing through a wind fence from left to right.

diameter wind fence). High frequency turbulence is small enough such that it is modified as it passes through the interior of the enclosure. Also, since the turbulence is small enough to be contained within the enclosure, high frequency wind noise is generated by the flow interactions inside the fence (Region I). Therefore, a model that can provide good estimates of the wind noise due to the interior flow will be used to estimate the high frequency contribution of the wind noise.

As discussed in Chapter III, Yu's multi-exponential model [Eq. (11) and shown here again as Eq. (17)],

$$\left|P_I\left(0,k_1\right)\right|^2 = \frac{440C\lambda^4\rho_0^2k_1^2}{9\pi} \sum_{i=0,j=0}^{i=n,j=m} s_i s_j e^{\left(\beta_i+\beta_j\right)d} \int_0^\infty\int_0^\infty \frac{dk_2dk_3}{\left[1+\left(k\lambda\right)^2\right]^{\frac{17}{6}}} \left[\int_d^h e^{-\left(\kappa+\beta_i\right)x_2}\sin\left(k_2x_2\right)dx_2 \int_d^h e^{-\left(\kappa+\beta_j\right)x_2'}\sin\left(k_2x_2'\right)dx_2'\right], \quad (17)$$

is used to predict the noise due to the interior flow interactions, and should therefore provide a good estimate for the high frequency component of the wind noise. Yu's k-fitting method, as described in Chapter III, is used to determine C and λ for this region since the reduced wind speeds set the majority of the wind noise in the inertial range.

2. Empirical Model for Region III

Wind noise measurements also show that at low frequencies, or frequencies with turbulence wavelengths that are at least two times the height of the wind fence, the wind noise measured inside the fence is approximately the same as the noise that would be measured if there was no wind fence present; see Fig. 69. This is equivalent to the flow in Region III, the undisturbed flow located away from the wind fence enclosure. Physically, this can again be explained by considering the size of the turbulence relative to the size of the wind fence, and is illustrated in Fig. 70. Physically, low frequency turbulence and the related velocity profile are large enough to be relatively unaffected by any perturbations due to the wind fence. Therefore a model that can satisfactorily predict the wind noise for an undisturbed flow will be used to estimate the low frequency component of the wind noise.

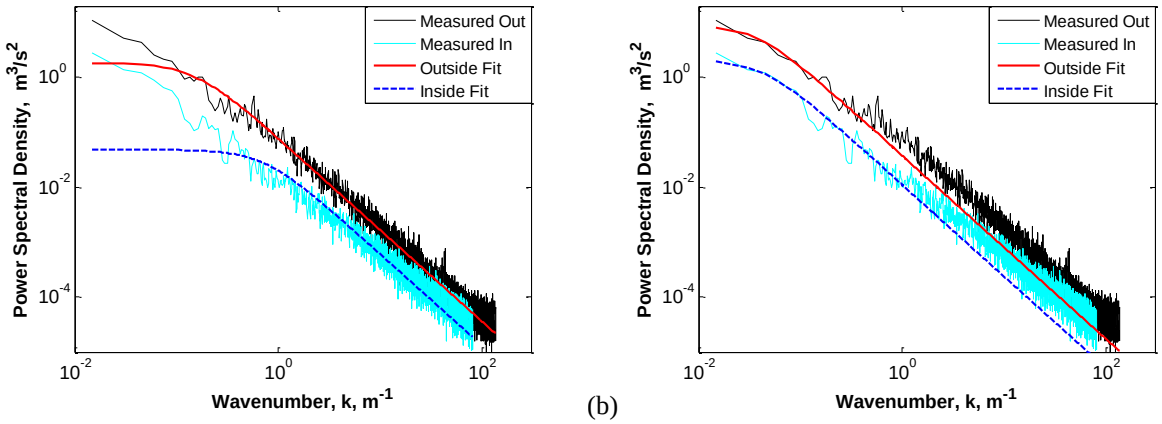

FIG. 71. Power spectral density of the measured inside and outside turbulence spectra with their respective fits using (a) the product of k method, the (b) the non-multiplicative method. Data was measured on 3/3/12 for a wind fence 3 m high and 5 m in diameter with 55% wall porosity, an open top, and an open bottom gap.

Jiao Yu's logarithmic model [Eq. (15) and shown here again as Eq. (18)],

$$\left|P_{III}\left(0,k_1\right)\right|^2 = P_{III}\left(0,k_1\right)P_{III}^*\left(0,k_1\right) = \frac{440a^2\rho_0^2k_1^2C\lambda^4}{9\pi}\int_0^\infty\int_0^\infty \frac{dk_2dk_3}{\left[1+\left(k\lambda\right)^2\right]^{\frac{17}{6}}}\left[\int_d^\infty \frac{e^{-\kappa x_2}\sin\left(k_2x_2\right)}{x_2-d+x_0}dx_2\int_d^\infty \frac{e^{-\kappa x_2'}\sin\left(k_2x_2'\right)}{x_2'-d+x_0}dx_2'\right], \quad (18)$$

is used to predict the noise contributions for the undisturbed flow and therefore, should provide good estimations for the low frequency component of the wind noise as measured inside the wind fence enclosure. Yu's k-fitting method for determining the C and λ terms for the flow in Region III is not used for this calculation since this technique provides very poor fits at low frequencies; see Figs. 69 and 71a. Jiao's fitting technique was designed to give optimal fits for wavenumbers in the inertial range of the spectra, since data in this range was statistically more reliable than the source region due to the shorter duration of her measurements. This dissertation emphasizes the contribution from lower frequencies. Therefore, to better accommodate for the longer measurement periods and lower frequency noise contributions, the parameters C and λ for

Region III are determined by fitting the measured velocity spectrum to the von Karman form of the spectrum without multiplying by the wavenumber, *k*, or:

$$F_{11}^{1}(k_1) = \frac{C}{\left[1 + (k_1\lambda)^2\right]^{\frac{5}{6}}}. \tag{19}$$

This method more heavily weights the low frequency contribution, which gives a better fit for low frequencies and its noise sources. However, as seen in Fig. 71b, this method gives poor fits for wavenumbers higher than k = 1 m^{-1}; hence it will only be used for the low wavenumber contributions. Even though this fitting method improves the fits at low wavenumbers, it is still limited since the measured data is not as statistically reliable at the lowest wavenumbers. As a result, some early roll off still occurs in the calculated noise spectra.

3. Empirical Model for Region II

There is no existing model to describe the wind noise contributions from the interaction of the wind velocity at the surface of the fence, or Region II. A model for this region will be derived here by adapting the calculations for estimating the wind noise at the center of a spherical windscreen. Like electrostatic theory, where the potential at the center of a hollow conductor is equal to the mean value of the potential over its surface, the wind noise at the center of a wind fence can be determined by the area average of the pressure fluctuations at its surface,

$$p(0,t) = \frac{1}{4\pi}\int_{s>0} p(\theta, z, t)\frac{\vec{r}}{r^3}\cdot d\vec{s} \tag{20}$$

where $\vec{r} = b\hat{r}$, $d\vec{s} = \hat{r}bdzd\theta$, $r = \sqrt{b^2 + z^2}$, and *b* is the radius of the wind fence. Substituting these values into Eq. (20) and multiplying by 2 to account for the doubling of the sound pressure level at a boundary, the pressure at the center of the wind fence becomes

$$p(0,t) = \frac{1}{2\pi}\int_g^h \int_0^{2\pi} p(\theta,z,t)\frac{b^2}{\left(b^2+z^2\right)^{\frac{3}{2}}}dzd\theta \tag{21}$$

where *h* is the height of the wind fence and *g* and is the size of the bottom gap. and *h* is the wind fence height. The surface pressure, $p(\theta,z,t)$, is determined by taking the divergence of the Navier-Stokes equation. Following the method shown in Appendix A the surface pressure and surface velocity distributions are related by:

$$-\frac{1}{\rho_0}\nabla p = \frac{1}{2}\nabla\left(\vec{u}\cdot\vec{u}\right) - \vec{u}\times\nabla\times\vec{u} \tag{22}$$

where p is the surface pressure and u is the velocity distribution near the surface of the fence.

Equation (22) can be expanded in terms of the mean and fluctuating components of the pressure and velocity by applying the Reynolds decomposition, or:

$$\nabla\left(P+p'\right) = -\frac{1}{2}\rho_0\nabla\left[\left(\vec{U}+\vec{v}'\right)\cdot\left(\vec{U}+\vec{v}'\right)\right] + \rho_0\left[\left(\vec{U}+\vec{v}'\right)\times\nabla\times\left(\vec{U}+\vec{v}'\right)\right] \tag{23}$$

where P and $\vec{U}$ are the mean components of the pressure and velocity, and p' and $\vec{v}'$ are the fluctuating components of the pressure and velocity. Expanding Eq. (23) further gives:

$$\begin{aligned}\nabla\left(P+p'\right) = &-\frac{1}{2}\rho_0\nabla\left[\vec{U}\cdot\vec{U} + 2\vec{U}\cdot\vec{v}'+\vec{v}'\cdot\vec{v}'\right]+\ldots \\ &\rho_0\left[\left(\vec{U}\times\nabla\times\vec{U}\right)+\left(\vec{v}'\times\nabla\times\vec{U}\right)+\left(\vec{U}\times\nabla\times\vec{v}'\right)+\left(\vec{v}'\times\nabla\times\vec{v}'\right)\right]\end{aligned} \tag{24}$$

The mean pressure is determined by taking the time average of Eq. (24), and assuming that $\bar{p}' = \bar{v}' = 0$, which gives:

$$\nabla P = -\frac{1}{2}\rho_0 \nabla\left[\vec{U}\cdot\vec{U} + \overline{\vec{v}'\cdot\vec{v}'}\right] + \rho_0\left[\left(\vec{U}\times\nabla\times\vec{U}\right) + \left(\overline{\vec{v}'\times\nabla\times\vec{v}'}\right)\right] \tag{25}$$

Subtracting Eq. (25) from Eq. (24) and dropping the primes gives the fluctuating surface pressure distribution,

$$\begin{aligned}\nabla p = -\frac{1}{2}\rho_0 \nabla\left[2\vec{U}\cdot\vec{v} + \vec{v}\cdot\vec{v} - \overline{\vec{v}\cdot\vec{v}}\right] + \ldots \\ \rho_0\left[\left(\vec{v}\times\nabla\times\vec{U}\right) + \left(\vec{U}\times\nabla\times\vec{v}\right) + \left(\vec{v}\times\nabla\times\vec{v}\right) - \left(\overline{\vec{v}\times\nabla\times\vec{v}}\right)\right]\end{aligned}. \tag{26}$$

The mean velocity, $\vec{U}$, is larger than the fluctuating turbulence, $\vec{v}$, so the $2\vec{U}\cdot\vec{v}$, $\left(\vec{v}\times\nabla\times\vec{U}\right)$, and $\left(\vec{U}\times\nabla\times\vec{v}\right)$ terms dominate , and Eq. (26) can be simplified to:

$$\nabla p = -\rho_0\nabla\left(\vec{U}\cdot\vec{v}\right) + \rho_0\left[\left(\vec{v}\times\nabla\times\vec{U}\right) + \left(\vec{U}\times\nabla\times\vec{v}\right)\right]. \tag{27}$$

The $\nabla\times\vec{U}$ term is approximately the spatial derivative of the mean velocity or $\partial U_i/\partial x_j$, which is very large since the change from high to low wind velocity is drastic and occurs over small distances. Therefore, since $\nabla\times\vec{v} \approx \vec{k}\vec{v}$ and $\frac{\partial U_i}{\partial x_j} > \vec{k}\vec{v}$, the $\left(\vec{v}\times\nabla\times\vec{U}\right)$ term in Eq. (27) dominates the $\left(\vec{U}\times\nabla\times\vec{v}\right)$ term, and Eq. (27) can be further simplified to:

$$\nabla p = -\rho_0\nabla\left(\vec{U}\cdot\vec{v}\right) + \rho_0\left(\vec{v}\times\nabla\times\vec{U}\right). \tag{28}$$

The surface pressure is obtained by integrating both sides of Eq. (28), which gives:

$$p = -\rho_0\vec{U}\cdot\vec{v} + \rho_0\int\left(\vec{v}\times\nabla\times\vec{U}\right). \tag{29}$$

The first term in Eq. (29) incorporates not only the stagnation pressure, which is the $\rho_0 v_1 U_1$ in the direction of flow, but all components of the mean and fluctuating wind velocity, on the fence's surface, or $\rho_0 v_i U_i$. This term will be referred to as the Bernoulli term. The second term describes the pressure due to the turbulence-shear interaction.

The turbulence-mean shear term in Eq. (29) is usually smaller than the Bernoulli term. This can be understood by considering the magnitude of the Bernoulli term and the turbulence-shear interaction on a bluff body placed in the flow. Jiao Yu's estimates showed that the magnitude of the Bernoulli term is larger than the turbulence-shear for a screened microphone placed in a flow, except at low frequencies; see Fig. 72a.[13] Later, the improved calculations showed that the turbulence-shear term is lower than the Bernoulli term at all frequencies; see Fig. 72b.[40] Therefore, $\rho_0 \vec{U} \cdot \vec{v} > \rho_0 \int \left(\vec{v} \times \nabla \times \vec{U} \right)$, and Eq. (29) can be approximated to:

$$p \cong -\rho_0 \vec{U} \cdot \vec{v} \,. \tag{30}$$

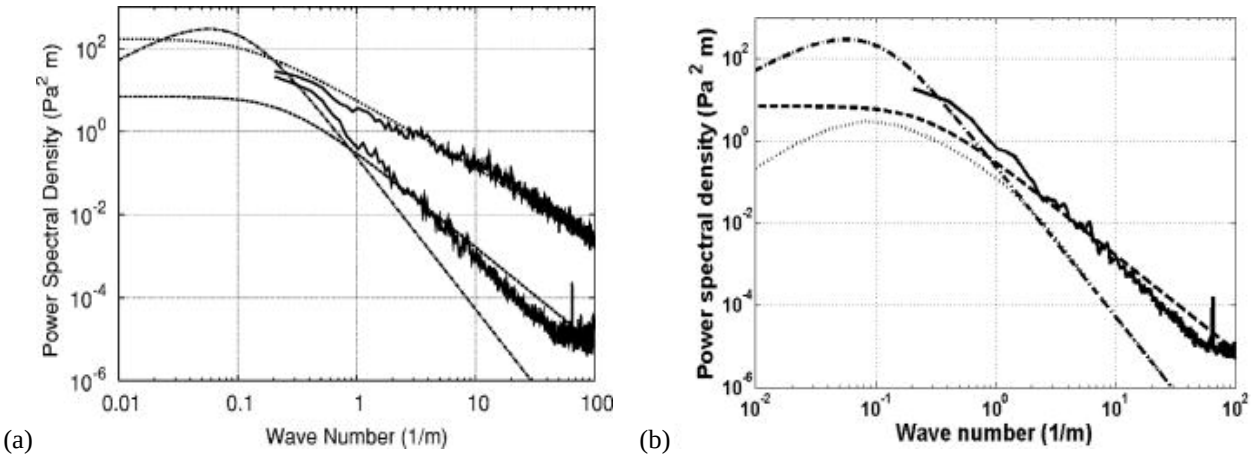

FIG. 72. Predicted wind noise spectra for the stagnation pressure [highest dotted line, plot (a)] and the turbulence-shear interaction [dotted line, plot(b)] for a microphone inside a 1.0 m windscreen set above the ground in the flow. Plot (a) taken from Yu et. al[13] and plot (b) taken from Yu et al.[40]

The $\vec{v}$ term in Eq. (30) represents the incident turbulence and the respective distribution around the wind fence, which can be written as $u(z,\theta,t)$. The mean velocity term in Eq. (30), $\vec{U}$, represents the mean velocity incident to the wind fence and its distribution around the wind fence with respect to the azimuthal angle, θ. The distribution can be determined by assuming that the mean velocity distribution is approximately uniform, and by subtracting the mean velocity of the turbulence inside the wind fence, U_{in}, from the mean velocity of the turbulence outside of the fence, U_{out}, or

$$\vec{U} = U_{out} - U_{in}. \tag{31}$$

Substituting $u(z,\theta,t)$ for $\vec{v}$, Eqs. (30 and 31) into Eq. (21), taking the Fourier transform into wavenumber space gives, and writing p as P_{II} gives:

$$P_{II}(0,k) = \frac{\rho_0}{2\pi}\int_g^h\int_0^{2\pi}\frac{(U_{out}-U_{in})u(z,\theta,k)}{(b^2+z^2)^{\frac{3}{2}}}b^2\,dz\,d\theta. \tag{32}$$

The power spectra for the pressure is determined by taking the average of the product of $P_{II}(0,k)$ and $P_{II}^*(0,k)$, which gives:

$$\left\langle\left|P_{II}(0,k)\right|^2\right\rangle = \left\langle P_{II}^*(0,k)P_{II}(0,k)\right\rangle = \frac{\rho_0^2 b^4}{(2\pi)^2}\int_g^h\int_0^{2\pi}\int_g^h\int_0^{2\pi}\frac{(U_{out}-U_{in})}{(b^2+z'^2)^{\frac{3}{2}}}\frac{(U_{out}-U_{in})}{(b^2+z^2)^{\frac{3}{2}}}\left\langle u^*(z',\theta',k)u(z,\theta,k)\right\rangle dz'\,d\theta'\,dz\,d\theta \tag{33}$$

where U_{out} and U_{in} are constants in time, and assuming homogeneous turbulence, then

$$\left\langle u^*(z',\theta',k)u(z,\theta,k)\right\rangle = u^*(k)u(k)e^{-\alpha(k)\sqrt{[b(\theta'-\theta)]^2+(z'-z)^2}} \tag{34}$$

where $\alpha(k)$ has units of m^{-1}, and is equal to one over the correlation length. Substituting Eq. (34) into Eq. (33), the pressure at the center of the barrier due to Region II becomes:

$$|P_{II}(0,k)|^2 = \frac{\rho_0^2 b^4}{(2\pi)^2} \int_g^h \int_0^{2\pi} \int_g^h \int_0^{2\pi} \frac{(U_{out}-U_{in})}{(b^2+z'^2)^{\frac{3}{2}}} \frac{(U_{out}-U_{in})}{(b^2+z^2)^{\frac{3}{2}}} u^*(k)u(k) e^{-\alpha(k)\sqrt{[b(\theta'-\theta)]^2+(z'-z)^2}} dz'd\theta' dz d\theta \quad (35)$$

The $u^*(k)u(k)$ is determined by fitting the measured velocity spectrum of the incident or outside flow to the von Karman form,

$$F(k) = \frac{C}{\left[1+(k\lambda)^2\right]^{\frac{5}{6}}}, \quad (36)$$

where C and λ are determined using the Yu's k-fitting method. Substituting Eq. (36) into Eq. (35), the pressure spectra becomes:

$$|P_{II}(0,k)|^2 = \frac{\rho_0^2 b^4 C}{(2\pi)^2} \int_g^h \int_0^{2\pi} \int_g^h \int_0^{2\pi} \frac{(U_{out}-U_{in})}{(b^2+z'^2)^{\frac{3}{2}}} \frac{(U_{out}-U_{in})}{(b^2+z^2)^{\frac{3}{2}}} \frac{e^{-\alpha(k)\sqrt{[b(\theta'-\theta)]^2+(z'-z)^2}}}{\left[1+(k\lambda)^2\right]^{\frac{5}{6}}} dz'd\theta' dz d\theta \quad (37)$$

B. Measurement of the correlation length, $1/\alpha(k)$

Based on the studies by Shields[63] and Priestly,[81-82] the correlation term is assumed to have the form of $R_{AB} = e^{-\alpha(k)x}$, where x is the position on and around the surface of the wind fence, and $\alpha(k)$ has the form of $\alpha(k) = \mu k^q$. Measurements indicate that the correlation length,

$1/\alpha(k)$, changes as the fence's surface porosity changes, therefore $\alpha(k)$ will be determined for each porosity.

The correlation length, $1/\alpha(k)$ was determined by measuring the wind noise around the fence at azimuthal angles of $\theta = 7^o$, 36^o, 72^o, 108^o, 144^o, and 180^o, with respect to the incident turbulence at $\theta = 0^o$; see Fig. 73. The measured wind noise was then filtered into octave band frequencies, with center frequencies between 0.01 and 20 Hz, and the filtered signals at each azimuthal angle were correlated with the signal at 0^o. The correlation of the filtered signal for each octave band was then fit to the general correlation function $R_i = e^{-a_i x}$; where x is the position on and around the barrier's surface, a_i is a fit parameter, and i is the center frequency for each octave band; see Fig. 74. The fit parameters were set into an array, α, with respect to the center frequencies for each octave band. Using Taylor's frozen turbulence hypothesis, $k = 2\pi f/U_c$, the center frequencies and octave bands were converted into wavenumber, k, by multiplying the center frequencies by $2\pi/U_c$, where U_c is the wind velocity; thus making α a function of k; see Fig. 75a. Assuming that $\alpha(k)$ has the form $\alpha(k) = \mu k^q$, the coefficients μ and q were determined by fitting the natural log of $\alpha(k)$ to a linear function, $\ln(\alpha) = q\ln(k) + b$, where

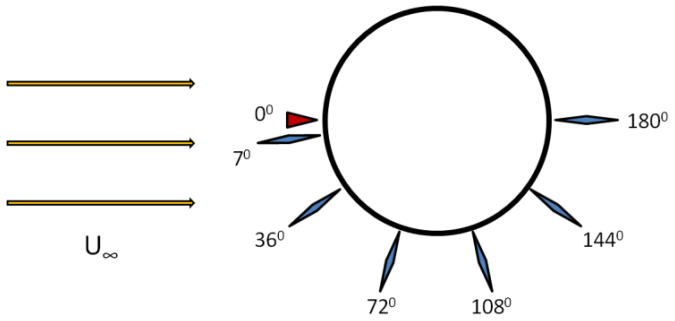

FIG. 73. Sketch of the positions around the wind fence for the measured correlations, with respect to the fence and the incident turbulence.

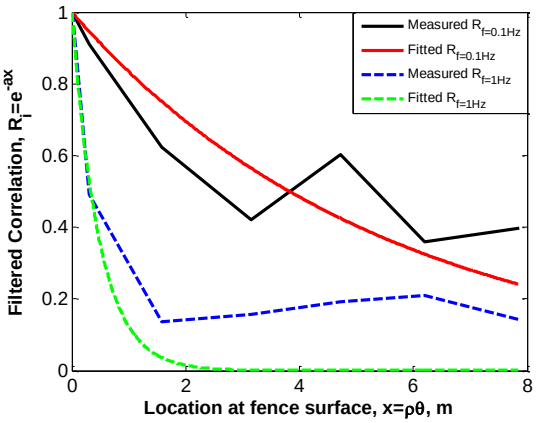

FIG. 74. Measured correlations around the surface of the 30% porous fence that have been filtered into octave band frequencies, and their respective fits to the form $R_i = e^{-a_i x}$.

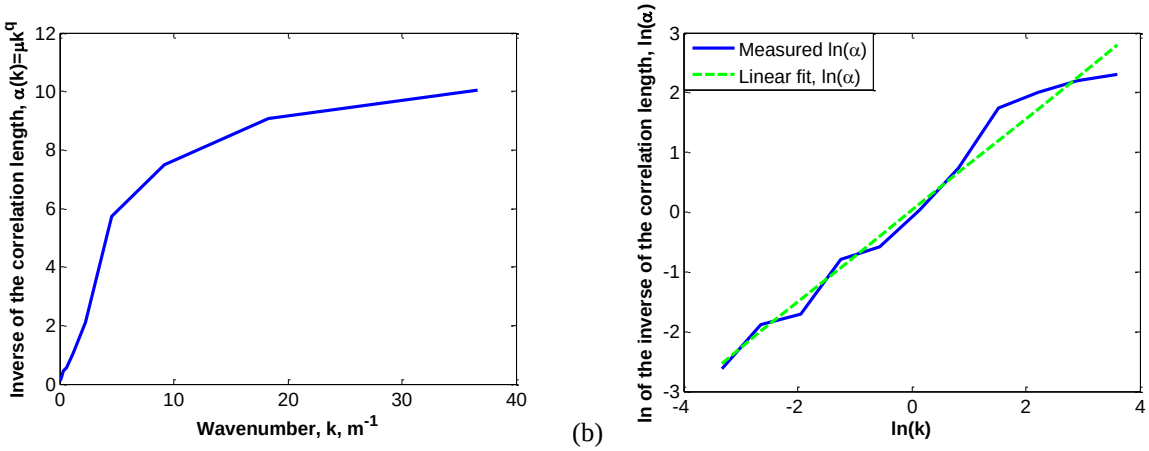

FIG. 75. The inverse correlation length α as a function of wavenumber as determined from fits to the measured correlations around a 30% porous fence in octave band frequencies. Plot (a) shows the linear graph, and plot (b) shows the ln(α) with its linear fit.

	μ	q
30%	1.0304	0.7674
40%	1.4142	0.6545
55%	1.6976	0.6076
65%	1.2786	0.7601
80%	1.5166	0.6681

TABLE III. Fitted values of μ and q for the correlation length function $1/\alpha(k) = (\mu k^q)^{-1}$ for the 30%, 40%, 55%, 65%, and 80% wall porosities of a single height and width wind fence with an open top and open bottom gap.

q and b are fit parameters and $b = \ln(\mu)$; see Fig. 75b. A correlation length, $1/\alpha(k)$, was determined for each of the five wall porosities using this method. The values of μ and q for each of the wall porosities are shown in Table III. Having verified the form for the inverted correlation length, $\alpha(k) = \mu k^q$, it was substituted into Eq. (37), and the wind noise contribution at the center of the wind fence from Region II becomes:

$$|P_{II}(0,k)|^2 = \frac{\rho_0^2 b^4 C}{(2\pi)^2} \int_g^h \int_0^{2\pi} \int_g^h \int_0^{2\pi} \frac{(U_{out} - U_{in})}{(b^2 + z'^2)^{\frac{3}{2}}} \frac{(U_{out} - U_{in})}{(b^2 + z^2)^{\frac{3}{2}}} \frac{e^{-\mu k^q \sqrt{[b(\theta'-\theta)]^2 + (z'-z)^2}}}{\left[1 + (k\lambda)^2\right]^{\frac{5}{6}}} dz' d\theta' dz d\theta \quad (38)$$

which is the final form for the wind noise contribution due to the turbulence and flow interactions at the surface of the fence.

4. Prediction and Measurement Comparisons

The predicted wind noise spectra at the center of the wind fence are determined by summing the three models together. However, since the wind velocity outside the fence is higher than the velocity inside the fence, the wavenumbers for the three different regions will also differ. As a result the models cannot be added together in wavenumber space since their respective magnitudes and wavenumber ranges will be misaligned. The models, however, can be accurately aligned and combined in frequency space. The models are converted to frequency space by multiplying the predicted power spectral densities by $2\pi/U_n$. The respective wavenumber ranges are converted by dividing by $2\pi/U_n$, where U_n is the average wind velocity

for the different flow regions. Hence in frequency space, the models for Regions I, II, and III are:

$$|P_I(0,f)|^2 = \frac{880C\lambda^4\rho_0^2k^2}{9U_I} \sum_{i=0,j=0}^{i=n,j=m} s_i s_j e^{(\beta_i+\beta_j)d} \int_0^\infty\int_0^\infty \frac{dk_2dk_3}{\left[1+(k\lambda)^2\right]^{\frac{17}{6}}} \left[\int_d^h e^{-(\kappa+\beta_i)x_2}\sin(k_2x_2)dx_2 \int_d^h e^{-(\kappa+\beta_j)x_2'}\sin(k_2x_2')dx_2'\right] \quad (39)$$

$$|P_{II}(0,f)|^2 = \frac{\rho_0^2b^4C}{2\pi U_{II}} \int_g^h\int_0^{2\pi}\int_g^h\int_0^{2\pi} \frac{(U_{out}-U_{in})}{(b^2+z'^2)^{\frac{3}{2}}} \frac{(U_{out}-U_{in})}{(b^2+z^2)^{\frac{3}{2}}} \frac{e^{-\mu k^q\sqrt{[b(\theta'-\theta)]^2+(z'-z)^2}}}{\left[1+(k\lambda)^2\right]^{\frac{5}{6}}} dz'd\theta'dzd\theta \quad (40)$$

$$|P_{III}(0,f)|^2 = \frac{880a^2\rho_0^2k^2C\lambda^4}{9U_{III}} \int_0^\infty\int_0^\infty \frac{dk_2dk_3}{\left[1+(k\lambda)^2\right]^{\frac{17}{6}}} \left[\int_d^\infty \frac{e^{-\kappa x_2}\sin(k_2x_2)}{x_2-d+x_0}dx_2 \int_d^\infty \frac{e^{-\kappa x_2'}\sin(k_2x_2')}{x_2'-d+x_0}dx_2'\right]. \quad (41)$$

The final form of the prediction is obtained by summing Eqs. (39-41) together, or:

$$|P(f)|^2 = |P_I(f)|^2 + |P_{II}(f)|^2 + |P_{III}(f)|^2. \quad (42)$$

Eq. (42) is converted back into wavenumber space using the free field mean wind velocity, U_{III}, for comparisons with the measured wind noise. For computational ease, the wind noise spectra for each region are computed separately and then combined together. Figs. 76-80 show comparisons of the measured wind noise spectra against the individual predicted noise contributions for Regions I, II, and III, and the summed predicted noise contributions for the 30%, 40%, 55%, 65%, and 80% wall porosities of a wind fence with an open top and open bottom gap. The individual predictions are plotted in frequency space, since that is the form in which they are added together. In general the slopes for the predictions for Region II, agree with

the measured wind noise data, however their magnitudes, most notably the 55% fence (Fig. 78) are low by a small factor. The low magnitudes indicate that the main source region may be located further from the wind fence than where the flow velocity was measured. This also indicates that the correlation lengths may be larger than those measured at the surface of the fence, and are likely closer to the size of the correlation length for the incident flow. Despite this, the low prediction provides a general idea of the noise contributions for the turbulence interactions at and near the surface of the wind fence.

The predicted and measured wind noise spectra for a wind fence with 30% porous walls are shown in Fig. 76. Part (a) shows the individual noise contributions for the three flow regions with the measured noise inside and outside of the fence, and part (b) shows the sum of the noise contributions for the three regions, $|P(f)|^2 = |P_I(f)|^2 + |P_{II}(f)|^2 + |P_{III}(f)|^2$, with the measured noise inside and outside of the fence. Since the turbulent flow in Region III only influences the low frequency contribution the predicted wind noise for this region is truncated for wavelengths that are smaller than two times the height of the wind fence, or $\lambda = 2H$. For the 30% porous fence this prediction is much lower than expected, which results in a poor low frequency

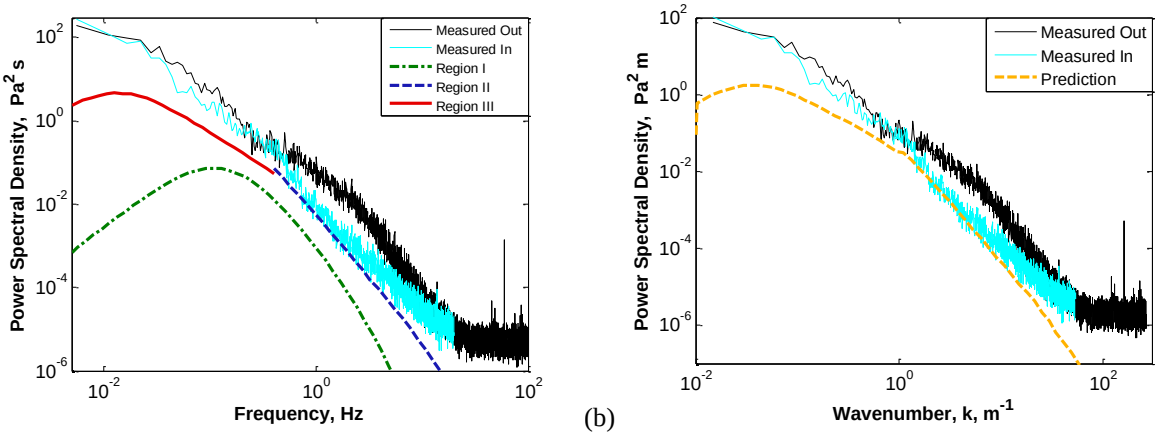

FIG. 76. Measured and predicted wind noise spectra for a wind fence with an open top, open bottom gap, and 30% wall porosity. Data was measured on 3/3/12.

prediction. This is due in part to the velocity spectra fitting method, which gives better matching at lower frequencies but at the cost of a lower magnitude. However, examination of the predictions for the other porous fences shows that this very poor fitting for the 30% fence is the exception, rather than the rule. The wind noise contributions for the flow interaction at the surface of the fence, Region II, is truncated for wavelengths that are larger than two times the height of the wind fence, since the noise source for this region is concentrated on the surface of the wind fence. Figure 76 further indicates that Region II dominates at high frequencies and that the predicted wind noise matches the measured wind noise fairly well. The plots also show that the noise due to the interior flow does not contribute for the 30% wall porosity.

The predicted and measured wind noise spectra for a wind fence with 40% porous walls are shown in Fig. 77; where parts (a) and (b) also show the individual and summed predictions for the three regions, respectively. At low wavenumbers, the noise contribution for Region III dominates, and very closely matches both the inside and outside measured wind noise. At high frequencies the noise contribution for Region II dominates. The prediction for this region is low, but is within an acceptable factor and matches the overall slope of the measured wind noise.

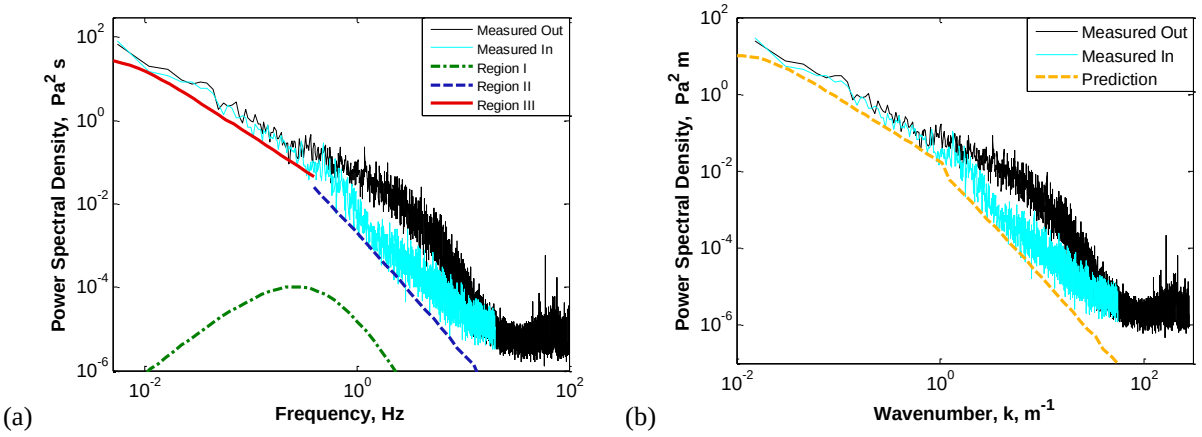

FIG. 77. Measured and predicted wind noise spectra for a wind fence with an open top, open bottom gap, and 40% wall porosity. Data was measured on 3/3/12.

Like the 30% porous fence the noise contributions for the interior flow are extremely low and negligible but even more so for the 40% fence. This is due to the reduced turbulence and velocity gradient inside the 40% fence (see Figs. 19 and 20 on pages 67 and 69). The results confirm that wind noise reductions begin to be optimized with the 40% porous fence.

The individual noise contributions for the 55% porous fence are very similar to the 40% porous fence, as seen in Fig. 78, which shows the individual and summed contributions for the 55% porous fence. Again, the measured noise contributions for the turbulent flow that is outside of the fence matches the measured low frequency wind noise. Likewise, the slope of the predicted noise contribution from the turbulence that interacts with the surface of the fence shows good agreement with the measured high frequency wind noise. However, the magnitude for this region is low, but by an acceptable factor. The flow inside the fence, Region I, is higher than the 40% fence, but it is lower than the 30% porous fence, and is still negligible. This is again due to the lower turbulence and velocity gradient inside the 55% fence as compared to the 30% fence (see Figs. 19 and 20 on pages 68 and 70). However, the rise in noise level for this region indicates that the contribution will continue to increase as the porosity continues to

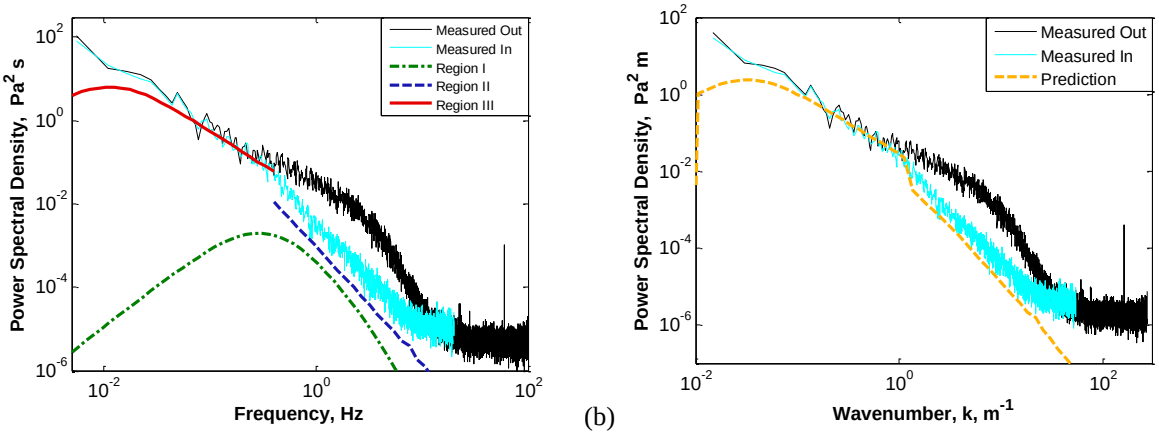

FIG. 78. Measured and predicted wind noise spectra for a wind fence with an open top, open bottom gap, and 55% wall porosity. Data was measured on 3/3/12.

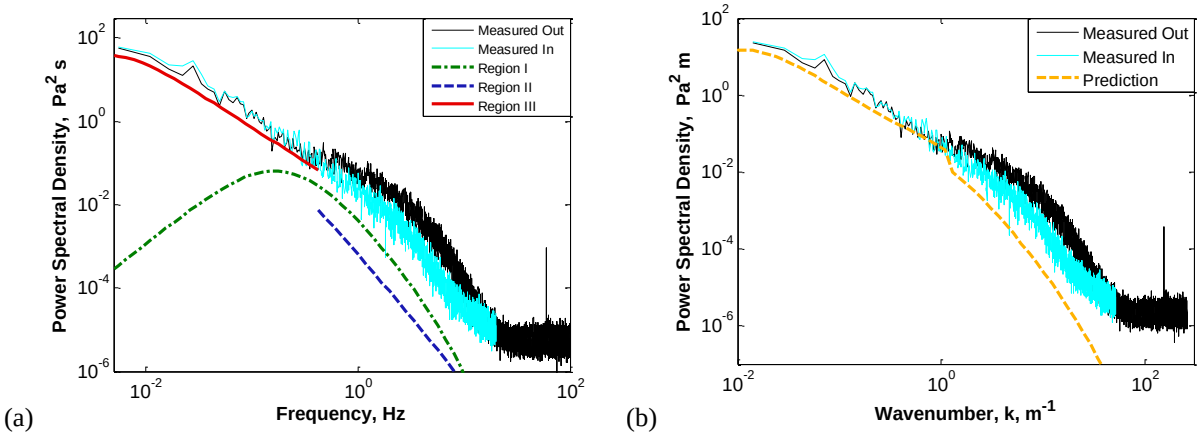

FIG. 79. Measured and predicted wind noise spectra for a wind fence with an open top, open bottom gap, and 65% wall porosity. Data was measured on 3/3/12.

increase. It also indicates that the optimum fence porosity for wind noise reductions is likely between 40% and 55%.

Figure 79 shows the individual and combined noise contributions for the three flow regions, as well as the inside and outside measured wind noise spectra for a wind fence with 65% porous walls. At this point the measured inside spectra begins to resemble the spectra measured outside of the fence in terms of both magnitude and shape. The predicted contribution for Region III still matches the measured noise at low frequencies. The magnitude of the wind noise contribution at the surface of the fence is lower and is dominated by the wind noise due to the flow inside the wind fence. The shape and magnitude of the predicted noise due to the inside flow at this porosity also begins to resemble the magnitude and shape of the measured wind noise, as it becomes the more dominant contribution. However, it is still low at this point.

Figure 80 shows the predicted noise contributions for the three individual flow regions and their combination into a single prediction for the wind noise for an 80% porous wind fence. As can be seen, the wall porosities are open enough that there is little to no difference between

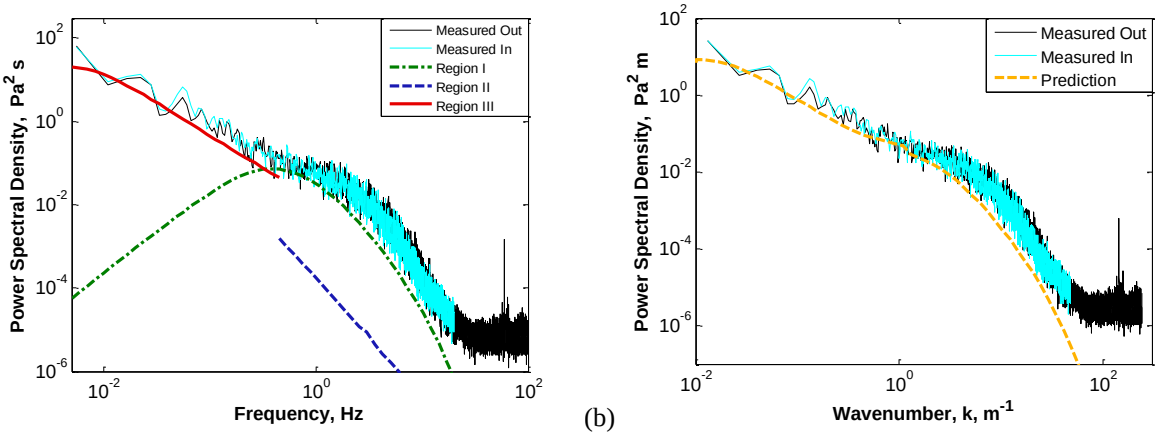

FIG. 80. Measured and predicted wind noise spectra for a wind fence with an open top, open bottom gap, and 80% wall porosity. Data was measured on 3/3/12.

the noise spectra measured outside and inside of the wind fence. Noise contributions from the flow interaction on the surface of the fence, Region II, do not contribute to the measured wind noise. The flow interaction outside the fence is the principal contributor to the measured noise at low wavenumbers, while for wavenumbers larger than k = 1 m^{-1} the flow inside the fence is the dominant noise source. The summed predictions, as shown in Fig. 80b, are on the low side of the measured spectra, but still match its shape and general energy levels.

The comparisons indicate that the dominant noise source for high frequencies or frequencies with wavelengths smaller than twice the height of the wind fence, are due to the turbulence interactions at the surface of the barrier for low to mid level porosities. Conversely, for the high porosities, the contributions of the pressure fluctuations on the barrier's exterior are negligible, while the inside contribution is dominant. The comparisons also show that the dominant noise sources at the center of the wind fence for low wavenumbers, or wavenumbers whose wavelengths are at least twice the size of the wind fence height, are due to the outside

flow, while noise contributions from the flow region inside the fence are negligible. This is consistent for all porosities.

In conclusion, we developed a simple calculation to estimate the wind noise reductions due to a large porous wind barrier. This empirical model shows that the wind noise measured at the center of a wind fence is due to the combination of the different flow interactions inside the wind fence, on its surface, and in the undisturbed region surrounding the wind fence. The individual contributions from Regions I and III can be predicted using the respective measured velocity profiles and turbulence spectra at the center of the fence and upwind of the fence. The wind noise contributions from Region II can be predicted from the measured correlation length around the barrier, the mean velocity distribution at the surface, and the turbulence spectra incident on the barrier's surface. The velocity distribution on the wind fence's surface is determined by the change between the flow velocities outside and inside of the barrier. The magnitude of the prediction for this region is low by a small factor, which suggests that the source region is located further from the surface of the fence than where it was measured, and hence the velocity correlation lengths are larger than what was measured. Finally, the model shows that the flow inside the fence, the correlation length, and the mean flow distribution around the fence are highly dependent on the fence's porosity.

CHAPTER VI

SUMMARY AND CONCLUSIONS

The main goal of this study was to develop a technology that reduces infrasonic wind noise between 0.01-10 Hz, and is simple, cost effective, and improves upon the limitations of pipe arrays and porous hose arrays. Using the principles of wind noise reduction by a compact spherical windscreen and the principles of two dimensional wind breaks for agricultural applications, a large porous wind barrier made of chain link fencing was designed and constructed. A series of measurements and investigations were performed to determine and optimize wind noise reductions by the fence. An empirical formula was derived from these measurements, which estimates the reductions capability of a wind fence, if the size, correlation length, turbulent boundary layer flow, incident turbulence, mean flow velocity distribution around the fence, and the velocity gradient inside the fence are measured.

Measurements and analysis identified the regions of flow that most contribute to the wind noise measured by the microphone at the center of the wind screen. Generally, turbulence interactions at the surface of the wind fence dominate at most wavenumbers. They especially dominate at high wavenumbers where the turbulence wavelengths are smaller than the fence. At low wavenumbers, or where the turbulence wavelengths are larger than the fence, noise due to

the flow outside and away from the fence dominates. The wind noise generated by flow inside the fence is negligible in a well designed wind fence.

Measurements and analysis have determined the physical mechanisms that cause wind noise reductions and how to optimize the reductions. The parameters which effect wind noise reductions are the porosity, a bottom gap, enclosing the top, the overall size of the barrier, and the addition of a secondary wind barrier. The porosity, size, and addition of the secondary wind barrier have the greatest influence in determining the performance of a wind fence enclosure. Investigations into noise contributions due to vortex and wake shedding determined that there was no evidence of vortex shedding, such as spectral peaks and augmentation, in the turbulence spectra measured behind the wind fence. The investigations also showed that noise contributions due to wake turbulence and shedding are negligible.

Porosity is one of the most influential characteristics and mid-level porosities give the best noise reductions. The investigation further determined that porosity affects the correlation length, the change in velocity and amount of turbulence that passes inside the fence, the velocity gradient, and the turbulent boundary layer flow around the fence. At mid-level porosities the velocity gradient is minimized due to a uniform flow field inside the fence, with respect to height. The turbulence inside the wind fence is also minimized and therefore, the turbulence-shear interaction inside the fence is negligible.

A bottom gap is only beneficial to wind noise reduction if there is no secondary wind barrier. The bottom gap influences the magnitude of the turbulence and velocity gradient inside the fence. The open bottom gap allows for an unhindered flow near the ground, which results in

a higher but more uniform flow with respect to height. The more uniform field minimizes the velocity gradient and noise contribution from the turbulence-shear interaction inside the fence.

A porous roof augments noise reductions if there is a secondary barrier. Otherwise reductions are limited and inconsistent. It is speculated that the poor to inconsistent influence on wind noise reductions is due to the relative height of the fence. The addition of a porous roof reduces turbulence reductions inside the fence. Hence, the noise reductions that occur are due in part to the limiting of the turbulence inside the fence.

Measurements and analysis show that increasing the overall fence size increases the noise reductions. The frequency band at which reductions occur is determined by the height. The height does not influence the correlation length, boundary layer flow, and the velocity gradient inside the fence. Therefore, reductions are primarily due to the fence modifying the higher flow streams and the larger turbulence scale lengths associated with these heights. Reductions are also due to an increased area averaging caused by the expanded surface area.

The magnitude of the wind noise reductions for a given frequency band is determined by the wind fence diameter. The diameter affects the correlation length, boundary layer flow, and the velocity gradient inside the fence. An increase in the diameter causes an increase in the turbulence-shear interaction inside the fence, but this contribution is small compared to other contributions. Further, the diameter influences the separation distance between the microphone and the noise due to surface interactions with the incident turbulence. The significant difference between the noise reductions for the expanded diameter fence and the increased height fence indicate that the separation distance is very influential on noise reductions.

A secondary wind barrier greatly improves wind noise reductions. A secondary filter reduces the turbulence and velocity gradient immediately adjacent to the microphone. Noise reductions are caused by further area averaging the reduced turbulence incident to the secondary barrier's surface. Best reductions are achieved when the magnitude and scale of the turbulence has been reduced to values where the secondary barrier is most effective. The initial magnitude and frequency band at which the reductions occur are determined by the primary wind fence, while the enhanced magnitude of these reductions is determined by the secondary wind barrier. These gains do not improve in an additive or multiplicative manner; however the improvements are large enough that the combined system performed better than doubling the wind fence size. Therefore the addition of a secondary wind barrier, such as a dome, provides significant gains in wind noise reductions.

The results for this dissertation were evaluated by comparing the wind noise measured inside the fence to the wind noise measured by a screened and flush mounted microphone set upwind of the fence. This method was employed since it uses the wind noise generated by the well understood turbulence-shear interaction as a reference level. This contribution is independent of sensor shape and will usually be lower than the noise generated by the stagnation pressure. Reduction methods, however, are often evaluated by comparing the measured wind noise to an unscreened surface mounted pressure sensor. As a result, noise reductions appear larger and are often more variable since they use noise due to the stagnation pressure as a reference level. Depending on the frequency the gains should be adjusted by at least 2-12 dB.

The best noise reductions achieved for this study were typically between 20-25 dB and occurred at about 3 Hz. The frequency band width for reductions of 5 dB and greater generally occurred between 0.1 and 20 Hz. This is at the high end of the targeted frequency band of 0.01-

10 Hz. However, reductions of approximately 4-6 dB were achieved for frequencies with turbulence wavelengths larger than the fence. A very large pipe array still achieves better reductions at low frequencies. However, the wind fence enclosure is more compact, cost effective, and detected microbaroms at high wind speeds (mean velocity of 5.3 m/s or about 19.1 km/h) that normally mask out microbaroms and other infrasonic acoustics sources. This demonstrates that wind fence enclosures are a viable noise reduction technology.

In summary, the mechanisms and parameters to optimize wind noise reduction are better understood, and an optimized wind fence can be designed accordingly. The measured data, theory, and empirical model suggest that the optimized wind fence should have a mid-level porosity and be as large as possible. The relationship between the dimensions is determined by the reduction goals. To obtain better reduction gains at low frequencies the design should be very tall. To maximize the reduction levels in a given frequency bandwidth the design should be wide, but should not exceed half the distance to the turbulence reattachment point. Additionally, maximum reductions are achieved with a secondary barrier, a closed bottom gap, and a porous top.

BIBLIOGRAPHY

1. M. S. Morgan, *An Investigation of the Sources and Attenuation of Wind Noise in Measurement Microphones,* Ph.D. Dissertation, Department of Physics and Astronomy, The University of Mississippi. (1992)
2. M. Morgan and R. Raspet, "Investigation of the mechanisms of low-frequency wind noise generation outdoors," *J. Acoust. Soc. Am.*, **92** (2), 1180-1183. (1992)
3. B. R. Munsun, D. F. Young, and T. H. Okiishi, *Fundamentals of Fluid Mechanics*. New York, Chichester, Brisbane, Toronto, Singapore: John Wiley and Sons, (2006).
4. P. D. Schomer, R. Raspet, J. Brunner, D. Marshall, M. Wagner, and D. Walker, "Reduction of wind noise for unattended blast noise monitoring," *Noise Control Engineering Journal*, **34** (2), 77-88. (1990)
5. National Committee for Fluid Mechanics Films. *Illustrated Experiments in Fluid Mechanics: The NCFMF Book of Film Notes*, 2nd ed, MIT, Cambridge, MA. (1972)
6. K. Chung, N McKibben, and Luc Mongeau, "Wind noise in hearing aids with directional and omnidirectional microphones: Polar characteristics of custum-made hearing aids," *J. Acoust. Soc. Am.*, **127** (4), 2529-2542. (2010)
7. M. Hedlin and R. Raspet, "Infrasonic wind-noise reduction by barriers and spatial filters," *Journal of the Acoustical Society of America*, **114** (3), 1379-1386. (2003)
8. B. Alcoverro, "Acoustic filters design and experimental results," in Proceedings: Workshop on Infrasound, Commissariat à l'Energie Atomique, Bruyères-le-Châtel, Fance, 21-24 July 1998.
9. M. Hedlin, B. Alcoverro, and G. D'Spain. "Evaluation of rosette infrasonic noise-reducing spatial filters," *J. Acoust. Soc. Am.*, **114** (4), 1807-1820. (2003)

10. F. B. Daniels, “On the propagation of sound waves in a cylindrical conduit,” *J. Soc. Acoust. Am.*, **31** (4), 529-531, (1959).

11. R. Burridge, “The acoustics of pipe arrays,” *Geophys. J. R. Astr. Soc.*, **26**, 53-69, (1971).

12. Z. C. Zheng and B. K. Tan, “Reynolds number effects on flow/acoustic mechanisms in spherical windscreens,” *J. Acoust. Soc. Am.*, **113** (1), 161-166. (2003)

13. R. Raspet, J. Yu, and J. Webster, “Low frequency wind noise contributions in measurement microphones,” *J. Acoust. Soc. Am.*, **123** (3), 1260-1269. (2008)

14. J. Yu, *Infrasound Wind Noise Predictions*, M.S. Thesis, Department of Physics and Astronomy, The University of Mississippi. (2007)

15. R. Raspet, J. Webster, and J. Yu, “Low-frequency wind noise reduction by spherical windscreens,” *153rd Meeting Acoustical Society of America*, Salt Lake City, UT, 4-8 June 2007.

16. G. C. Lauchle, “Turbulent Boundary Layer (TBL) Wall Pressure Fluctuations and Acoustics,” *Lecture, ACS 530*, The Pennsylvania State University.

17. J. R. Abbott, R. Raspet, and J. Webster, “Porosity effects in large wind screening structures,” *161st Meeting Acoustical Society of America*, Seattle, WA, 24 May 2011

18. J. R. Abbott, *The Time Dependent Relationship of Vertical Wind Velocity and Pressure Fluctuations Over Flat Open Ground*, M.S. Thesis, Department of Physics and Astronomy, The University of Mississippi. (2010)

19. J. Bleazy, “Experimental determination of effectiveness of microphone wind screens,” *J. Audio Eng. Soc.*, **9**, 48-53. (1961)

20. R. Hosier and P. Donavan, “Microphone Windscreen Performance,” *National Bureau of Standards Report*, NBSIR 79-1599, January 1979.

21. D. Blomquist, "An Experimental Investigation of Foam Windscreens," *Proc, InterNoise*, **73**, 589-593. (1973)

22. I. Dyer, "Self Noise of Cylindrical Wind-screens," *Bolt Beranek and Newman Report 225,* Job 637, August 1954.

23. F. J. van Leeuwen, "Windscreens and 'Anti-Plop' screens for microphones," (in Dutch), *Omroep-Techische Mededelingen*, **2** (4), 168-172. (Nov. 1960)

24. G. Maidanik and W. Reader, "Filtering action of a blanket dome," *J. Acoust. Soc. Am,* **44**, 497-502. (1968)

25. K. Dillion, *An Investigation of Wind Noise Over a Flat Plate*, M.S. Thesis, Department of Physics and Astronomy, The University of Mississippi. (2005)

26. J. Webster, R. Raspet, and J. Yu, "The pressure distribution around foam spheres outdoors," *Joint 150th Meeting Acoustical Society of America and Noise-Con,* Minneapolis, MN, 17-21 October 2005

27. R. Raspet, J. Webster, and K. Dillion, "Framework for wind noise studies," *J. Acoust. Soc. Am.*, **119** (2), 834-843. (2006)

28. W. Phelps, "Microphone Wind Screening," *RCA Review*, **3**, 203-212. (1938)

29. M. Strasberg, "Nonacoustic noise interference in measurements of infrasonic ambient noise," *J. Acoust. Soc. Am.*, **66** (5), 1487-1493. (1979)

30. M. Strasberg, "Dimensional Analysis of Windscreen Noise," *J. Acoust. Soc. Am.*, **83** (2), 544-548. (1988)

31. H. A. Panofsky and J. A. Dutton, *Atmospheric Turbulence, Models and Methods for Engineering Applications*. New York, Chinchester, Brisbane, Toronto, Singapore: John Wiley and Sons. (1984)

32. J. A. Elliot, “Instrumentation for measuring static pressure fluctuations within the atmospheric boundary layer,” *Boundary Layer Meteorology*, **2**, 476-495. (1972)

33. J. A. Elliot, “Microscale pressure fluctuations measured within the lower atmospheric boundary layer,” *J. Fluid Mech.*, **53** (2), 351-383. (1972)

34. H. V. Fuchs, “Measurement of pressure fluctuations within subsonic turbulent jets,” *J. Sound Vib.*, **22** (3), 361-378. (1972)

35. W. K. George, P. D. Beuther, and R. E. A. Arndt, “Pressure spectra in turbulent free shear flows,” *J. Fluid Mechanics*, **148**, 155. (1984)

36. J. Yu, *Calculation of Wind Noise Measured at the Surface Under Turbulent Wind Fields*, Ph.D. Dissertation, Department of Physics and Astronomy, The University of Mississippi. (2009)

37. J. Yu, R. Raspet, J. Webster, and J. Abbott, “Wind noise measured at the ground surface,” *J. Acoust. Soc. Am.*, **129**, 2445. (2011)

38. R. H. Kraichnan, “Pressure fluctuations in turbulent flow over a flat plate,” *J. Acoust. Soc. Am.* **28**, 378. (1956).

39. R. H. Kraichnan, “Pressure field within homogenous anisotropic turbulence,” *J. Acoust. Soc. Am.* **28**, 64. (1956).

40. J. Yu, R. Raspet, J. Webster, and J. Abbott, “Improved prediction of the turbulence-shear contribution to wind noise pressure spectra,” *J. Acoust. Soc. Am.*, **130**, 3590. (2011)

41. M. D. A. E. S. Perera, “Shelter behind two-dimensional solid and porous fences,” *J. Wind Engineering and Industrial Aerodynamics*, **8**, 93-104. (1981)

42. E. F. Bradley and P. J. Mulhearn, “Development of velocity and shear stress distributions in the wake of a porous shelter fence,” *J. Wind Engineering and Industrial Aerodynamics*, **15**, 145-156. (1983)

43. R. M. Cionco, “A mathematical model for air flow in a vegetative canopy,” *J. Applied Meteorology*, **4**, 517-522. (1965)

44. L. H. Allen, “Turbulence and wind speed spectra within a Japanese larch plantation,” *J. Applied Meteorology*, **7**, 73-38. (1968)

45. B. Amiro, “Statistics of atmosphere turbulence within a natural black spruce forest canopy,” *Boundary-Layer Meteorology*, **44**, 267-283. (1988)

46. B. Amiro, “Comparison of turbulence statistics within three boreal forest canopies,” *Boundary-Layer Meteorology*, **51**, 99-121. (1990)

47. M. R. Raupach and A. S. Thom, “Turbulence in and above plant canopies,” *Ann. Rev. Fluid Mech.*, **13**, 97-129. (1981)

48. D. D. Baldocchi and T. P. Meyers, “Turbulence structure in a deciduous forest,” *Boundary-Layer Meteorology*, **43**, 345-364. (1988)

49. T. P. Meyers and D. D. Baldocchi, “The budgets of turbulent kinetic energy and Reynolds stress within and above a deciduous forest,” *Agricultural and Forest Meteorology*, **53**, 207-222. (1991)

50. D. ReVelle, “Infrasonic noise reduction using shelters/windbreaks”, *Infrasonic Technology Workshop*, Bermuda, U.K. 3-7 November 2008

51. A. J. Bedard, B. W. Bartman, A. N. Keane, D. C. Welsh, and R. T. Nishiyama, “A device for reducing wind and breaking flow into small-scale eddies to decrease infrasonic noise (A),” *J. Acoust. Soc. A.*, **122** (5), 2559. (2007)

52. A. J. Bedard, B. W. Bartman, A. N. Keane, D. C. Welsh, and R. T. Nishiyama. "The infrasound Network (ISNET): Background, design details, and display capability as an 88D adjunct tornado detection tool," *Proceedings of the 22nd Conf. On Severe Local Storms*, Hyannis, MA, *Amer. Meteor. Soc*. Paper 1.1

53. D. Christie "Wind noise reduction at IMS infrasound stations," *Infrasonic Technology Workshop*, Bermuda, U.K. in 3-7 November 2008.

54. E. J. Plate, "The aerodynamics of shelter belts," *Agricultural Meteorology*, **8**, 203-222. (1971)

55. J. K. Raine and D. C. Stevenson, "Wind protection by model fences in a simulated atmospheric boundary layer," *J. of Wind Engineering and Industrial Aerodynamics,* **2 (2)**, 159-180. (1977)

56. Z. Dong, W. Luo, G. Qian, and H. Wang, "A wind tunnel simulation of the mean velocity fields behind upright porous fences," *Agricultural and Forest Meteorology*, **146**, 82-93. (2007)

57. J. C. Argete and J. D. Wilson, "The microclimate in the centre of small square sheltered plots," *Agriculture and Forest Meteorology*, **48**, 185-199. (1989)

58. L. Liszka, Swedish Patent No. 7315138-3, 30 October, 1975

59. D. Clauter, "Infrasonic Research Program at AFTAC," *34th Meeting Monitoring Research and Review: Ground-Based Nuclear Explosion Monitoring Techniques,* Albuquerque, NM, 20 September 2012.

60. Q. A. Shams, A. J. Zuckerwar, and B. R. Sealy, "Compact nonporous windscreen for infrasonic measurements," *J. Acoust. Soc. Am.*, **118** (3), 1335-1340. (2005)

61. A. J. Zukerwar, Q. A. Shams, K. K. Ahuja, and R. Funk, "Soaker hose versus compact nonporous windscreen: A comparison of performance at infrasonic frequencies," *Joint 150th Meeting Acoustical Society of America and Noise-Con*, Minneapolis, MN, 20 Oct. 2005

62. J. Webster, R. Raspet, J. Yu, and W. Prather, "Measurement of wind noise levels in streamlined probes," *J. Acoust. Soc. Am.*, **127** (5). (2010)

63. F. D. Shields, "Low-frequency wind noise correlation in microphone arrays," *J. Acoust. Soc. Am.*, **117**, 3489-3496. (2005)

64. R. T. Nishiyama and A. J. Bedard, "A Quad-disc static pressure probe for measurement in adverse atmospheres: With a comparative review of static pressure probe designs," *Rev. Sci. Instrum.*, **62** (9), 2193-2204. (1991)

65. A. Nakamura, R. Matsumoto, A. Sugiyama, and T. Tanaka, "Some investigations on output level of microphones in air streams," *J. Acoust. Soc. Am.*, **46**, 1391-1396. (1969)

66. A. Nakamura, A. Sugiyama, T. Tanakara, and R. Matsumoto, "Experimental investigation for detecting of sound-pressure level by a microphone in an airstream," *J. Acoust. Soc. Am.*, **50** (1), 40-46. (1971)

67. D. K. Wilson and M. J. White, "Simulation of fluid flow in and around a porous windscreen," *151st Meeting of Acoustical Society of America*, Providence, RI, 5-9 June 2006.

68. Y. Xu, Z. C. Zheng, and D. K. Wilson, "A computational study of the effect of windscreen shape and flow resistivity on turbulent wind noise reduction," *J. Acoust. Soc. Am.*, **129** (4), 1740-1747. (2011)

69. H. Ballard and M. Izquierdo, "Reduction of Microphone wind noise by the generation of a proper turbulent flow," *U.S. Army Electronics and Development AR 262*, DDC. No. AD455966, February 1965.

70. R. A. Kumar, C. Sohn, and B. H. L Gowda, "Passive control of vortex-induced vibrations: an overview," *Recent Patents on Mechanical Engineering 2008*, **1** (1), 1-11. (2008)

71. C. W. Park and S. J. Lee, "The effects of a bottom gap and non-uniform porosity in a wind fence on the surface pressure of a triangular prism located behind the fence," *Journal of Wind Engineering and Industrial Aerodynamics*, **89**, 1137-1154. (2001)

72. H. B. Kim and S. J. Lee, "The structure of turbulent shear flow around a two-dimensional porous fence having a bottom gap," *Journal of Fluids and Structures*, **16** (3), 317-329. (2002)

73. D. Kleinert and C. Talmage, "Design and development of a high impedance amplifier for use with piezoelectric infrasound microphones," *American Geophysical Union Fall Meeting 2011*, San Francisco, CA, 5-9 December 2011.

74. D. Christie and P. Campus, "The IMS infrasound network: design and establishment of infrasound stations," *Infrasound Monitoring for Atmospheric Studies*, A. Le Pichon, E. Blanc, and A. Hauchecorne (Eds.), Springer Science + Business Media B.V., 27-72. (2010)

75. P. Campus and D. Christie, "Worldwide observations of infrasonic waves," *Infrasound Monitoring for Atmospheric Studies*, A. Le Pichon, E. Blanc, and A. Hauchecorne (Eds.), Springer Science + Business Media B.V., 181-230. (2010)

76. D. Christie, B. L. N. Kennett, and C. Tarlowski, "Advances in infrasound technology with application to nuclear explosion monitoring," *Proceeding of the 29th Monitoring Research Review*, Los Alamos National Laboratory, Los Alamos, New Mexico, 825-835. (2007)

77. J. Webster and R. Raspet, "Wind noise minimization for single infrasonic sensors," *161st Meeting Acoustical Society of America*, Seattle, WA, 23-27 May 2011

78. M. C. Willis, M. Garces, C. Hetzer, and S. Businger, "Source modeling of microbaroms in the Pacific," *The 84th AMS Annual Meeting*, Seattle, WA, 10-16 January 2004.

79. "R. Waxler and K. Gilbert, "The radiation of atmospheric microbaroms by ocean waves," *J. Acoust. Soc. Am.*, **119** (5), 2651. (2006)

80. M. A. Garcés, C. H. Hetzer, M. Willis, and S. Businger, "Integration of infrasonic models with ocean wave spectra and atmospheric specifications to produce global estimates of microbarom signal levels," *Proceedings of the 25th Seismic Research Review*, 617-627. (2003)

81. J. T. Priestly, *Correlation Studies of Pressure Fluctuations on the Ground Beneath a Turbulent Boundary Layer*, M.S. Thesis, Institute for Fluid Dynamics in Applied Mathematics, University of Maryland, (1965); and *National Bureau of Standards Report*, No. 8942. (1965)

82. J. T. Priestly, "Calculation of the effectiveness of infrasound line microphones for reducing wind noise," *National Bureau of Standards Report*, No. 9380. (1966)

LIST OF APPENDICIES

APPENDIX A: DERIVATION OF THE STAGNATION PRESSURE

The stagnation pressure is derived by from the Navier-Stokes equation by applying the divergence to the Navier-Stokes equation and then enforcing the incompressibility condition to form the Poisson equation. Next the the Reynolds decomposition is applied to Poisson's equation.

The Navier-Stokes equation is:

$$\frac{\partial \vec{u}}{\partial t} + (\vec{u} \cdot \nabla)\vec{u} = -\frac{\nabla P}{\rho} + \nu \nabla^2 \vec{u}\,, \tag{43}$$

where ρ is the fluid density, ν is the fluid kinematic viscosity, P the pressure, and $\vec{u}$ is the fluid velocity.

The equation of continuity is given by:

$$\frac{\partial u_i}{\partial x_i} = \nabla \cdot \vec{u} = 0\,. \tag{44}$$

Taking the divergence of the Navier-Stokes equation gives:

$$\nabla \cdot \frac{\partial \vec{u}}{\partial t} + \nabla \cdot \left[(\vec{u} \cdot \nabla)\vec{u}\right] = -\frac{\nabla^2 P}{\rho} + \nu \nabla \cdot \left(\nabla^2 \vec{u}\right). \tag{45}$$

Equation (45) can be expanded and rewritten using the definition

$\nabla \times (\nabla \times a) = \nabla(\nabla \cdot a) - \nabla^2 a$, as

$$\frac{\partial(\nabla \cdot \vec{u})}{\partial t} + \nabla \cdot \left[(\vec{u} \cdot \nabla)\vec{u}\right] = -\frac{\nabla^2 P}{\rho} + \nu \nabla \cdot \left[\nabla(\nabla \cdot \vec{u}) - \nabla \times (\nabla \times \vec{u})\right]. \tag{46}$$

Applying the continuity condition, Eq. (46), and recalling that the divergence of a curl is zero,

Eq. (46) becomes

$$\nabla \cdot \left[(\vec{u} \cdot \nabla) \vec{u} \right] = -\frac{\nabla^2 P}{\rho}, \tag{47}$$

which is Poisson's equation

$$\nabla^2 P = -\rho \frac{\partial^2 u_i u_j}{\partial x_j \partial x_i}. \tag{48}$$

The derivation is further carried out by considering the identity:

$$\nabla\left(\vec{a} \cdot \vec{b}\right) = \vec{a} \times \left(\nabla \times \vec{b}\right) + \vec{b} \times \left(\nabla \times \vec{a}\right) + \left(\vec{b} \cdot \nabla\right)\vec{a} + \left(\vec{a} \cdot \nabla\right)\vec{b}. \tag{49}$$

Then,

$$\frac{1}{2}\nabla u^2 = \frac{1}{2}\nabla\left(\vec{u} \cdot \vec{u}\right) = \frac{1}{2}\left[\vec{u} \times \left(\nabla \times \vec{u}\right) + \vec{u} \times \left(\nabla \times \vec{u}\right) + \left(\vec{u} \cdot \nabla\right)\vec{u} + \left(\vec{u} \cdot \nabla\right)\vec{u}\right], \tag{50}$$

which simplifies to the following:

$$\frac{1}{2}\nabla u^2 = \vec{u} \times \left(\nabla \times \vec{u}\right) + \left(\vec{u} \cdot \nabla\right)\vec{u}. \tag{51}$$

Rearranging Eq. (51), gives:

$$\left(\vec{u} \cdot \nabla\right)\vec{u} = \frac{1}{2}\nabla u^2 - \vec{u} \times \left(\nabla \times \vec{u}\right). \tag{52}$$

Substituting Eq. (52) into Eq. (47), and assuming that the flow's vorticity is negligible, or $\nabla \times \vec{u} \cong 0$, and that $\nabla^2 a = \nabla \cdot \left(\nabla a\right)$, then Poisson's equation becomes,

$$\nabla \cdot \left(\nabla \frac{u^2}{2} \right) = \nabla \cdot \left(-\frac{\nabla P}{\rho} \right), \tag{53}$$

which leads to the relation

$$\nabla \frac{u^2}{2} = -\frac{\nabla P}{\rho}. \tag{54}$$

Integrating both sides of Eq. (54) gives the Bernoulli equation for a flow with negligible vorticity,

$$P = -\rho \frac{u^2}{2} + C, \tag{55}$$

which contains the stagnation pressure.

APPENDIX B: DERIVATION OF THE TURBULENCE-TURBULENCE AND TURBULENCE-SHEAR INTERACTIONS

The turbulence-turbulence and turbulence-shear interactions are derived from the Navier-Stokes equation and Poisson's equation, Eq. (56).

$$\nabla^2 P = -\rho \frac{\partial^2 u_i u_j}{\partial x_j \partial x_i} \tag{56}$$

This derivation of Eq. (43) is in Appendix A and will not be repeated here. First, the Reynolds decomposition is applied,

$$P = \overline{P} + p\,, \tag{57}$$

$$u_i = \overline{U}_i + u_i'\,, \tag{58}$$

where the $\overline{P}$ and $\overline{U}_i$ are the mean terms for the static pressure and velocity, and p and u' are the fluctuating terms for the static pressure and velocity. Eq. (56) becomes

$$\nabla^2 \overline{P} + \nabla^2 p = -\rho \frac{\partial^2}{\partial x_i \partial x_j}\left(\overline{U}_i \overline{U}_j + \overline{U}_i u_j' + u_i' \overline{U}_j + u_i' u_j'\right). \tag{59}$$

Since $\overline{u_i'} = \overline{p} = 0$ the fluctuation terms can be eliminated by taking the time average of Eq. (59),

$$\nabla^2 \overline{P} = -\rho \frac{\partial^2}{\partial x_i \partial x_j}\left(\overline{U}_i \overline{U}_j + \overline{u_i' u_j'}\right). \tag{60}$$

Subtracting Eq. (60) from Eq. (57) we get:

$$\nabla^2 p = -\rho \frac{\partial^2}{\partial x_i \partial x_j}\left[\overline{U}_i u_j' + u_i' \overline{U}_j + \left(u_i' u_j' - \overline{u_i u_j}\right)\right]. \tag{61}$$

Applying the equation of continuity, $\frac{\partial \overline{U}_i}{\partial x_i} = \frac{\partial u_i'}{\partial x_i} = 0$ and therefore $\frac{\partial^2 \overline{U}_i}{\partial x_i \partial x_j} = \frac{\partial^2 u_i'}{\partial x_i \partial x_j} = 0$, Eq. (61) becomes

$$\nabla^2 p = -\rho\left[\frac{\partial u_j'}{\partial x_i}\frac{\partial \overline{U}_i}{\partial x_j} + \frac{\partial \overline{U}_j}{\partial x_i}\frac{\partial u_i}{\partial x_j} + \frac{\partial^2}{\partial x_i \partial x_j}\left(u_i u_j - \overline{u_i u_j}\right)\right]. \tag{62}$$

This is a Poisson equation for the fluctuating pressure. Since $\frac{\partial u_j'}{\partial x_i}\frac{\partial \overline{U}_i}{\partial x_j} = \frac{\partial \overline{U}_j}{\partial x_i}\frac{\partial u_i}{\partial x_j}$, Eq. (62) can be rewritten as

$$\nabla^2 p = -\rho\left[2\frac{\partial \overline{U}_j}{\partial x_i}\frac{\partial u_i}{\partial x_j} + \frac{\partial^2}{\partial x_i \partial x_j}\left(u_i u_j - \overline{u_i u_j}\right)\right], \tag{63}$$

where the first term is the turbulence shear term and the second term is the turbulence-turbulence term; the primes have been dropped from the fluctuating terms. The turbulent fluctuating pressure is independent of the viscosity of the fluid. The turbulence-mean shear interaction is the first term calculated under the assumption that the turbulence is isotropic and that the derivative of the mean velocity is a constant.

APPENDIX C: FREQUENCY BANDWIDTH LIMITS FOR SPATIAL FILTERS

The frequency bandwidth for spatial filters is limited. Consider the upper and lower limits for coherent pulse detection under windy conditions. The upper limit is determined by the coherence of the acoustic signal. For an acoustic signal to be coherent in a spatial filter, the filter's diameter, D, must be less than or equal to the acoustic wavelength, λ, or $D \leq \lambda$. The acoustic wavelength, λ, is determined by dividing the acoustic speed of sound, c, by the frequency, *f*, or $\lambda = c/f$; therefore the relation $D \leq \lambda$ can be written as $D \leq c/f$. Solving for frequency we see that he upper limit is $f_{upper} \leq c/2D$.

For the turbulence to be incoherent, the turbulence correlation length, L, must be much smaller than the filter's diameter, or $L < D$, and smaller than or equal to the convective wavelength, λ_c, or $L \leq \lambda_c$. Therefore, the lower limit is determined by the incoherence of the turbulence. λ_c is defined asthe convection velocity, U_c, divided by the frequency, *f*, or $\lambda_c = U_c/f$. $L \leq \lambda_c$ can be written as $L \leq U_c/f$, and therefore $U_c/f < D$. Solving for frequency we see that $f_{lower} > U_c/D$. The maximum usable bandwidth is therefore, $U_c/D < f < c/D$. As an example, for a 70 m diameter spatial filter in a 5 m/s wind, the wind noise reduction frequency bandwidth is approximately 0.07 Hz $< f <$ 4.9 Hz, and the ratio between the two is $f_{upper}/f_{lower} \approx 70$. If the wind speed increases to 10 m/s, then the frequency bandwidth changes to 0.1 Hz $< f <$ 4.9 Hz, and the ratio decreases to $f_{upper}/f_{lower} \approx 35$.

APPENDIX D: DERIVATION OF PRESSURE FLUCTUATION SPECTRA

Starting with the general form of the Poisson equation,

$$\nabla^2 p = -\rho \frac{\partial^2 u_i u_j}{\partial x_j \partial x_i}, \tag{64}$$

where p is the pressure, ρ is the density of air, and u_i and u_j are components of the velocity. Applying the incompressibility condition and Reynolds decomposition u = (U+ũ) to the Navier-Stokes equation, the source equation for pressure fluctuations due to the turbulence-shear interaction for a turbulent flow is:

$$\nabla^2 p(\vec{x},t) = -2\rho s(z) \frac{\partial \tilde{w}(\vec{x},t)}{\partial x}, \tag{65}$$

where s(z) is the horizontal velocity gradient, or $s(z) = \partial u / \partial z$, and $\tilde{w}(\vec{x},t)$ is the z or vertical component of the turbulence.

The general form of the pressure fluctuation spectra over a flat plate can be derived by taking the space-time Fourier transform of Eq. (65). The plate is formed by letting z equal a constant, with x and y forming a plane in z, and assume that the flow is stationary and homogeneous at the plate. Assuming that the time dependent pressure can be solved by using a Green's function at a plane surface, then:

$$p(\vec{x},t)\big|_{z=0} = \frac{1}{2\pi} \int_{z'>0} \frac{q(\vec{x}',t)}{|\vec{x}-\vec{x}'|} d^3\vec{x}' \tag{66}$$

where $q(\vec{x},t)$ is the source term, or $q(\vec{x},t) = -2\rho s(z)\dfrac{\partial \tilde{w}(\vec{x},t)}{\partial x}$. The space-time Fourier transforms for the pressure and source term are defined as:

$$P(k_x, k_y, z, \omega) = \int_{-\infty}^{\infty}\int_{-\infty}^{\infty}\int_{-\infty}^{\infty} p(x,y,t)e^{-i(k_x x + k_y y + \omega t)}dxdydz \tag{67}$$

$$Q(k_x, k_y, z, \omega) = \int_{-\infty}^{\infty}\int_{-\infty}^{\infty}\int_{-\infty}^{\infty} q(x,y,t)e^{-i(k_x x + k_y y + \omega t)}dxdydt \tag{68}$$

Applying the space-time Fourier transform to $\nabla^2 p(\vec{x},t) = -q(\vec{x},t)$ gives:

$$\nabla^2 P = -Q \tag{69}$$

The P and Q function as wave like structures in planes parallel to the flat plate. We can therefore let $P = P_0 e^{-i(k_x x + k_y y)}$, $\partial^2 P/\partial x = -k_x^2 P$, and $\partial^2 P/\partial y = -k_y^2 P$. Defining $\kappa^2 = k_x^2 + k_y^2$ Eq. (69) becomes:

$$\nabla^2 P = -\kappa^2 P + \frac{\partial^2 P}{\partial z^2} = -Q \tag{70}$$

This is a non-homogeneous, linear ordinary differential equation, with the general solution:

$$P(\vec{k}, z, \omega) = A_1 e^{\kappa z} + B_1 e^{-\kappa z} + \frac{1}{\kappa}\int_{z'>0} e^{-\kappa|z'-z|} Q(z', \vec{\kappa}, \omega)dz' \tag{71}$$

Applying the boundary conditions that P must be finite as $z \to \infty$ and the normal derivative of P at the surface of the plate is zero, or $\left.\dfrac{\partial P}{\partial z}\right|_{z=0} = 0$, then $A_1 = B_1 = 0$, and Eq. (71) becomes:

$$P\left(\vec{k},z,\omega\right)=\frac{1}{\kappa}\int_{z'>0}e^{-\kappa|z'-z|}Q\left(z',\vec{\kappa},\omega\right)dz' \tag{72}$$

When z = 0, the pressure spectrum at the surface of the plate becomes:

$$P\left(\vec{k},0,\omega\right)=\frac{1}{\kappa}\int_{z'>0}e^{-\kappa|z'|}Q\left(z',\vec{\kappa},\omega\right)dz' \tag{73}$$

With the final form as function of wavenumber,

$$P\left(\vec{k},\omega\right)=\frac{1}{\kappa}\int_{z>0}e^{-\kappa z}Q\left(z',\vec{\kappa},\omega\right)dz \tag{74}$$

where the pressure spectra is both inversely proportional to and decreases exponentially with wavenumber, k, and κ is the magnitude of the horizontal wavenumber; or $\kappa=\left|\vec{\kappa}\right|=\sqrt{k_x^2+k_y^2}$.

In full form Eq. (74) is:

$$P\left(\vec{k},\omega\right)=\frac{1}{\kappa}\int_{z>0}e^{-\kappa z}\left[-\int_{-\infty}^{\infty}\int_{-\infty}^{\infty}\int_{-\infty}^{\infty}2\rho s(z)\frac{\partial\tilde{w}\left(\vec{x},t\right)}{\partial x}e^{-i\left(k_x x+k_y y+\omega t\right)}dxdydt\right]dz \tag{75}$$

VITA

JohnPaul Russell Abbott was born January 30, 1981 in Lethbridge, Alberta, Canada to Craig and Ellen Abbott. When his father began his doctoral studies in Psychology at the University of Utah, JohnPaul moved to Salt Lake City, Utah, where he graduated from Highland High School and received the Boy Scouts of America Eagle Scout Award in 1999. After graduating from high school, JohnPaul attended Brigham Young University in Provo, Utah. After a year he left to serve a two year church mission in Florianópolis, Brazil. Upon returning, JohnPaul resumed his studies and graduated with a Bachelor of Science in Physics with a minor in Portuguese in August 2007. During his time as an undergraduate, JohnPaul was actively involved with the university's Acoustics Research Group. He also did a summer internship in Berlin, Germany for the consulting firm Acoustic Design Ahnert. JohnPaul began his graduate studies in Physics at the University of Mississippi in the fall of 2007. In May 2010 he graduated with his Master of Science degree in Physics and began working on his Ph.D. That same year JohnPaul graduated from the Physical Acoustics Summer School held in La Cienega, New Mexico. He was awarded with the University of Mississippi Zdravko Stipcevic Honors Fellowship from 2007-2013. After graduation, JohnPaul will pursue a career in research and teaching.

Outside of academics, JohnPaul enjoys archery, church, history, hiking, camping, fishing, leisure reading, dancing, rugby, and music. He has been an active member of the Memphis Symphony Chorus since January 2010.